Summer 2019

Coherent effects in wave propagation through complex media

Milan Koirala

Department: Physics

COHERENT EFFECTS IN WAVE PROPAGATION THROUGH COMPLEX MEDIA

by

MILAN KOIRALA

A DISSERTATION

Presented to the Graduate Faculty of the

MISSOURI UNIVERSITY OF SCIENCE AND TECHNOLOGY

In Partial Fulfillment of the Requirements for the Degree

DOCTOR OF PHILOSOPHY

in

PHYSICS

2019

Approved by:

Alexey Yamilov, Advisor
S. Thomas Vojta
Paul E. Parris
Daniel Fischer
Xiaodong Yang

PUBLICATION DISSERTATION OPTION

This dissertation consists of the following five articles which have been submitted for publication, or will be submitted for publication as follows:

Paper I: Pages 20–32 have been published as *Detection of a diffusive cloak via second-order statistics*, in Optics Letters Vol. 41, Issue **16**, pp. 3860-3863 (2016) with Alexey Yamilov.

Paper II: Pages 33–43 have been published as *Uncloaking diffusive-light invisibility cloaks by speckle analysis* in Optics Letters Vol. 42, Issue **10**, pp. 1998-2001 (2017) with Andreas Niemeyer, Frederik Mayer, Andreas Naber, Alexey Yamilov, and Martin Wegener.

Paper III: Pages 44–61 have been published as *Inverse Design of Perfectly Transmitting Eigenchannels in Scattering Media* in Physical Review B **96**, 054209 (2017) with Raktim Sarma, Hui Cao, and Alexey Yamilov.

Paper IV: Pages 62–83 is submitted as *Inverse design of long-range intensity correlations in scattering media*, in Physical Review B, with Raktim Sarma, Hui Cao, and Alexey Yamilov.

Paper V: Pages 84–101 have been published as *Critical states embedded in the continuum* in new Journal of Physics **17**, 013003 (2015) with Alexey Yamilov, Ali Basiri, Yaroon Bromberg, Hui Cao and Tsampikos Kottos.

ABSTRACT

Diffusion is a powerful and versatile description of a typical wave propagation in a random scattering medium that disregards phase and, thus, a possibility of interference. Speckle, transmission fluctuations, wave localization, non-local correlations, and transmission eigenchannels are examples of persistent interference effects, which arise in the course of deterministic propagation. Such wave phenomena contain a wealth of information about the medium and the source of waves, enabling sensing and coherent control of the propagation. The nonlocal correlations and speckle statistics of the partially coherent light are used to uncover an object hidden by a diffusive cloak inside a strong scattering medium. It is shown that it is possible to detect the size and position, including the depth, of the object unknown apriori. In addition, a theoretical model is developed to predict the geometry dependence of the transmission eigenchannels and intensity correlations. It is demonstrated that deformation of the geometry of the system offers a predictable approach to coherent control of wave propagation in random media that is complementary to wavefront shaping. Lastly, a class of critical states embedded in the continuum is uncovered in a one-dimensional optical waveguide array with one non-Hermitian defect. These states are on the verge of being fractal and have real propagation constants, exhibiting a phase transition from delocalization to localization as the imaginary part of the refractive index in the defect waveguide approaches a critical value.

ACKNOWLEDGMENTS

First, I would like to express my sincere gratitude to my advisor, Dr. Alexey Yamilov, for his continuous support of my Ph.D. study and related research, patience, motivation, and immense knowledge. His guidance helped me in all of my research and writing of this thesis. I could not have imagined having a better advisor and mentor for my Ph.D. study.

Besides my advisor, I would like to thank the rest of my thesis committee, Dr. Thomas Vojta, Dr. Paul Parris, Dr. Daniel Fishcer, and Dr. Xiaodong Yang, not only for their insightful comments and encouragement, but also for their questions, which motivated me to widen my research to various perspectives.

My sincere thanks also goes to Dr. George Waddill, Dr. Jerry Peacher, and Dr. Gerald Wilemski for their enormous support to overcome hard times during my graduate studies. Without their support, it would not be possible to conduct this research. My sincere thanks also goes to Dr. Hui Cao and Dr. Raktim Sarma for opportunities in their groups and leading me to work on diverse, exciting projects.

I thank my friends, Dr. Chandra M. Adhikari, Madhav Dhital, Sujan Bastola and Norsang Lama, for the numerous discussions we had during the last four years. Fond memories have been created with all the graduate students, faculty, and staff.

Nobody has been more important to me in the pursuit of this project than the members of my family. I would like to thank my father, Narayan, my mother, Radhika, and my sisters, Minu and Rabina, for dedicating their whole lives to the benefit of my success from day one. Most importantly, I owe a debt of gratitude to my loving, encouraging, and caring wife, Amrita, for her support throughout this journey.

TABLE OF CONTENTS

Page

PAPER

LIST OF ILLUSTRATIONS

PAPER V

LIST OF TABLES

SECTION

1. INTRODUCTION

1.1. LIGHT PROPAGATION

Light is present all around us, and it is the means by which we perceive the world. In a transparent medium, like glass or air, light propagates along a straight line. Although this is indeed the case, during the last leg of its journey to our eyes, tracing light back to the original source reveals a much richer behavior. The light which might have originated in the Sun, encounters many obstacles before reaching our eyes. It might be reflected, refracted, diffracted, scattered, or even absorbed and re-emitted along the way in the medium it is passing through. The light, which ends up reaching our eyes, may carry a lot of information about its journey. Propagation of light through homogeneous media can largely be understood through geometrical optics. Without presence of any obstacles, the propagation of light is ballistic (a ray of light travels straight through the medium without scattering). One common example of ballistic propagation is light passing through an opening of a cloud in the sky. The cloud, in contrast, is an inhomogeneous medium when light propagates through the cloud, the light interacts with water droplets. These obstacles can change its direction of propagation via the process called scattering of light as depicted in Figure 1.1. When light propagation is influenced by more than one obstacle, it is called "multiple scattering". On a cloudless day, we see the direct light from the Sun. When a cloud becomes thick enough, the Sun is no longer discernible, but we can still see less intense light. This is diffuse light coming from many directions. It propagates diffusely via a random walk-like fashion through the cloud and leaves it in random directions. The phenomena described in our example of light traversing a cloud in the sky did not incorporate the wave nature of

Figure 1.1. Scattering of light in a cloud

light. Such a treatment may or may not always be adequate as the propagation of waves in a scattering medium depends on various parameters. The shortest one is the wavelength of light λ, which depends on frequency f and speed of the wave in a medium $\upsilon(\lambda = \upsilon/f)$. Other parameters include the scattering mean free path ℓ_s, which is the average distance traveled by the wave between two scattering events; transport mean free path ℓ^*, which is the distance after which the wave loses the "memory" of its initial direction; and absorption length ℓ_a, which is the distance along the path over which the amplitude of the wave is strongly attenuated due to the presence of absorption inside the medium. The macroscopic absorption length ξ_a is the linear distance over which such attenuation occurs– the distance over which the amplitude of the wave is strongly attenuated due to the presence of absorption inside the medium see (Figure 1.2). Another important parameter is a thickness of the medium L. Propagation of light is predominantly ballistic (the wave travels straight through the medium without straying off the forward direction) when the sample size L is shorter or comparable to the scattering mean free path ℓ_s. In contrast, when light propagation is influenced by more than one obstacle, we enter the regime of multiple scattering.

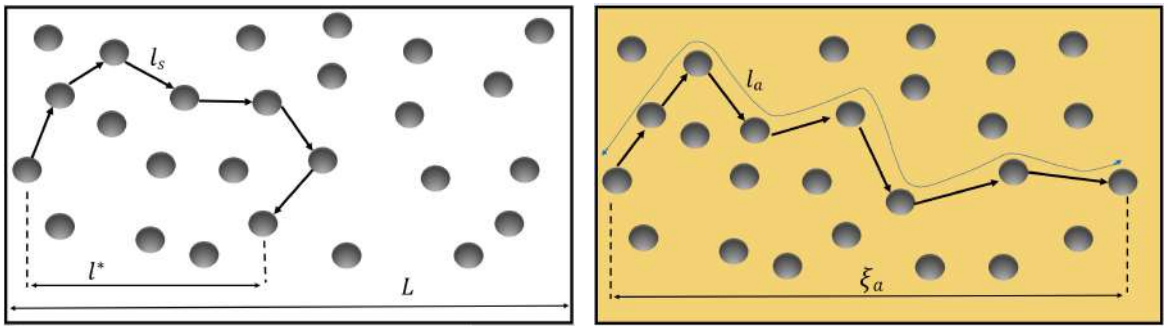

Scattering vs transport mean free path Ballistic vs diffusive absorption lengths

Figure 1.2. (a) Scattering mean free path, sometimes also referred to as scattering length, is the average distance between two consecutive scattering events. Transport mean free path, on the other hand, describes the distance over which photon's direction of propagation is randomized. (b) Attenuation of light is determined by distance traveled through an absorbing medium along the path, it is described by the (ballistic) absorption length. Attenuation depth also accounts for diffusive nature of propagation, it is determined by the parameter ξ_a.

When the sample size is large compared to ℓ_s, waves become multiply scattered and randomized due to a large number of scattering events along its path. Due to multiple obstacles, wave also travels longer inside the sample that may cause our geometrical optics picture become inadequate and fail because wave interference might become important. When the density of scatters inside a medium is very high, waves can even become localized (trapped) due to persistent interference with the new associated length scale- the localization length ξ.

1.2. DIFFUSION OF WAVES

Diffusion model works extremely well in describing wave propagation via multiple scattering that takes place in opaque media [1]. In these systems, a wave undergoes a large number of scattering events at random positions. One of the earlier motivations came from astrophysicists who were interested in how light propagates through nebulae and other

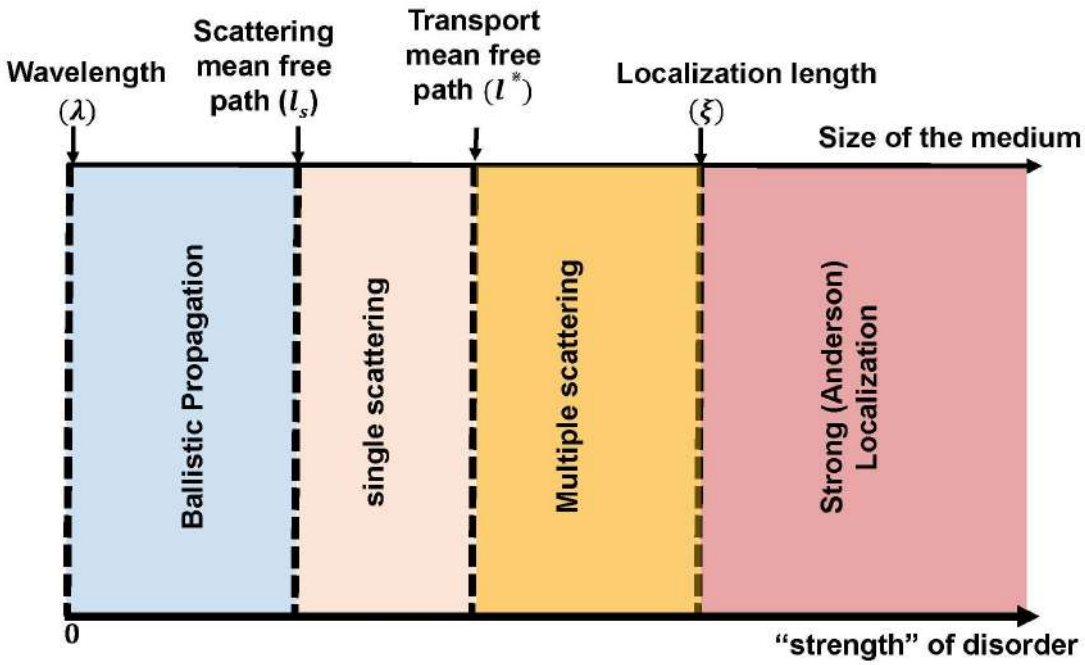

Figure 1.3. Regimes of scattering. Depending on relative length scales, a number of distinct regimes of wave propagation can be observed.

interstellar/stellar objects. These studies were early attempts to carefully observe how light diffuses inside systems and to extract information about the source of the light as well as the medium through which it propagated [2].

The history of process diffusion dates back to observations of irregular movement of particles in a fluid due to their collisions with other atoms or molecules. The first scientific description was provided by Robert Brown, who studied the motion of pollen in water. In 1905, Einstein provided both a mathematical description and a physical interpretation of this irregular motion, now known as Brownian random walk [3]. In Brownian motion, the movement of atoms and molecules in a liquid and gas is random, and over time larger particles will be driven to disperse evenly throughout the medium. Particles undergoing random walk will eventually explore all available space, although the average distance explored might increase quite slowly. The evolution of the probability to find, at any given point and at any given time, a particle that undergoes a Brownian random walk is given

by the diffusion equation. Importantly, this equation does not describe the microscopic irregular motion of each particle, but instead is a macroscopic description of the average motion. A visual example of the particle diffusion process is given by observing the process of dispersion of a drop of ink in a glass of water. Remarkably, the diffusion phenomenon, originally conceived for particles, has found to work very well for describing wave propagation in scattering media [4]. This is highly nontrivial because particle diffusion fundamentally differs from wave diffusion as latter the interference ("quantum" in case of electron propagation) effects. A visual example of wave diffusion process in depicted in Figure 1.4.

(a) Ballistic propagation (b) Diffusive propagation

Figure 1.4. (a) Ballistic regime is applicable to the optically thin systems when only a few scattering events occur and, thus, the original location of the source can be discerned. (b) Multiple scattering randomizes the directions of propagation completely, leading to diffuse propagation. The rainbow represents a separate single-scattering effect superimposed on top of the diffuse background.

1.3. MATHEMATICAL DESCRIPTION OF THE MULTIPLE SCATTERING OF LIGHT

Light is scattered by inhomogeneities in the medium, and when such inhomogeneities are randomly distributed, the multiple scattering path can be described as a random walk. We can have different regimes of scattering depending on relative length

scales and disorder strength as shown in Figure 1.3. The study of multiple scattering of light inside such a medium can be used as a proxy as it also applies to propagation of other waves, for example acoustic, seismic, or matter waves, behave in random media [5–7]. Although the diffusion equation is already sufficient to describe a wide range of wave transport phenomena [5], it fails to capture interference effects emerging from the multiple scattering. In this thesis, we go beyond the diffusion model to describe transport of light. The standard diffusion model neglects interference effects, which are always present, to a greater or lesser extent, in wave propagation. The idea of incorporating interference effects in wave propagation in random media, has yielded many interesting wave interference phenomena [5, 6, 8–10], that would be called quantum phenomena in context of electron propagation. In last several decades, remarkable results have been achieved in condensed matter physics, especially in the transport of electrons in conductors. The impurities in a conductor are randomly distributed, and scatter electrons, or more precisely de Broglie waves. Multiple scattering affects such a measurable quantity as conductance and, under certain conditions, it might become imperative to take into account the wave properties of the electrons inside the conductor. This field is known as mesoscopic physics. The study of coherent multiple scattering of light in disordered media presents experimental advantages compared to the problem of electron conduction. Indeed, the absence of coherence destroying effects such as de-phasing, means that experiments with light can be performed at room temperature. In another example, when light is illuminated upon a scattering medium and then is detected along some direction allows angular (directional) analysis of multiple scattering. Such a measurement is much more difficult, if not impossible, in the case of electrons. Furthermore, development of lasers provided a common source of extremely coherent light, which is easily tunable, so that the statistical ensemble can be obtained by simply changing the light wavelength.

In context of this thesis, it is enlightening to express physical quantities related to wave scatterings in terms of products of complex amplitudes, $a(\mathbf{r},\mathbf{r}')$. $a(\mathbf{r},\mathbf{r}')$ is complex amplitude of a propagating trajectory from $\mathbf{r}'$ to $\mathbf{r}$. The average of product of two complex amplitudes is related to the average probability $P(\mathbf{r},\mathbf{r}')$ of propagation from point $\mathbf{r}'$ to point $\mathbf{r}$:

$$P(\mathbf{r},\mathbf{r}') \propto \overline{\sum_{i,j} a_i^*(\mathbf{r},\mathbf{r}')a_j(\mathbf{r},\mathbf{r}')}. \tag{1.1}$$

We can decompose the total sum of trajectories as in Eq. 1.1 into two components:(1) with identical trajectories and (2) different trajectories i, j:

$$P(\mathbf{r},\mathbf{r}') \propto \sum_j \overline{|a_j(\mathbf{r},\mathbf{r}')|^2} + \overline{\sum_{i\neq j} a_i^*(\mathbf{r},\mathbf{r}')a_j(\mathbf{r},\mathbf{r}')}. \tag{1.2}$$

It is tempting, and usually safe to assume, that different trajectories result in different phase and their contributions vanish on averaging, leading to vanishing of the second term in Eq. 1.2. Hence, the probability, in our case average intensity $I(\mathbf{r},\mathbf{r}')$, is only due to identical trajectories.

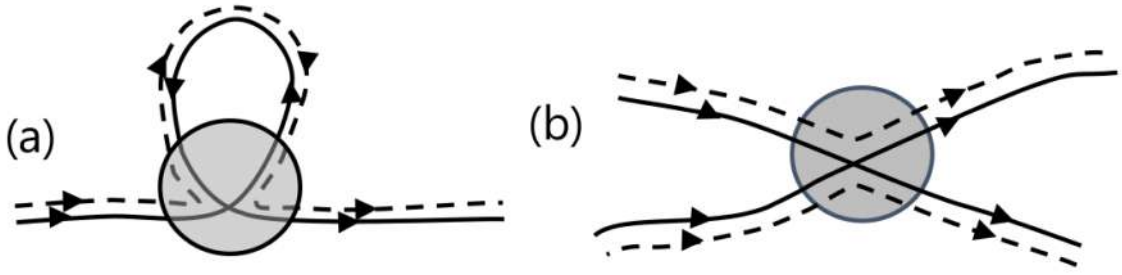

Figure 1.5. Self-crossing of one (a), or a crossing between two pairs of trajectories result in interference effect that do not vanish after statistical averaging [6]

Eliminating the second term of Eq. 1.2 neglects all interference effects in the course of wave propagation. Figure 1.5(a) shows two trajectories (solid line representing a and dashed line representing a^*) in a medium following the same sequence of scatterings with one crossing, forming a loop with counter propagating trajectories. Even after averaging over disorder, this contribution from the loop is not zero because the two trajectories travel along

identical paths accumulating identical phase and, thus, always interfering constructively. The loop is an example of how statistical average might not completely suppress information about interference effects. Figure 1.5(b) shows another example involving one crossing, which mixes four complex amplitudes and pairs them in different way. The crossing is called a *Hikami box*, which is an object which permutes amplitudes and makes intensities correlated everywhere along trajectories after the crossing [6].

1.4. CORRELATION FUNCTION

Interference, not captured by diffusive description, is the key to explaining a number of remarkable effects in mesoscopic physics, optics, acoustics, and other fields dealing with wave propagation in complex scattering media. One of such effects is correlation between intensity measured at two different locations (also at different outgoing angles, or frequencies). One prominent example of spatial correlation of intensity is speckle pattern. Due to presence of disorder, the intensity distribution of a light wave undergoing multiple scattering yields random distribution of dark and bright spots– a speckle pattern [11]. It is an interference pattern, which depends on disorder configuration and it reflects the fundamental "graininess" of wave field at the scale of wavelength. Speckle patterns are common– place, they are observed when intensity is measured spatially or as a function of angle.

To understand the structure and meaning of the correlation function, let us consider its diagrammatic contributions in terms of four plane waves: two incident along directions $S_{\hat{a}}, S_{\hat{a}'}$ and two emerging along $S_{\hat{b}}, S_{\hat{b}'}$. Here, we consider a slab of thickness L. We can measure normalized intensity T_{ab} transmitted in the direction $\hat{S}_b$ and corresponding to a wave incident in the direction $\hat{S}_a$ as in Figure 1.6. Average transmission coefficient, $\overline{T_{ab}}$ depends only slightly on the directions $\hat{S}_a$ and $\hat{S}_b$. The angular correlation of the speckle is

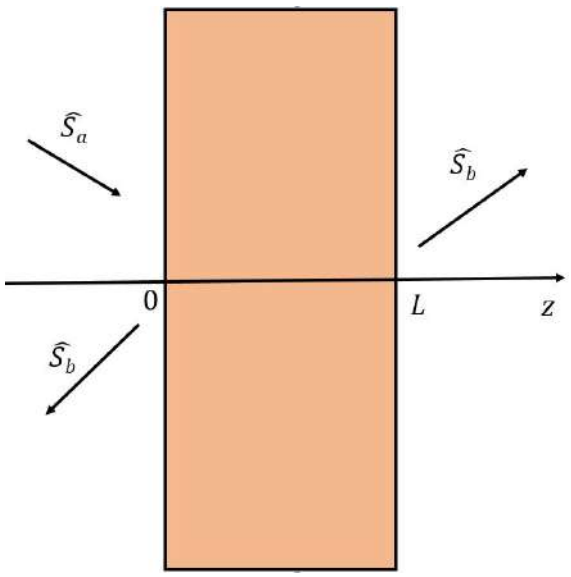

Figure 1.6. Schematic diagram to define reflection and transmission coefficients through a slab of thickness L.

defined by

$$C_{aba'b'} = \frac{\overline{\delta T_{ab} \delta T_{a'b'}}}{\overline{T_{ab}}^2}. \tag{1.3}$$

where $\delta T_{ab} = T_{ab} - \overline{T_{ab}}$. The fluctuation of the speckle pattern, for a specific angle of incidence direction $\hat{s}_a$ are given by $C_{aaaa} = \frac{\overline{\delta^2 T}}{\overline{T}^2}$ which is equal to 1 in diffusive medium [6], yielding

$$\overline{T_{aa}^2} = 2\overline{T_{aa}^2}.$$

This result describes the most visible aspect of a speckle pattern, with relative fluctuations of the order of unity, it is a consequence of Rayleigh distribution of transmitted intensities.

The correlation function defined in Eq. 1.3 is the product of four complex amplitudes as depicted in Figure 1.7(a). They are due to four complex fields entering the definition in Eq. 1.3, two complex conjugated pairs, one per intensity. The pairing of complex amplitudes is performed to obtain two intensities at the end points, but inside the medium, they fields can propagate via a multitude of different paths, and thus can result in many contributions. Such pairings can be classified [5, 12] into the four main groups of to contributions $(b - e)$

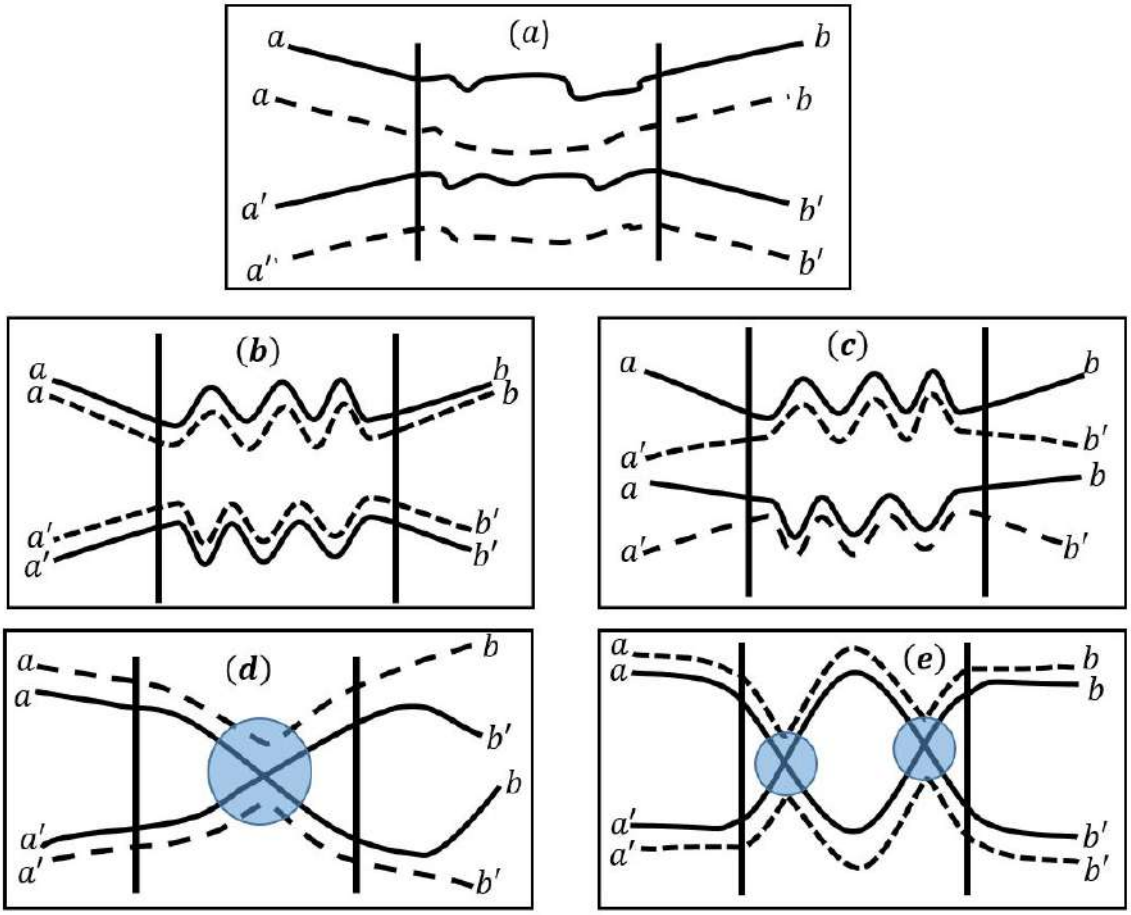

Figure 1.7. (a) Correlation function is built from four complex amplitudes corresponding to four incoming and outgoing plane waves. (b) and (c) are the contributions obtained by pairing amplitudes in pairs without swapping the order of pairing. Contribution (d) contains one quantum crossing, while (e) has two quantum crossings, each of which incurs swapping pairings of the four trajectories.

in Figure 1.7. The classification originates from the role played by the interference of waves inside medium. The diagram in Figure 1.7 (b) corresponds to two intensities propagating independently through the system, it is the term which is being subtracted off when defining δT_{ab}. The correlation function is decomposed into its components depending on number of interference events, which, in context of electronic wave transport in condensed matter systems, are "quantum" crossings of paths– the remaining three diagrams, Figure 1.7(c-e).

1.4.1. Short-Range $C^{(1)}$ Correlation. Figure 1.7(c) depicts the principal contribution to the correlation function Eq. 1.3 denoted by $C^{(1)}_{aba'b'}$. It is appreciable only if $\hat{S}_a - \hat{S}'_a = \hat{S}_b - \hat{S}'_b$ and it decays exponentially otherwise. This contribution corresponds to the following pairing

$$C^{(1)} : (aa')(aa') \rightarrow (bb')(bb').$$

If the angle of an incoming beam is changed, the speckles follow the incoming beam– the so-called memory effect. Second, the speckle pattern also deforms, it decorrelates. The $C^{(1)}$ correlation is a sharply peaked function, nonzero only if the angles of the incoming and outgoing channel are changed by the same amount. Theoretical studies of $C^{(1)}$ were first done by Shapiro [13]. Experimental work on $C^{(1)}$ was then carried out to study memory effect [14]. Frequency dependence of short-range correlation is studied by Lagendijk et. al. [15]. The effects of absorption and internal reflection in $C^{(1)}$ is studied in ref [16, 17].

1.4.2. Long-Range $C^{(2)}$ Correlation. It is also possible to pair the amplitudes by interposing them in one or more quantum crossings. One of the such possibility is $C^{(2)}_{aba'b'}$, it has one crossing and is shown in Figure 1.7(d). The crossing leads to an exchange of the channels a and a' or b and b' which can be represented by

$$C^{(2)} = \begin{cases} (aa)(a'a') \rightarrow (bb')(bb'), \\ or \\ (aa')(aa') \rightarrow (bb)(b'b'). \end{cases}$$

The contribution $C^{(2)}$ to the correlation decreases and vanishes only if both $\Delta\hat{S}_a$ and $\Delta\hat{S}_b$ are large. For a speckle pattern generated from a single incident beam $a = a'$, we expect to observe long–range (for b not equal to b') angular correlations of weak amplitude. Smallness of this contribution arises from the additional requirement for two paths to cross which is usually a rare event.

The $C^{(2)}$ term can be measured more easily in a setup using one incoming channel (e.g. angle of incidence) and integrating over all outgoing channels. This is because this type of correlation (when b and b' are automatically paired) is present in all channels so that the addition makes $C^{(2)}$ the dominant contribution. The long-range character of the $C^{(2)}$ arises due to interference of the diffuse light paths [17]. The long-range correlation function was first introduced by Stephen and Cwilich [18]. The Langevin approach simplified the calculation of correlation functions [19]. Zyuzin and Spivak applied the Langevin approach to calculate the correlation functions of light transmitted through and reflected from disordered samples [20]. The long-range correlation function was obtained experimentally for various systems: including optical systems [15, 21, 22] and microwave waveguides [23, 24].

1.4.3. Infinite-Range $C^{(3)}$ Correlation. The contribution $C^{(3)}_{aba'b'}$ with two crossings is depicted in Figure 1.7(e). Because of the two-crossing structure, this contribution has no angular dependence,(i.e. it yields a uniform background to the correlation function for any aa' and any bb'). This result is characteristic of coherent multiple scattering of the combined effect of quantum crossings and of their non-local propagation. Upon averaging over all directions of incident and emergent waves, this contribution not only survives, but it becomes dominant. This is the celebrated universal conductance fluctuation [25–28].

The correlation function is thus decomposed into its components depending on number of interference events or, on a more fundamental level, on the type of pairing of the incoming and outgoing wave amplitudes that, in context of electronic wave transport in condensed matter systems, are "quantum" crossings of the paths. Thus, the three terms to the correlation function, in the decreasing order of contribution, are

$$C(\mathbf{r},\mathbf{r}') \approx C_1(\mathbf{r},\mathbf{r}') + C_2(\mathbf{r},\mathbf{r}') + C_3(\mathbf{r},\mathbf{r}'). \tag{1.4}$$

1.5. TRANSMISSION EIGENCHANNELS

Another striking interference effect is the existence of eigenchanels, first predicted by Dorokhov [29] in 1984. His work suggested existence of particular incident wavefronts, which can transmit through scattering media with near unity transmittance. He calculated the statistical distribution of transmission eigenvalues and predicted the existence of these so-called open eigenchannel, the system-specific wavefronts with unity transmittance [8, 30]. Each eigenchannel can be excited by a linear combination of multiple free-space incident modes. These incident wave-fronts when coupled to an open eigenchannel can be fully transmitted through a lossless disordered sample, even if the sample is optically thick (i.e. when the sample thickness is much greater than the transport mean free path). In contrast, waves injected into low-transmission (closed) channels with a transmission coefficient of close to zero barely penetrate the medium and are mostly reflected. In this thesis, we explore the idea manipulating the perfectly transmitting eigenchannels (open channel) by constructing different shapes of the disordered medium.

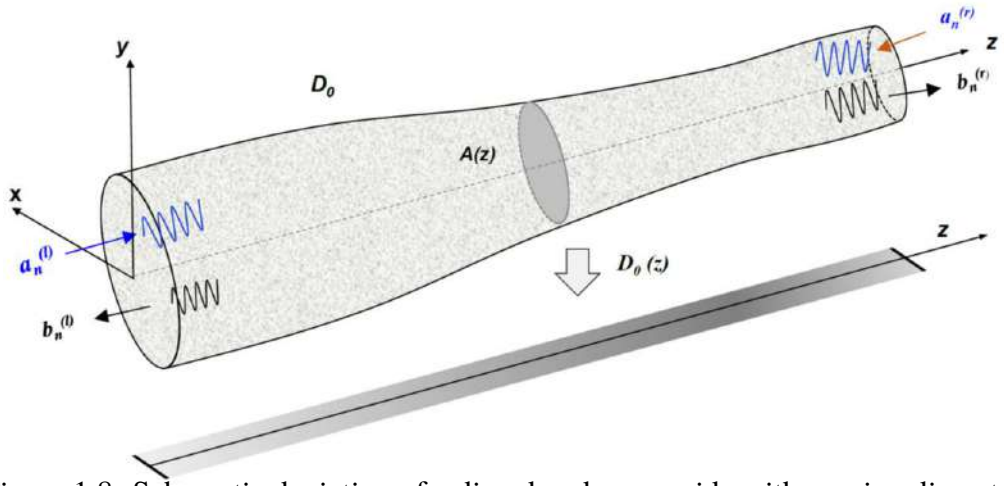

Figure 1.8. Schematic depiction of a disordered waveguide with varying diameter.

To construct the transmission matrix t of the disordered waveguide, we use guided modes in the leads as the basis. The input (output) lead waveguide has a constant width equal to the same width $W_1(W_2)$ of the disordered waveguide with an index of refraction n, at the front (back) end $z = 0$ ($z = L$), and it supports $M = W_1/(\lambda/2n)$ ($N = W_2/(\lambda/2n)$

guided modes. Thus t is a $N \times M$ matrix, and its element t_{ij} represents the field transmission from the input j^{th} mode to the output i^{th} mode. The reflection matrix is constructed in a similar way by computing the reflected waves, and its dimension is $M \times M$. A singular value decomposition of the transmission matrix t gives $t = U\Lambda V^{\dagger}$. Λ is a $N \times M$ diagonal matrix with $min[N, M]$ non-negative real numbers, $\tau_m^{1/2}$, where τ_m is the eigenvalue of $t^{\dagger}t$ and represents the transmittance of the m^{th} transmission eigenchannel. U is a $M \times M$ unitary matrix that maps the field in the guided modes of the input lead to the eigenchannels of the disordered waveguide, and V is a $N \times N$ unitary matrix that maps the eigenchannels to the output waveguide modes. Each column of V represents an input singular vector, whose elements are the complex coefficients for the input waveguide modes that combine to couple light into a single transmission eigenchannel. The output field of a single transmission eigenchanel is represented by the column of U, which is called the output singular vector. Similarly, the reflection eigenvalues ρ_m can be obtained by singular value decomposition of the reflection matrix r. The dimensionless conductance is $g = \langle Tr(\hat{t}^{\dagger}\hat{t})\rangle = \sum_n \langle \tau_n \rangle$. The density of the eigenvalues $P(\tau)$ has a bimodal distribution [8, 22, 29, 31, 32], with one peak at $\tau \approx 0$ that corresponds to the closed channels, and a peak at $\tau \approx 1$ that corresponds to the open channels.

$$P(\tau) = \frac{g_0}{2} \frac{1}{\tau\sqrt{1-\tau}}. \tag{1.5}$$

In this thesis, we will show that for a waveguide with an arbitrary shape, this expression remains appropriate, if $g_0 = \frac{k\ell}{2}\left[\int_0^L W^{-1}(z)dz\right]^{-1}$ depends on geometry of the waveguide, where $k = 2\pi/\lambda$ is the wave number, ℓ is the transport mean free path. We obtain this result by reducing arbitrary $2D$ or $3D$ waveguide to the $1D$ waveguide by projection technique [22, 33] see Figure 1.8. We propose a model to describe transmission eigenchannels for arbitrary waveguide profiles and develop an inverse design technique to obtain waveguide profiles for the desired eigenchannel profile.

1.6. FOCUSING CONTRAST

Scientific instruments like telescopes, microscopes, and cameras all work on the notion of easily predictable ballistic propagation of light. But, for a turbid medium, light propagation is not ballistic and its direction gets scrambled due to scattering on the inhomogeneities. Hence, it is not immediately clear how we can get a sharp focus inside turbid medium. The majority of imaging methods (coherence gating, multi-photon microscopy) depend on the ballistic light to form an image [34–38], but the intensity of the ballistic light decreases exponentially with depth of penetration. Therefore, with increasing depth, it becomes progressively (exponentially) more difficult to retrieve information that would be useful in imaging.

Recent investigations of wavefront shaping offered a radically new approach to light focusing inside scattering medium. One such method is the iterative method which was developed by Mosk and Vellekoop to focus light through [39] or even inside scattering objects [40]. Waves propagating inside a random medium (with exponentially small ballistic component), which are completely scattered, ordinarily generate a strongly fluctuating spatial distribution of intensity (speckle pattern) [1, 6, 12] having no apparent relation to the incident waveform. However, despite such a superficial randomness, light propagation in a linear complex medium is completely deterministic. Therefore, intensity can potentially be focused at any point inside the medium by adjusting the phase and amplitude of all sources of the wave so that the constructive interference of all partial waves takes place at the selected point. It has since been convincingly demonstrated that light can indeed be focused, albeit not perfectly due to experimentally limitations, through a random slab in both space and time by manipulating the incident fields [41].

The spatial profile of focused intensity inside the medium does depend upon the random medium, location with respect to the boundaries, as well as upon the incident field. To understand the process and limitations of focusing via wave-front shaping, a complete set of the N orthogonal eigenchannels of the transmission matrix and their associated transmission

eigenvalues τ_n is used. As discussed previously, the field transmission matrix t relates the fields E_a and E_b between incoming a and outgoing b waveguide modes with $E_b = \sum_a^N t_{ba} E_a$; whereas the transmission matrix eigenchannels represent an alternative basis for representing the electric fields inside the medium [41–43]. Furthermore, focusing in/through random media is intrinsically related to the correlation and the fluctuations of transmitted intensity [41]. Intensity correlation across the transmitted speckle pattern persists beyond the range over which the field is correlated [14, 18, 23, 44, 45] and may be characterized through the degree of intensity correlation κ [46] related to $C^{(2)}$ correlations introduced previously. Correlation in intensity and fluctuations of total transmission normalized by its ensemble average $s_a = T_a/\langle T_a \rangle$, where $T_a = \sum_b^N |t_{ba}|^2$ are linked via the equality $\kappa = var(s_a)$ for $N \gg \kappa$. κ is also inversely proportional to the dimensionless conductance g [12] because $C^{(2)}$ correlation requires one crossing of paths. The conductance g is in fact the ensemble average of the optical transmittance $g = \langle T \rangle = \langle \sum_{a,b}^N |t_{ba}|^2 \rangle = \langle \sum_{n=1}^N \tau_n \rangle$ [47].

Focusing with maximum intensity at a point β for a normalized incident field is achieved by phase conjugating the field transmission coefficient between the target point at β and input points a so that the incident field is $E_a = t_{\beta a}^* / \sqrt{\sum_a t_{\beta a}^2} = t_{\beta a}^* / \sqrt{T_\beta}$. Components of the transmitted field originating from different points then interfere constructively at β to give the focused intensity, which is equal to the total transmission through the opposite surface for a source at β, $I_\beta = \sum_a |t_{\beta a}^2|^2 / T_\beta$. If M incoming channels is such that $M \ll N$, where N is the number of independent components supported in the space surrounding the medium, $\langle I_\beta \rangle$ is only enhanced by a factor M over $\langle I \rangle$, $\langle I_\beta \rangle = M \langle I \rangle = Mg/N^2$. On the other hand, the background intensity at points $b \neq \beta$ is $I_b = |\sum_a t_{ba} t_{\beta a}^*|^2 / T_\beta$. Decomposing the field into orthonormal incoming and outgoing singular vectors v_n and u_n, respectively, t can be written as $t = U \Lambda V = \sum_{n=1}^N u_n \tau^{1/2} v_n^\dagger$. The singular vectors v_n and u_n are the waveforms at input and ouput surfaces, respectively, which couple selectively to the n^{th} eigenchannel propagating through the medium. The focused and background intensities

can now be expressed in terms of the singular vectors:

$$I_\beta = \sum_n \tau_n |u_{n\beta}|^2 \tag{1.6a}$$

$$I_b = \frac{|\sum_n \tau_n u_{nb} u^*_{n\beta}|^2}{T_\beta} \tag{1.6b}$$

Since the background intensity is the result of interference between randomly phased statistically independent elements associated with different eigenchannels, the contrast $\mu_M \leq \langle I_\beta / I_b \rangle$ depends on the effective number of eigenchannels contributing to the transmission. The average of the contrast(i.e. ratio) between the peak and background intensity for M input points is [43]:

$$\mu_M = \frac{1}{\frac{1}{1+1/N_{eff}} - \frac{1}{M}} \tag{1.7}$$

where $N_{eff} \equiv \langle (\sum_{n=1}^N \tau_n)^2 / \sum_{n=1}^N \tau_n^2 \rangle$, and the eigenchannel participation number of the transmission matrix is the effective number of uncorrelated speckle patterns contributing to the transmitted field. The eigenchannel participation number N_{eff} may be directly linked to fluctuations and correlations of intensity for diffusive waves for quasi-one-dimensional samples. Indeed, the correlation of intensity and fluctuations of total transmission normalized by its ensemble average $s_a = T_a / \langle T_a \rangle$ are linked with $\kappa = var(s_a)$. For $N \gg 1$:

$$var(s_a) = \kappa = 1/N_{eff}$$

Therefore, the average intensity pattern for focused waves normalized to the value at the focus can be written to give the spatial variation of the normalized intensity pattern with the displacement Δr in terms of $\kappa \propto C^{(2)}$:

$$\frac{\langle I_{foc}(\Delta r) \rangle}{C^{(1)} \langle I \rangle} = \frac{C^{(1)}(\Delta r) + \kappa}{1 + \kappa} \tag{1.8}$$

This relationship explicitly shows that importance of intensity correlations, specifically, the long-range correlation, extends far beyond studies of mesoscopic transport, it plays the key role in setting the fundamental limits for wavefront shaping applications [41–43, 48, 49].

1.7. PROJECTION METHOD IN 2D AND 3D WAVEGUIDES WITH ABSORPTION

Recently, two theoretical models have been put forward to describe the spatial profile of the perfectly transmitting channels in lossless diffusive media. Davy et al. [50] applied the supersymmetry theory to wave propagation in a quasi-one-dimensional random system and related the intensity profile to the return probability (RP) of diffusive waves. Ojambati et al. [51, 52] proposed that the perfectly transmitting channel in a disordered slab is related to the fundamental mode (FM) of the one-dimensional (1D) diffusion equation. Although both models correctly predict the depth of the maximum energy density [50, 53–55], they disagree quantitatively in terms of the depth profile for the perfectly transmitting channel. So far, both models have been applied only to one-dimensional diffusion.

We have studied light transport in quasi-two-dimensional disordered systems and showed that the spatial structure of transmission eigenchannels can be modified by the confinement geometry [56]. For example, by adjusting the shape of the reflecting boundary of a disordered waveguide, the depth at which the energy density of a high transmission channel reaches the maximum can be displaced. This enables enhanced light-matter interaction at different location inside the random medium.

In this part of the thesis, we use the projection technique, developed in physical chemistry for particle diffusion in confined geometries [22, 33], to describe wave diffusion. With the help of projection technique, we derive expressions for the Green function in the two- and three-dimensional disordered waveguides with an arbitrary shape in order to obtain the non-local long-range mesoscopic correlations [12, 18, 20, 23, 48, 57–60].

We reduce the problem to one-dimension and obtain an analytical solution. We further extend the projection technique to include the effects of absorption commonly encountered in experiments with the electromagnetic waves.

PAPER

I. DETECTION OF A DIFFUSIVE CLOAK VIA SECOND-ORDER STATISTICS

Milan Koirala and Alexey Yamilov

Department of Physics Missouri University of Science and Technology, Rolla, Missouri 65409

ABSTRACT

We propose a scheme to detect the diffusive cloak proposed by Schittny et al [Science 345, 427 (2014)]. We exploit the fact that diffusion of light is an approximation that disregards wave interference. The long-range contribution to intensity correlation is sensitive to locations of paths crossings and the interference inside the medium, allowing one to detect the size and position, including the depth, of the diffusive cloak. Our results also suggest that it is possible to separately manipulate the first- and the second-order statistics of wave propagation in turbid media.

1. INTRODUCTION

A cloak conceals an object by molding the the flow of light in the surrounding volume [1]. Transformation optics [2, 3] has enabled one to design artificial materials with spatially varying permittivity and permeability to achieve cloaking effect, see Figure 1(a). In the following we will refer to this scheme as a ballistic cloak. A different kind of cloak has been proposed by Schittny et al [4, 5] – a reflecting object is hidden inside a turbid

medium where the light propagates diffusively, i.e. via a random walk, see Figure 1(b). The effect is achieved by properly increasing diffusivity of the shell D'. Hiding an object inside a scattering medium is usually not difficult – it suffices to bury an object at the depth of several transport mean free paths – in fact, the opposite task of detecting an inhomogeneity, such as a cancer, is the holy grail of biomedical optics [6]. Notwithstanding, it has been pointed out that in Ref. [4] that cloaking effect can be achieved for a shallow object and with a thin cloak made of a statistically uniform material. Furthermore, the cloak is omni-directional and broadband. This behavior can be understood by realizing that the light intensity in turbid medium is governed by the diffusion equation, which is much simpler than Maxwell equations for the ballistic cloak. Laplace equation describing the diffusion is formally equivalent to that of electric/magnetic potential in the electro-/mangneto- statics. In the latter context, core-shell structures have been known to preserve the uniformity of electric [7]/magnetic [8] field lines in both two (cylinder) and three (sphere) dimensions. In context of light diffusion, it suggests that the proper choice of diffusion constant ensures the uniform intensity at the output surface of a slab containing the cloak. This result has been verified in Ref. [4] and further extended to heat cloaking [9, 10].

The cloak in Figure 1 b is based on the diffusive description of wave transport. This is an approximation, which does not take into account wave interference effects [11, 12]. Second-order statistical properties such as fluctuations and correlations of intensity contain information about wave nature of transport, including the location where wave interference took place [13]. We consider spatial intensity correlations defined as $C(\mathbf{r}_1, \mathbf{r}_2) = \langle \delta I(\mathbf{r}_1) \delta I(\mathbf{r}_2) \rangle / \langle I(\mathbf{r}_1) \rangle \langle I(\mathbf{r}_2) \rangle$, where $\delta I(\mathbf{r}) = I(\mathbf{r}) - \langle (I(\mathbf{r}) \rangle$ is the deviation from the mean. $\langle ... \rangle$ denotes ensemble average that is accomplished by e.g. averaging over wavelength of the source. The correlation is dominated by a short-range (on the order of transport mean free path, ℓ) contribution $C_1(\mathbf{r}_1, \mathbf{r}_2)$ responsible for speckles [14]. In this work,

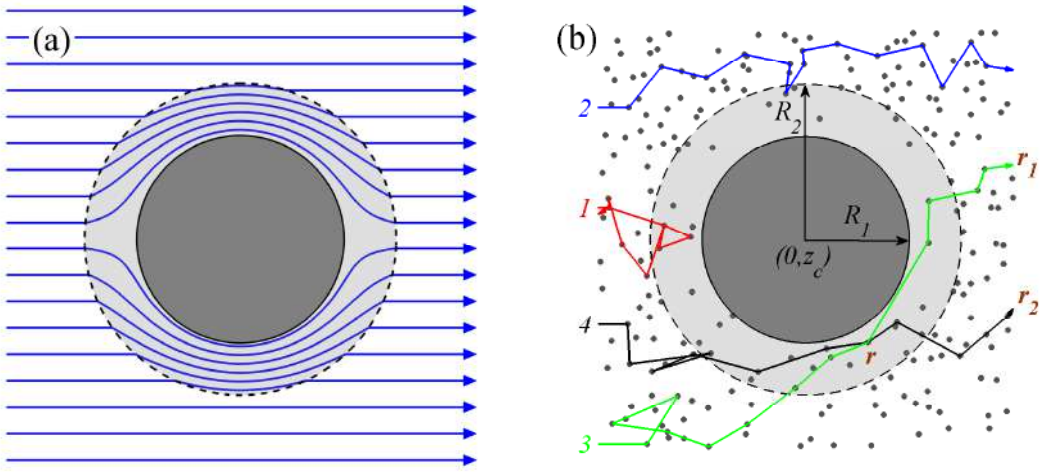

Figure 1. (a) Schematic depiction of light paths in a ballistic cloak. Gray shell depicts the area where material properties have been modified based on principles of transformation optics to mold the flow of light around the obstacle. (b) Diffusive cloak compensates the longer paths around the object by the increased diffusivity (e.g. lower scatterer density) in the surrounding shell.

we present a method for detecting the size and location of an object concealed by the diffusive cloak based on analysis of the long-range component of correlation [15–18] $C_2(\mathbf{r}_1,\mathbf{r}_2) \simeq C(\mathbf{r}_1,\mathbf{r}_2) - C_1(\mathbf{r}_1,\mathbf{r}_2)$ measured at the output surface of a slab of turbid medium.

2. MODEL

We consider coherent plane-wave illumination of a slab of lossless $2D$ turbid medium of thickness L and transport mean free path ℓ. Our goal is to compare the intensity and the long-range correlation in a slab (the reference) to those in slab with an embedded reflecting cylinder (case I); and in slab with the cylinder surrounded by diffusion cloak (case II).

To compute ensemble-averaged intensity we solve diffusion equation

$$D\nabla^2\langle I(\mathbf{r})\rangle = 0 \tag{1}$$

with boundary conditions $\langle I(y,0)\rangle = I_0$ and $\langle I(y,L)\rangle = 0$. $\mathbf{r} = (y,z)$ where y and z are the transverse and longitudinal coordinates respectively. For cases with inclusions, we represent the solution as:

$$\langle I(\mathbf{r})\rangle = \langle I^{(0)}(\mathbf{r})\rangle + \langle \Delta I(\mathbf{r})\rangle \tag{2}$$

where $\langle I^{(0)}(\mathbf{r})\rangle$ is the solution of diffusion equation in pure slab and $\langle \Delta I(\mathbf{r})\rangle$ is correction in intensity due to the inclusion. To obtain an analytical expression for correction term, we use method described in Ref. [19]. For an object located at $\mathbf{r}_c$ inside the medium, the intensity can be described by a multipole expansion, in analogy with electrostatics [19–21], where electric potential also satisfies Laplace equation. For a lossless medium, the lowest order dipole term describes disturbance of the intensity far enough from the object can be written as

$$\langle \Delta I(\mathbf{r})\rangle = \mathbf{p}\cdot\nabla_{\mathbf{r}_c} G^{(0)}(\mathbf{r},\mathbf{r}_c), \tag{3}$$

where $G^{(0)}(\mathbf{r},\mathbf{r}')$ is Green function for the pure slab, i.e. it is solution of $\Delta_{\mathbf{r}} G^{(0)}(\mathbf{r},\mathbf{r}') = -\delta(\mathbf{r}-\mathbf{r}')$ with zero boundary conditions at the slab boundaries. The dipole moment in Eq. 3 is induced by the incident intensity so that $\mathbf{p} = -P\,\nabla_{\mathbf{r}_c}\langle I^{(0)}(\mathbf{r}_c)\rangle$. Intrinsic "polarizability" for a reflecting cylindrical inclusion $P^{(I)} = 2\pi R_1^2$ can be found by applying proper boundary conditions at the cylinder surface [21]. Using same method for the core-shell structure we find

$$P^{(II)} = 2\pi R_2^2 \times \frac{(R_2^2+R_1^2)/(R_2^2-R_1^2) - D'/D}{(R_2^2+R_1^2)/(R_2^2-R_1^2) + D'/D}, \tag{4}$$

where $R_{1,2}$ are inner and outer radii of the shell and D' is diffusion coefficient of the shell. It is implicitly assumed that the size of the inclusion is much greater than ℓ. Lastly, the position-resolved intensity transmitted through the slab can be found from the diffuse flux at the output surface, where c denotes speed of light.

$$I_T(y) = (1/c)J(\mathbf{r})\rangle|_{z=L} = -(D/c)\nabla_z\langle I(\mathbf{r})\rangle|_{z=L}, \tag{5}$$

Using Langevin approach [17, 22, 23], the long-range intensity correlation $C_2(\mathbf{r}_1;\mathbf{r}_2)$ has been related to the ensemble average intensity $\langle I(\mathbf{r})\rangle$ and Green function $G(\mathbf{r};\mathbf{r}')$ of diffusion equation as

$$C_2(\mathbf{r}_1,\mathbf{r}_2) = \frac{4}{k_0\ell}\frac{\int_\Omega d\mathbf{r}\ \nabla_{\mathbf{r}}G(\mathbf{r}_1,\mathbf{r})\cdot\nabla_{\mathbf{r}}G(\mathbf{r}_2,\mathbf{r})\langle I(\mathbf{r})\rangle^2}{\langle I(\mathbf{r}_1)\rangle\langle I(\mathbf{r}_2)\rangle}. \tag{6}$$

In the Langevin approach, proposed in the context of mesoscopic electron transport by Spivak and Zyuzin [24], the long-range correlations are obtained from the short-range ($\delta\mathbf{r} \le \ell$) correlations for fluxes. The result in Eq. 6 is due to wave interference of paths with crossings in Figure 1 b; its wave nature is seen from the $(k_0\ell)^{-1}$ factor, where $k_0 = 2\pi/\lambda$ is the wave number. As in Eq. 1, Eq. 6 neglects surface corrections [22], which are small in the limit $L \ge \ell$ considered in this work. The integration in Eq. 6 is taken over the entire volume of the system Ω.

In analogy with in Eqs. 2,3, Green function in systems with inclusions can be found as

$$G(\mathbf{r},\mathbf{r}') = G^{(0)}(\mathbf{r},\mathbf{r}') - P\ \nabla_{\mathbf{r}_c}G^{(0)}(\mathbf{r}_c,\mathbf{r}')\cdot\nabla_{\mathbf{r}_c}G^{(0)}(\mathbf{r},\mathbf{r}_c)\,. \tag{7}$$

In what follows, we use Eqs. (2,6) to compute the diffuse intensity and long-range correlation for the three cases of interest.

3. DIFFUSE INTENSITY

For a slab without inclusions illuminated by a plane wave, solution of diffusion equation is a linear function and the Green function can be easily found by e.g. Fourier transformation over the transverse variable [12]

$$\langle I^{(0)}(\mathbf{r})\rangle = \langle I^I(z,L)\rangle = I_0(1 - z/L) \tag{8}$$

$$G^{(0)}(\mathbf{r},\mathbf{r}') = -\int_{-\infty}^{\infty} \frac{\sinh[kz_<]\sinh[k(L-z_<]}{k\sinh[kL]} e^{ik(y-y')}\frac{dk}{2\pi}, \tag{9}$$

where $z_< = \min[z,z']$, and $z_> = \max[z,z']$. Diffuse intensity in the presence of a reflecting cylinder at $\mathbf{r}_c = (z_c, y_c \equiv 0)$ can be found by substituting Eqs. (8,9) into Eq. 3

$$\begin{aligned}\langle \Delta I^{(I)}(\mathbf{r})\rangle = -\frac{P^{(I)}I_0}{4L^2}\Bigg(&\frac{\sin[\pi(z-z_c)/L]}{\cosh[\pi y/L]-\cos[\pi(z-z_c)/L]}\\ &+\frac{\sin[\pi(z-(L-z_c))/L]}{\cosh[\pi y/L]-\cos[\pi(z+z_c)/L]}\Bigg).\end{aligned} \tag{10}$$

This negative correction scales as a ratio between the area πR_1^2 of the inclusion and square of the thickness of the slab. It leads a shadow directly behind the cylinder that was studied both experimentally and theoretically in Ref. [19] where Eq. 10 was also obtained.

To cloak a cylindrical inclusion, Ref. [4] proposed to modify the diffusion coefficient in the surrounding cylindrical shell as

$$D'/D = (R_2^2 + R_1^2)/(R_2^2 - R_1^2). \tag{11}$$

Under this cloaking condition, the polarizability in Eq. 4 vanishes and our method confirms that indeed

$$\langle \Delta I^{(II)}(\mathbf{r})\rangle = 0. \tag{12}$$

4. LONG-RANGE INTENSITY CORRELATION

For a slab, the long-range correlation is found by substituting Eqs. (8,9) into Eq. 6. For observation points at the output surface a compact expression has been obtained [17]

$$C_2^{(0)}(y_1,L;y_2,L) = \frac{1}{k_0\ell}\int_{-\infty}^{+\infty}\frac{dk}{2\pi}\frac{-2kL+\sinh(2kL)}{k\sinh^2(kL)}\cos[k(y_1-y_2)], \tag{13}$$

which we use as a reference. Presence of a reflecting cylinder can be treated perturbatively, it introduces corrections of two types

$$\Delta C_2^{(I)}(\mathbf{r}_1, \mathbf{r}_2) \simeq \frac{1}{k_0 \ell} \frac{P^{(I)}}{L^2} F(\mathbf{r}_1, \mathbf{r}_2) + \Delta C_2^{EV}(\mathbf{r}_1, \mathbf{r}_2). \tag{14}$$

The first term is the leading term due to $\langle \Delta I(\mathbf{r}) \rangle$ and $\Delta G(\mathbf{r}, \mathbf{r}')$ in Eqs. (3,7) respectively, where $P^{(I)}/L^2$ is small parameter and $F(\mathbf{r}_1, \mathbf{r}_2)$ is a function with an amplitude on the order of one. The second contribution in Eq. 14 originates from the reduction of the integration area (i.e. exclusion volume) $\Omega \longrightarrow \Omega - \Omega_c$ in Eq. 6. This negative contribution is proportional to the area of the cylinder Ω_c and can be estimated as $\Delta C_2^{EV}(\mathbf{r}_1, \mathbf{r}_2) \propto (1/k_0\ell) \times (\pi R_1^2/L^2)$. Therefore, although two terms in Eq. 14 have difference origin, they have comparable amplitudes. Analytical computation of $\Delta C_2^{(I)}(\mathbf{r}_1, \mathbf{r}_2)$ leads to a cumbersome expression, so we defer further analysis of this case to the numerical section below.

Surrounding a cylindrical object with a cloak modifies its "polarizability" $P^{(I)} \longrightarrow P^{(II)} = 0$ when the condition in Eq. 11 is met. As the result, the first term in Eq. 14 that proportional to $P^{(II)}$ vanishes, whereas the exclusion volume in the second term is increased to also include the cloak. Assuming that the integrand in Eq. 13 varies slowly around $\mathbf{r}_c$, we obtain the following analytical result for observation points at the output surface of the slab

$$\begin{aligned} \Delta C_2^{(II)}(y_1, L; y_2, L) = -\frac{1}{k_0 \ell} \frac{\pi R_2^2}{L^2} \frac{\pi^2 (L - z_c)^2}{4\pi L^2} \times \\ \mathrm{Re}\left[\cosh^{-2} \frac{\pi\,(i y_1 + z_c)}{2L} \cosh^{-2} \frac{\pi\,(i y_2 - z_c)}{2L} \right], \end{aligned} \tag{15}$$

When $y_1 = y_2$, $\Delta C_2^{(II)}(y, L; y, L)$ represents a correction to the fluctuations of intensity at the output surface. We find that the transverse coordinate of the cloaked object corresponds to the maximum correction ($y = y_c \equiv 0$ in our case). The depth and the size of the object can be determined from the absolute value, $|\Delta C_1^{(II)}(0, L; 0, L)| \equiv \delta$, and the full width at half maximum, Δy_{FWHM}, of the correction: $z = z_c/L = 2/\pi \cos^{-1}[(\sqrt{2} - 1)^{1/2} \sinh(\pi y_{FWHM}/L)]$

and $\pi R_2^2/L^2 = \delta 4k_0\ell L^2/(L-z_c)^2\cos^4(\pi z_c/2L)$. Table 1 summarizes the results of our calculations. It shows that the cloak removes the correction in the transmitted intensity profile but not in the long-range correlations. Moreover, the magnitude and the scaling of the correction is the same with and without the cloak. To confirm the analytical results derived above, we obtained the intensity, $\langle I(\mathbf{r})\rangle$, and the long-range intensity correlation, $C_2(\mathbf{r_1},\mathbf{r_2})$, numerically. First, we used Comsol Mutiphysics [25] to compute intensity, $\langle I(\mathbf{r})\rangle$, and the Green function, $G(\mathbf{r},\mathbf{r}')$, as solutions of the homogeneous diffusion equation and the diffusion equation with a point source, respectively. Secondly, we used Eq. 6 to calculate the correlation.

Table 1. Summary of the analytical results. Long-range intensity correlation contains the size and location (see Eq. 15) information of the cloaked object.

	Slab		Cylinder (I)	Cloak (II)
$\langle I^{(0)}\rangle$	$\propto \dfrac{\ell}{L}$	$\langle \Delta I\rangle$	$\propto \dfrac{\ell}{L}\times\dfrac{\pi R_1^2}{L^2}$	0
$C_2^{(0)}$	$\propto \dfrac{1}{k_0\ell}$	ΔC_2	$\propto \dfrac{1}{k_0\ell}\times\dfrac{\pi R_1^2}{L^2}$	$\propto -\dfrac{1}{k_0\ell}\times\dfrac{\pi R_2^2}{L^2}$

5. NUMERICAL RESULTS

Figures 2(a-c) show numerically computed intensity $\langle I(\mathbf{r})\rangle$ and the corresponding transverse profiles at the output surface $\langle I(y,L)\rangle$, Figure 2(d), for plane wave illumination for: (case 0) slab geometry (red lines); (case I) slab geometry with an embedded reflecting cylinder (black) lines; and (case II) slab geometry with an embedded cloaked cylinder (blue lines). In the latter two cases, the inclusions were placed in the middle of the slab. For results in Figure 2(a-c,e-g) the thickness was $L/\ell = 20.4$. The radii of the cylinder and cloak were chosen as $R_1/\ell = 4.5$ and $R_2/\ell = 6.8$, such that their ratio is $R_2/R_1 = 1.5$. The diffusion coefficient of the cloak satisfied Eq. 11.

As predicted analytically by Eq. 10, there exists a diffusive shadow behind the cylinder, c.f. Figs. 2(b,d), where intensity drops. In contrast, the cloaked cylinder has no shadow, concealing the presence of the cylinder in accordance with Eq. 12. To verify the theoretical scaling in Eq. 10, solid black line, we normalized the numerical intensity profiles Figure 2(d) by $\pi R_1^2/L^2$. Dashed, dot-dashed, dotted black lines are normalized intensities at output surface in the slabs with an embedded cylinder with $L/\ell = 20,\ 34$ and 41 respectively. The numerical results approach the analytical solution with an increase of L, where the dipole approximation used in deriving Eq. 10 are asymptotically satisfied.

In general, the long-range correlation $C_2(\mathbf{r}_1, \mathbf{r}_2)$ depends on two spatial coordinates $\mathbf{r}_1$ and $\mathbf{r}_2$. Figures 2(e-g) depict the diagonal part $C_2(\mathbf{r}, \mathbf{r})$ computed numerically using Eq. 6. This quantity corresponds to the non-Rayleigh contribution to intensity fluctuation. In the slab geometry, Figure 2(e), $C_2(\mathbf{r}, \mathbf{r})$ depends only on z-coordinate as $C_2(z; z) \propto (z/L)(1 - 2z/3L)$ [26]. In case of slab with a reflecting cylinder in the middle, Figure 2(f), the long-range correlation is enhanced. This is because photon path lengths increase in order to circumvent the cylinder and, thus, the probability of path crossings, responsible for correlations, is also increased. The amplitude of the correction $\Delta C_2(L, y; L, y)$ computed for slabs of different thickness, black lines in Figure 2(h) scales with $\propto \pi R_1^2/L^2$, as predicted in Table 1.

The diminished diffusion coefficient of the cylinder, Eq. 11, reduces the time the waves spend in the cloak. As a result, the intensity correlation is suppressed below the reference level of a pure slab, see Figure 2(g). This agrees both qualitatively and quantitatively with the prediction of Eq. 12. Indeed, as shown in Figure 2(h), our analytical result describes $\Delta C_2(L, y; L, y)$ computed for slabs of different thickness. Both profile and size scaling of the correction term are in agreement. In the realistic systems, an absorption tends to suppress the transmission and its fluctuations. However, the correlation in Eq. 6 is normalized by the average intensity. This largely compensates for the exponential attenuation factor associated with absorption. Hence, the long-range correlations persist at distances

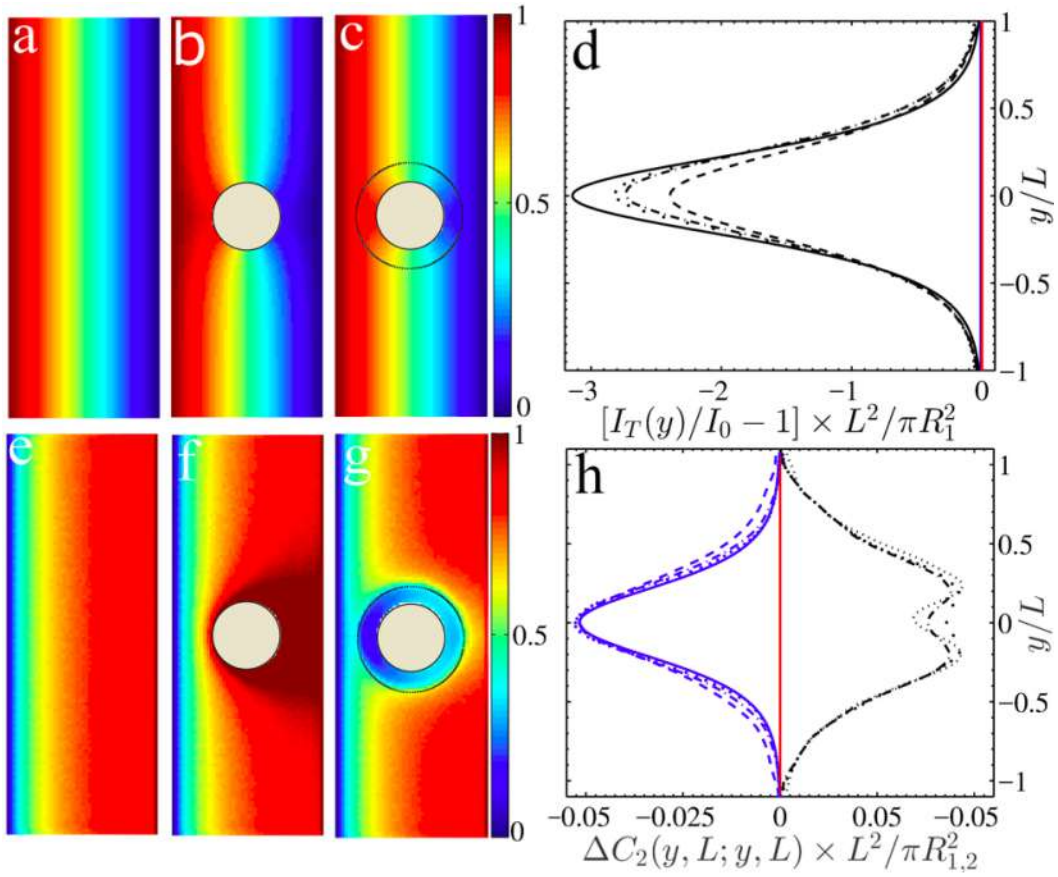

Figure 2. Panels (a-c) show intensity computed by solving diffusion equation numerically for slab, bare reflecting cylinder and cloaked cylinder respectively. (d) shows the intensity profile on the output surface of the slab. Red, black and blue curves correspond to three geometries shown in (a-c) respectively. Dashed, dot-dashed and dotted black curves correspond to slabs with $L/\ell = 20,\ 34,\ 41$; solid line is the analytical result in Eq. 10. Panels (e-g) show the amplitude of the long-range intensity correlation $C_2(\mathbf{r}, \mathbf{r})$ computed numerically from Eq. 6 and normalized to the maximum value in the case of pure slab. (h) shows $\Delta C_2(L, y; L, y)$ using the same color scheme as in (d); solid blue line is the analytical result from Eq. 15.

longer than the characteristic absorption length [27], and we expect that the effect predicted in our work will depend only weakly on absorption losses. The detailed account of loss goes beyond the scope of the current work.

6. CONCLUSIONS

Analogy between diffusion and electrostatics problems offers insights into the nature of diffusive cloak. It shows that the intensity perturbation due to embedded objects can be suppressed by cancellation of "multipoles". In case of cylindrical (spherical in 3D) inclusions, cancellation of the dominant dipole term leads to cloaking, Eq. 3. Such an approach is also analogous to ballistic cloaks employing metamaterials [28].

In this work we exploit a the fact that diffusion is only an approximate description of the electromagnetic wave transport in turbid media. The intrinsic wave effects are responsible for such phenomena as speckles, intensity fluctuations and correlations. In particular, the non-local nature of the long-range correlation offers an opportunity to detect the diffusive cloak. Crossings of diffusive paths and subsequent interference serve as “beacons” which give rise to intensity correlation detectable at the output surface of the medium. In Ref. [29], ultrasound focus was used to shift the wavelength of light and, thus, to temporarily create a source inside a strongly scattering sample. Such a technique can potentially offer an alternative approach to detecting the diffusive cloak. However, unlike the long-range correlation employed in our work, scanning ultrasonic focus would be a serial process. Lastly, use of an entirely different kind of a “beacon” – Cherenkov radiation produced by fast-moving charged particles – was proposed for detection of the ballistic cloak based on transformation optics [30].

Aside of detection of diffusive cloak, our work also offers an intriguing possibility to manipulate the second-order statistics (correlations/fluctuations) independently from first order statistics (average intensity). Finally, the results can be trivially generalized to 3D systems and for waves of different nature acoustic, electronic, seismic, etc.

ACKNOWLEDGMENTS

The authors thank Hui Cao and Raktim Sarma for numerous insightful discussions.

FUNDING

This work has been supported by National Science Foundation grant DMR-1205223.

REFERENCES

[1] V. M.Shalaev. Transforming light. *Science*, 322(5900):384–386, 2008.

[2] J. B. Pendry, D. Schurig, and D.R. Smith. Controlling electromagnetic fields. *Science*, 312(5781):1780–1782, 2006.

[3] U. Leonhardt. Optical conformal mapping. *Science*, 312(5781):1777–1780, 2006.

[4] R. Schittny, M. Kadic, T. Bückmann, and M. Wegener. Invisibility cloaking in a diffusive light scattering medium. *Science*, 345(6195):427–429, 2014.

[5] R. Schittny, A. Niemeyer, M. Kadic, T. Bückmann, A.Naber, and M. Wegener. Diffuse-light all-solid-state invisibility cloak. *Opt. Lett.*, 40(18):4202–4205, 2015.

[6] L. V. Wang and H. Wu. *Biomedical optics: principles and imaging*. John Wiley & Sons, 2007.

[7] G.W. Milton. *The theory of composites*, volume 6. Cambridge university press, 2002.

[8] F. Gömöry, M. Solovyov, J. Šouc, C. Navau, J. Prat-Camps, and A. Sanchez. Experimental realization of a magnetic cloak. *Science*, 335(6075):1466–1468, 2012.

[9] H. Xu, X. Shi, F. Gao, H. Sun, and B. Zhang. Ultrathin three-dimensional thermal cloak. *Phys. Rev. Lett.*, 112:054301–054305, Feb 2014.

[10] T. Han, X. Bai, D. Gao, J. T. L. Thong, B. Li, and C. Qiu. Experimental demonstration of a bilayer thermal cloak. *Phys. Rev. Lett.*, 112:054302, 2014.

[11] M. C. W. van Rossum and Th. M. Nieuwenhuizen. Multiple scattering of classical waves: microscopy, mesoscopy, and diffusion. *Rev. Mod. Phys.*, 71:313–371, 1999.

[12] E. Akkermans and G. Montambaux. *Mesoscopic Physics of Electrons and Photons*. Cambridge University Press, Cambridge, 2007.

[13] R. Berkovits and S. Feng. Correlations in coherent multiple scattering. *Physics Reports*, 238(3):135–172, 1994.

[14] B. Shapiro. Large intensity fluctuations for wave propagation in random media. *Phys. Rev. Lett.*, 57:2168–2171, 1986.

[15] M.J. Stephen and G. Cwilich. Intensity correlation functions and fluctuations in light scattered from a random medium. *Phys. Rev. Lett.*, 59:285–287, 1987.

[16] S. Feng, C. Kane, P. A. Lee, and A. D. Stone. Correlations and fluctuations of coherent wave transmission through disordered media. *Phys. Rev. Lett.*, 61:834–837, 1988.

[17] R. Pnini and B. Shapiro. Fluctuations in transmission of waves through disordered slabs. *Phys. Rev. B*, 39:6986–6994, 1989.

[18] A. Z. Genack, N. Garcia, and W. Polkosnik. Long-range intensity correlation in random media. *Phys. Rev. Lett.*, 65:2129–2132, 1990.

[19] P. N. den Outer, Ad Lagendijk, and Th. M. Nieuwenhuizen. Location of objects in multiple-scattering media. *J. Opt. Soc. Am. A*, 10(6):1209–1218, 1993.

[20] D. Lancaster and T. Nieuwenhuizen. Scattering from objects immersed in a diffusive medium. *Physica A*, 256(3-4):417 – 438, 1998.

[21] J.M. Luck and Th. M. Nieuwenhuizen. Light scattering from mesoscopic objects in diffusive media. *Eur. Phys. J. B*, 7(3):483–500, 1999.

[22] A. A. Lisyansky and D. Livdan. Intensity correlation in wave propagation through random media with internal reflection. *Physics Letters A*, 170(1):53 – 57, 1992.

[23] J. F. de Boer, M. P. van Albada, and Ad. Lagendijk. Transmission and intensity correlations in wave propagation through random media. *Phys. Rev. B*, 45:658–666, 1992.

[24] B.Z. Spivak and A.Yu. Zyuzin. Fluctuations of coherent light transmission through disordered media. *Solid State Communications*, 65(5):311 – 313, 1988.

[25] 'WWW.COMSOL.COM'.

[26] R. Sarma, A. Yamilov, P. Neupane, B. Shapiro, and H. Cao. Probing long-range intensity correlations inside disordered photonic nanostructures. *Phys. Rev. B*, 90:014203–014207, 2014.

[27] R. Pnini and B. Shapiro. Intensity correlation in absorbing random media. *Physics Letters A*, 157(4):265–269, 1991.

[28] A. Alù and N. Engheta. Achieving transparency with plasmonic and metamaterial coatings. *Phys. Rev. E*, 72:0166231–0166239, 2005.

[29] X. Xu, H. Liu, and L. V. Wang. Time-reversed ultrasonically encoded optical focusing into scattering media. *Nature Photonics*, 5:154–157, 2011.

[30] B. Zhang and B.I. Wu. Electromagnetic detection of a perfect invisibility cloak. *Phys. Rev. Lett.*, 103:243901, 2009.

II. UNCLOAKING DIFFUSIVE-LIGHT INVISIBILITY CLOAKS BY SPECKLE ANALYSIS

Andreas Niemeyer[1], Frederik Mayer[1,2], Andreas Naber[1], Milan Koirala[3], Alexey Yamilov[3], and Martin Wegener[1,2]

[1]*Institute of Applied Physics, Karlsruhe Institute of Technology (KIT), Karlsruhe 76128, Germany*

[2]*Institute of Nanotechnology, Karlsruhe Institute of Technology (KIT), Karlsruhe 76021, Germany*

[3]*Physics Department, Missouri University of Science and Technology, Rolla, Missouri 65409, USA*

ABSTRACT

Within the range of validity of the stationary diffusion equation, an ideal diffusive-light invisibility cloak can make an arbitrary macroscopic object hidden inside of the cloak indistinguishable from the surrounding for all colors, polarizations, and directions of incident visible light. However, the diffusion equation for light is an approximation which becomes exact only in the limit of small coherence length. Thus, one expects that the cloak can be revealed by illumination with coherent light. The experiments presented here show that the cloaks are robust in the limit of large coherence length but can be revealed by analysis of the speckle patterns under illumination with partially coherent light. Experiments on cylindrical core-shell cloaks and corresponding theory are in good agreement.

1. INTRODUCTION

The purpose of any cloak is to make an arbitrary object hidden inside of the cloak indistinguishable from the surrounding with respect to some observable [1]. A specific cloak works for a specific surrounding only. For example, in water or in a cloud, an optical invisibility cloak designed for vacuum or air would appear as a void and would hence be visible. Broadly speaking, cloaking can be seen as a striking example for that the corresponding tomography problem does not have a unique solution [2].

With respect to invisibility cloaking for electromagnetic waves following the Maxwell equations for continua, fundamental limitations of cloaking [3–5] and possibilities to uncloak the cloak have been discussed in detail. For example, due to relativity, a macroscopic object can be hidden only for a relatively small part of the electromagnetic spectrum. [4]. The extinction cross section of the cloak, integrated over all frequencies, is always larger than that of the object to be hidden alone [5]. The cloak can be uncloaked by Cherenkov radiation of charged particles passing through the cloak [6] or by motion of the cloak with respect to source and observer at relativistic speeds [7].

The situation is less clear in regard to invisibility cloaking in turbid media, where light propagation follows a diffusion equation [8, 9]. Ideal cloaks can be designed by using coordinate transformations [10] and approximate cloaks have been realized by simplified core-shell structures [11–13]. Homogenizing the light emission from Lambertian emitters such as OLEDs with shadowing metal contacts on top is a possible application [14]. Conceptually, diffusive cloaking of macroscopic objects can be ideal for the entire visible spectrum and for all polarizations and directions of incident light – at least for stationary or quasi-stationary [15–17] conditions. It is thus interesting to also investigate fundamental limitations of diffusive-light cloaking allowing for revealing the cloaks – which is the aim of the present work.

It is clear that the diffusion equation does not account for coherent wave effects like, e.g., speckles [8]. All previous experiments on core-shell structures have used illumination with incoherent white light [11–13]. Experiments in the opposite limit of illumination with coherent light from a continuous-wave laser (Toptica, DL100) operating at around $\lambda = 780$ nm wavelength along the positive z-direction are depicted in Figure 1 The bandwidth of this laser is less than 5 MHz, corresponding to a coherence length in air exceeding 60 m. The behavior shown in Figure 1 is similar to the one for illumination with incoherent white light [12]: The obstacle casts a pronounced diffusive shadow, which essentially disappears for the cloak sample, making it indistinguishable from the reference. For all samples, pronounced spatial intensity fluctuations, i.e., speckles are superimposed. Altogether, the cloak cannot be revealed by such an experiment.

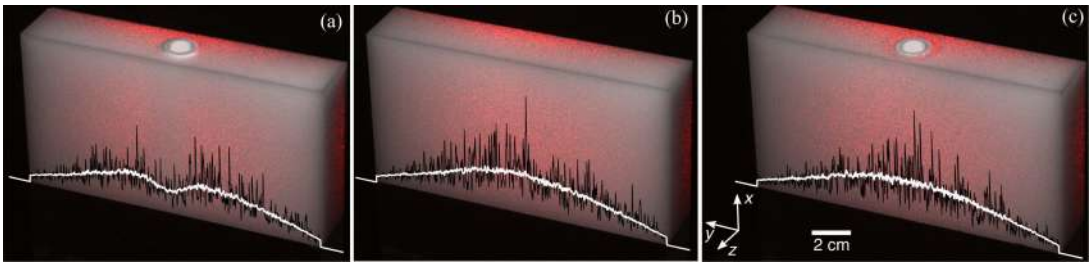

Figure 1. Images of (a) the reference, (b) the obstacle, and (c) the cloak sample under large-area illumination from the rear side(i.e. along the positive z-direction) with coherent laser light at $\lambda = 780$ nm wavelength(red). No polarizer is used in front of the camera. Each image results from two exposures: One with white-light illumination to reveal the sample and one with laser illumination. The laser light leads to strong intensity fluctuations (speckles). The two images are superimposed in the computer. The black curves are intensity cuts through the middle of the samples, projected onto the sample's surface. The white curves show the intensity averaged along the vertical direction from 25% to 75% of the sample height. We find that the obstacle casts a diffuse shadow, which essentially disappears for the cloak, making it indistinguishable from the reference. This overall behavior for illumination with coherent light is closely similar to t at for illumination with incoherent white light, which we have published previously [12]

Here, we use the same samples as in our previous work [12]: The cuboid reference sample with dimensions $L_x = 15$ cm, $L_y = 8$ cm, and $L_z = 3$ cm contains a constant density of TiO_2 nanoparticles (DuPont, R700) with an average diameter of 340 nm within a homogeneous and transparent polydimethylsiloxane (PDMS) matrix, leading to an effective

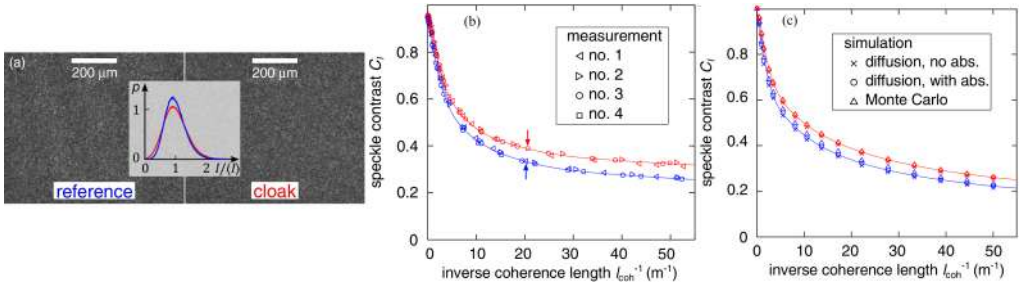

Figure 2. In contrast to Figure 1, only the center of the rear side of the sample is illuminated with a narrow beam, and a linear polarizer is placed in front of the camera. Furthermore, illumination is with partially coherent light with adjustable effective coherence length ℓ_{coh}. (a) One example ($\ell_{coh} = 4.8$ cm, see arrows in (b)) of a resolved measured speckle image for a magnified view onto the center of the front side of the reference (left) and the cloak sample (right). The inset shows the corresponding histograms, normalized to unity integral, vs. normalized intensity $I/\langle I\rangle$. (b) Derived speckle contrast,C_I, versus inverse coherence length ℓ_{coh}^{-1} for the reference (blue) and the cloak (red) sample. The solid curves are guides to the eye. (c) calculated speckle contrast versus ℓ_{coh}^{-1} represented as the experiments in (b). The different symbols corresponds to diffusion theory without absorption(crosses), diffusion theory with absorption (circles), and the Monte Carlo ray-tracing simulations(triangles).

light diffusivity of $D_O = 11.9 \times 108cm^2s^{-1}$ [12]. The corresponding transport mean free path length is $l_s^0 = 1.67$ mm. The scattering mean free path length of $l_t^0 = 0.76$ mm $= l_t^0 \times (1 - \langle\cos\theta\rangle)$ has been measured independently [12] and leads to an asymmetry value of $g = \langle\cos\theta\rangle) = 0.544$ [13]. This value indicates preferential forward scattering, which is expected for TiO_2 nanoparticles of this size. The obstacle sample additionally contains a hollow cylindrical ceramic core (Accuratus Corporation, AccuflectÂő B6) in the center of the xz-plane, with the cylinder axis parallel to the y-axis. It has an outer radius of $R_1 = 0.8cm$ and acts as a Lambertian diffusive reflector with diffusivity $D_1 \ll D_0$ The cloak sample contains an additional PDMS cylindrical shell with outer radius $R_2 = 1.2cm = 1.5 \times R_1$ around the core. The shell is doped with a 3.9 times lower concentration of TiO_2 nanoparticles than the surrounding, leading to a light diffusivity of $D_2 = 3.9 \times D_0$ [12]. Arbitrary objects can be placed into the opaque hollow ceramic core, qualifying the arrangement as a true cloak rather than just as an invisible object.

The mean distance between the intensity peaks of the speckle patterns in Figure 1 is mainly determined by the resolution capability of the imaging system. To better resolve the speckles, we perform additional experiments. We illuminate the center of the rear side of the sample (parallel to the xy-plane) with a collimated Gaussian beam (with about 2 mm diameter) of the same laser impinging along the positive z-direction. We image only a small region with about 1 mm^2 footprint in the center of the sample's front side by using a single microscope objective lens (Olympus, 605339,10 $\times$, NA = 0.25) and a charge-coupled-device (CCD) gray-scale silicon camera (Point Grey, BFLY-PGE-50H5M-C, 12 bits dynamic range). To maximize the effects and to obtain good statistics, we have chosen this region to be small compared to the cloak diameter and large compared to the speckle size. In contrast to Figure 1, a linear polarizer is located in front of the camera; without the polarizer, one would obtain an incoherent superposition of two independent speckle patterns. The speckle contrast is defined as $C_I = \sigma_I/\langle I\rangle$, with the standard deviation of the intensity pattern aI and the average intensity $\langle I\rangle$. The measured camera images contain the effects of electrical noise. We thus first subtract a dark image I^0_{ij},i.e., $I_{ij} \rightarrow I_{ij} - I^0_{ij}$. Negative values I_{ij} can result. We then compute the average $\langle I\rangle = N^{-1}\sum_{ij} I_{ij}$ and the intensity standard deviation $\sigma_1 = N^{-1}\sum_{ij}(I_{ij} - \langle I\rangle)^2$ with the number of camera pixels $N = 2448 \times 2048$. The camera exposure time is adjusted such that pixel values much larger than $\langle I\rangle$ are still below the saturation value I_{sat}, i.e., $\langle I\rangle = I_{sat}/15$. Otherwise, the speckle statistics could be distorted. The measured speckle contrast is equal to within the error bars for reference and cloak, respectively, and typically around $C_I = 95\%$ in both cases(see Figure 2(b)). This value is close to the expected theoretical ideal of $C_I = 100\%$ for fully coherent speckles from scattering off bulk turbid media or surfaces [8]. The 5% difference can be traced back to electrical noise, which smears out the contrast - despite the above background subtraction. Importantly, the cloak *cannot* be reveled in this manner.

To reveal the cloak, recent theoretical work [18] has suggested computing the long-range contribution of the second-order intensity correlation function C_2 [19] from such speckle patterns for fully coherent illumination. It relies on the existence of crossing and interference of diffusive paths. Occurrence of such processes has low probability in our highly diffusive system with $\ell_t^0 \gg \lambda$. Indeed, the published formulas applied to our sample parameters yield that the peak relative differences between reference and cloak are expected to be on the order of merely

$$|\Delta C_2^{max}| \approx \frac{1}{2}\frac{\lambda}{\ell_t^0}\frac{R_2^2}{L_z^2} \approx 4 \times 10^{-5}$$

for $\lambda = 780$ nm. Such small relative differences are very difficult to resolve for realistic statistics and single-to-noise ratios. Thus, in practice, the cloaks discussed here cannot be revealed in this manner either. The diffusive-light cloak works well for incoherent illumination as well as for coherent illumination. Can it be revealed for the intermediate case of partially coherent illumination?

It is known from our time-resolved measurements [13–15] that the propagation-time distributions are different for reference and cloak. The propagation-time, t, distribution can be converted into a path-length distribution $P(s)$, with $s = ct$ and the medium velocity of light c. The distribution $P(s)$ could alternatively be measured by an interferometric approach [20]. The physical reason for the different path-length distributions $P(s)$ is that the cloaking shell has a larger diffusivity of light than the surrounding to compensate for the near-zero diffusivity of the core. The diffusion time is inversely proportional to the diffusivity and determines the width of the path-length distribution, which is thus larger for the reference than for the cloak. This trend is partly compensated for by the facts that light has to make a detour surrounding medium for the cloak sample.

References [21–23] describe an experimental approach based on measuring speckle contrast for illumination with partially coherent light to obtain certain information about $P(s)$ without actually determining the entire path-length distribution *via* demanding time-

resolved or interferometric measurements. This approach has previously been employed for studying the internal microscopic structure of a scattering medium [24], detection of buried objects [22], and imaging in biomedical optics [25]. It is however, not a *priori* clear whether such measurement can recover enough information to reveal the existence of a cloaked object.

To test this idea, we have performed experiments in which we sweep the center frequency of the laser (monitered by a Fabry-Perot interferometer (Topitca, FPI 780)) in a periodic triangular temporal pattern, leading to a box-shaped spectrum of frequency width Δf. The camera exposure time of 250 ms is chosen to be large compared to the sweep period of 4 ms, such that this spectral width Δf effectively corresponds to a coherence length in air given by $\ell_{coh} = c_0/\Delta f$, with the vacuum speed of light c_0. Figure 2 exhibits the measured speckle contrast of the reference (blue curve) and the cloak (red curve) samples versus the inverse coherence length; Figure 2(a) depicts examples of underlying raw data. To test the reproducibility, we have repeated the experiments on different days and have intentionally taken the samples in and out of the setup in between (see measurements no. 1-4 in Figure 2(b)). We find the cloak behaves significantly and different from the reference for intermediate coherence lengths. If no separate reference sample should be available, the observer could equivalently compare the speckle contrast of images centered at the cloak position and horizontally separated from the center by a few times the diameter or the depth of the cloak (whatever is larger). This finding means that the cloak can indeed be uncloaked using partially coherent illumination -while the cloak works well for very small coherence lengths (white-light illuminations, see [12]) as well as for every large coherence lengths.

To test the validity of our interpretation, we have performed corresponding theoretical calculations. Mathematically, the speckle contrast can be obtained [21] from

$$C_I = \frac{[\int_0^\infty \int_0^\infty \mathcal{S}(\lambda)\mathcal{S}(\lambda')F(\lambda,\lambda')d\lambda d\lambda']^{1/2}}{\int_0^\infty \mathcal{S}(\lambda)d\lambda}. \tag{1}$$

The contrast depends on the spectral profile $(S)(\lambda)$ and the distribution of the path lengths $P(s)$ via function

$$F(\lambda, \lambda') = |[\int_0^\infty P(s) exp[2\pi i s(\lambda^{-1} - \lambda'^{-1})ds]|^2, \quad (2)$$

which is essentially a Fourier transform of $P(s)$. (In our case, the spectral profile is a rectangular function with a width defined by ℓ_{coh}. It can be shown that ℓ_{coh}. It can be shown that $\ell_{coh} \rightarrow \infty \rightarrow C_I \rightarrow 1$ and $\ell_{coh} \rightarrow 0 \rightarrow C_I \propto \sqrt{\ell_{coh}/\Delta s}$, with the width of the path-length distribution Δs. While Δsc is different for reference and cloak, $C_I \rightarrow 0$ holds true for both, i.e., the cloak cannot be revealed using incoherent light. For partially coherent light, the only remaining input is the path-length distribution $P(s)$ that we compute using two different numerical methods: (i) solution of the diffusion equation [13] or (ii) Monte-Carlo simulations [13]. In the case of the reference sample, both methods agree well, whereas we observe slight differences in $P(s)$ for the case of the cloak sample. This finding is due to the fact that the thickness of the cloak is not much larger than the transport mean free path and, therefore, the Monte-Carlo approach should provide a more accurate description of light propagation.

The results of numerical evaluation of Eqs. 1 and 2, shown in Figure 2(c), reproduce the measurements shown in Figure 2(b) well. In particular, we observe an onset of modification of the speckle contrast when ℓ_{coh}/c_0 becomes comparable to the time of diffusive light propagation through the sample [26] $\tau_{diff} = L_z^2/6D_0 \approx 1.3ns$, which translates onto $\ell_{coh}^{-1} \approx 2.7m^{-1}$. For larger values of ℓ_{coh}^{-1}, the differences in speckle contrast C_1 between reference and cloak samples is evident from Figure 2(b) and 2(c). This means that the cloak can indeed be revealed without having to measure the complete distributions of the path lengths $P(s)$.

Finally, our experiments and the corresponding theory have considered the case of simplified core-shell cloaks. We have used a cylindrical geometry throughout this paper because the effects are more pronounced than for spherical geometry [11]. One might ask

whether the conclusions drawn also apply for refined cloaks designed by spatial coordinate transformations [15], which can be approximated by cloaks composed of many layers [13]. The answer is yes, because the described uncloaking mechanism using partially coherent light builds upon the fact that the geometrical path-length distribution $P(s)$ or, equivalently, the propagation- time distribution, is significantly different for the reference and the cloak, respectively [15].

2. CONCLUSIONS

In conclusion, we have shown that diffusive-light invisibility cloaks can work well under stationary conditions in the limits of very small and very large coherence length of light, but can be uncloaked for the intermediate case of illumination with partially coherent light and inspection of the resulting speckle contrast. Broadly speaking, all types of cloaks have their Achilles' heels and partial coherence is one for diffusive-light cloaking. The same weakness is, of course, expected for other diffusing-wave cloaks, e.g., in acoustics.

ACKNOWLEDGEMENTS

We thank Sylvain Gigan (University Pierre et Marie Curie, France) and Aristide Dogariu (CREOL, USA) for insightful discussions. We thank the group of Heinz Kalt (KIT) for lending the laser to us and Toptica for lending the interferometer to us. We acknowledge support by the Deutsche Forschungsgemeinschaft (DFG) via the priority program DFG-SPP 1839 "Tailored Disorder", by the Helmholtz Program "Science and Technology of Nanosystems", by the Karlsruhe School of Optics and Photonics (KSOP), and by the National Science Foundation (NSF) via grant DMR-1205223.

REFERENCES

[1] M. Kadic, T. Bückmann, R. Schittny, and M. Wegener. Metamaterials beyond electromagnetism. *Reports on Progress in physics*, 76(12):126501–126533, 2013.

[2] A. Greenleaf, M. Lassas, and G. Uhlmann. On nonuniqueness for calderónś inverse problem. *Mathematical Research Letters*, 10(5):685–693, 2003.

[3] and B. Zhang H. Hashemi, J. D. Joannopoulos, and S. G. Johnson. Delay-bandwidth and delay-loss limitations for cloaking of large objects. *Phys. Rev. Lett.*, 104:253903, Jun 2010.

[4] F. Monticone and A. Alù. Do cloaked objects really scatter less? *Phys. Rev. X*, 3:041005, 2013.

[5] F. Monticone and A. Alù. Invisibility exposed: physical bounds on passive cloaking. *Optica*, 3(7):718–724, 2016.

[6] B. Zhang and B.I. Wu. Electromagnetic detection of a perfect invisibility cloak. *Phys. Rev. Lett.*, 103:243901, 2009.

[7] J.C. Halimeh, R.T. Thompson, and M. Wegener. Invisibility cloaks in relativistic motion. *Phys. Rev. A*, 93:013850, 2016.

[8] J. W. Goodman. *Speckle phenomena in optics: theory and applications*. s and Company Publishers, 2007.

[9] F. Martelli, S.D. Bianco, A. Ismaelli, and G. Zaccanti. *Light propagation through biological tissue*, volume 10. SPIE press, 2010.

[10] S. Guenneau, C. Amra, and D. Veynante. Transformation thermodynamics: cloaking and concentrating heat flux. *Opt. Express*, 20(7):8207–8218, 2012.

[11] R. Schittny, M. Kadic, T. Bückmann, and M. Wegener. Invisibility cloaking in a diffusive light scattering medium. *Science*, 345(6195):427–429, 2014.

[12] R. Schittny, A. Niemeyer, M. Kadic, T. Bückmann, A.Naber, and M. Wegener. Diffuse-light all-solid-state invisibility cloak. *Opt. Lett.*, 40(18):4202–4205, 2015.

[13] R. Schittny, A. Niemeyer, F. Mayer, A. Naber, M. Kadic, and M. Wegener. Invisibility cloaking in light-scattering media. *Laser & Photonics Reviews*, 10(3):382–408, 2016.

[14] F. Mayer, R. Schittny, A. Egel, A. Niemeyer, J. Preinfalk, U. Lemmer, and M. Wegener. Cloaking contacts on large-area organic light-emitting diodes. *Advanced Optical Materials*, 4(5):740–745, 2016.

[15] R. Schittny, A. Niemeyer, M.Kadic, T. Bückmann, A. Naber, and M. Wegener. Transient behavior of invisibility cloaks for diffusive light propagation. *Optica*, 2(2):84–87, 2015.

[16] B. Orazbayev, M. Beruete, A. Martínez, and C. García-Meca. Diffusive-light invisibility cloak for transient illumination. *Phys. Rev. A*, 94:063850, 2016.

[17] M. Farhat, P. Y. Chen, S. Guenneau, H. Bağcı, K.N. Salama, and A. Alù. Cloaking through cancellation of diffusive wave scattering. *Proc. R. Soc. A*, 472(2192):20160276, 2016.

[18] M. Koirala and A. Yamilov. Detection of a diffusive cloak via second-order statistics. *Opt. Lett.*, 41(16):3860–3863, 2016.

[19] M. C. W. van Rossum and Th. M. Nieuwenhuizen. Multiple scattering of classical waves: microscopy, mesoscopy, and diffusion. *Rev. Mod. Phys.*, 71:313–371, 1999.

[20] G. Popescu and A. Dogariu. Optical path-length spectroscopy of wave propagation in random media. *Opt. Lett.*, 24(7):442–444, 1999.

[21] C. A. Thompson, K. J. Webb, and A. M. Weiner. Diffusive media characterization with laser speckle. *Appl. Opt.*, 36(16):3726–3734, 1997.

[22] J. D. McKinney, M. A. Webster, K. J. Webb, and A. M. Weiner. Characterization and imaging in optically scattering media by use of laser speckle and a variable-coherence source. *Opt. Lett.*, 25(1):4–6, 2000.

[23] N. Curry, P. Bondareff, M. Leclercq, N. F. van Hulst, R. Sapienza, S. Gigan, and S. Grésillon. Direct determination of diffusion properties of random media from speckle contrast. *Opt. Lett.*, 36(17):3332–3334, 2011.

[24] A. Dogariu and R. Carminati. Electromagnetic field correlations in three-dimensional speckles. *Physics Reports*, 559:1–29, 2015.

[25] D. A. Boas and A.K. Dunn. Laser speckle contrast imaging in biomedical optics. *Journal of biomedical optics*, 15(1):011109, 2010.

[26] R. B. Bird, W. E. Stewart, and E. N. Lightfoot. Transport phenomena. *AIChE Journal*, 7(2):5J–6J, 1960.

III. INVERSE DESIGN OF PERFECTLY TRANSMITTING EIGENCHANNELS IN SCATTERING MEDIA

Milan Koirala[1] , Raktim Sarma[2], Hui Cao[2], and Alexey Yamilov[1]

[1]*Department of Physics, Missouri University of Science and Technology, Rolla, MO* 65409*, USA*

[2]*Department of Applied Physics, Yale University, New Haven, Connecticut 06520, USA*

ABSTRACT

Light-matter interactions inside turbid medium can be controlled by tailoring the spatial distribution of energy density throughout the system. Wavefront shaping allows selective coupling of incident light to different transmission eigenchannels, producing dramatically different spatial intensity profiles. In contrast to the density of transmission eigenvalues that is dictated by the universal bimodal distribution, the spatial structures of the eigenchannels are not universal and depend on the confinement geometry of the system. Here, we develop and verify a model for the transmission eigenchannel with the corresponding eigenvalue close to unity. By projecting the original problem of two-dimensional diffusion in a homogeneous scattering medium onto a one-dimensional inhomogeneous diffusion, we obtain an analytical expression relating the intensity profile to the shape of the confining waveguide. Inverting this relationship enables the inverse design of the waveguide shape to achieve the desired energy distribution for the perfectly transmitting eigenchannel. Our approach also allows to predict the intensity profile of such channel in a disordered slab with open boundaries, pointing to the possibility of controllable delivery of light to different depths with local illumination.

1. INTRODUCTION

Interference of scattered waves in random media gives rise to well-known phenomena such as enhanced backscattering, Anderson localization and universal conductance fluctuation. These phenomena are general and occur not only for electromagnetic waves, but also for acoustic, electronic and other kinds of waves [1, 2]. Recently, there has been a growing interest in another interference effect – formation of perfectly transmitting channels [3, 4], which can greatly enhance the total transmission through opaque media [5–8]. In addition, the perfectly transmitting channels have energy density buildup deep inside the medium [7, 9–11], opening the possibility of enhancing linear and non-linear light-matter interactions inside turbid media. Recent advances of optical wavefront shaping techniques [12–17] enabled direct coupling of incident light to perfectly transmitting channels [11], making the depth profile of energy density dramatically different from the typical decay in a diffusive medium. To unlock the full potential of this approach for tailoring light-matter interactions in turbid media, it becomes imperative to understand what determines the spatial structure of the perfectly transmitting channels.

Recently two theoretical models have been put forward to describe the spatial profile of the perfectly transmitting channels in lossless diffusive media. Davy et al [9] applied the supersymmetry theory to wave propagation in a quasi-one-dimensional random system and related the intensity profile to the return probability (RP) of diffusive waves. Ojambati and co-workers[10, 18] proposed that the perfectly transmitting channel in a disordered slab is related to the fundamental mode (FM) of the one-dimensional (1D) diffusion equation. Although both models predict correctly the depth of the maximum energy density [7, 9, 11, 19], they disagree quantitatively in terms of the depth profile for the perfectly transmitting channel. So far, both models have been applied only to one-dimensional diffusion.

We have studied light transport in quasi-two-dimensional disordered systems, and showed that the spatial structure of transmission eigenchannels can be modified by the confinement geometry [20]. For example, by adjusting the shape of the reflecting boundary

of a disordered waveguide, the depth at which the energy density of a high transmission channel reaches the maximum can be moved. This enables enhancing light-matter interaction at different location inside the random medium. For many applications, inverse design is needed, namely, to design the confinement geometry to achieve the desired depth profile of energy density inside a diffusive system. This requires a prior knowledge of the relation between the geometry of the system and the spatial structure of the transmission channels. However, there is currently no theoretical model capable of establishing such relation.

In this work, we consider a two-dimensional disordered waveguide with an *arbitrary* shape, and develop a theoretical model to predict the spatial structure of the perfectly transmitting eigenchannel in the regime of diffusive transport. We further employ a projection technique, developed in physical chemistry for the particle diffusion in confined geometries [21], to obtain an analytical relation between the depth profile of the perfectly transmitting eigenchannel and the geometry of the waveguide. With this relation, we perform the inverse design of the waveguide shape to realize the desired energy distribution for the perfectly transmitting eigenchannel. Finally, we predict the depth profile for the perfectly transmitting eigenchannel in an open slab geometry with local illumination, by simulating the lateral beam spread in a waveguide of expanding width. We find that the depth of the maximum of intensity increases with the size of the impinging beam, which provides an insight into controlling the energy distribution inside a diffusive slab with local illumination.

2. MODEL AND ITS SOLUTION

The transmission matrix, which connects the transmitted fields to the incident fields, contains the complete information about wave transport through the disordered system. Transmission eigenchannels are introduced via singular value decomposition of the transmission matrix $\hat{t} = \hat{U}\hat{\tau}^{1/2}\hat{V}^{\dagger}$. Here $\hat{\tau}$ is the diagonal matrix of eigenvalues of $\hat{t}^{\dagger}\hat{t}$ that represent the transmittance of each eigenchannel; $\hat{V}$ is a unitary matrix that maps the in-

coming modes onto the eigenchannels; and $\hat{U}$ is a unitary matrix that maps the eigenchannels onto the outgoing modes. In the regime of diffusive transport, the transmission eigenvalues have a universal bimodal distribution, independent of both the microscopical details of the disorder and the boundary shape of the system. It consists of two peaks at $\tau \sim 0$ and $\tau \sim 1$, which correspond respectively to closed and open eigenchannels [22–25].

Here, we consider a two-dimensional (2D) waveguide with reflecting boundaries at $y = \pm W(z)/2$. The region $0 \leq z \leq L$ is filled with lossless scattering medium characterized by the transport mean free path $\ell \ll L$. The waveguide width $W(z)$ can be either larger or smaller than the length L, corresponding to slab or quasi-1D geometry. Our aim is to predict the depth profile (cross-section averaged intensity) of the perfectly transmitting eigenchannel (PTE) with $\tau \simeq 1$, $\phi(z) \equiv W^{-1}(z) \int_{-W(z)/2}^{W(z)/2} \langle I_{PTE}(\mathbf{r}) \rangle dy$, where $I_{PTE}(\mathbf{r})$ is the intensity and $\langle ... \rangle$ denotes the ensemble averaging. $I_{PTE}(\mathbf{r}) \equiv |E_{PTE}(\mathbf{r})|^2$, and $E_{PTE}(\mathbf{r})$ is the solution of the wave equation with the incident wave given by the eigenvector (a column vector in $\hat{V}$) corresponding to the eigenvalue $\tau \simeq 1$.

Diagrammatic theory was used [9] to establish connection between the spatial profile of PTE and the diffusion return probability to the cross-section in a rectangular waveguide of constant width $W \ll L$. To determine PTE profile in the waveguides of an arbitrary cross-section and without the width constraint, we propose a phenomenological model based on the solution of the diffusion equation with the additional *ad-hoc* self-action term on the right-hand-side:

$$-\nabla_{\mathbf{r}}^2 G(\mathbf{r}; \mathbf{r}') = [1 + \alpha G(\mathbf{r}; \mathbf{r}')] \, \delta(z - z')/W(z), \tag{1}$$

where the diffusion coefficient D_0 is absorbed in the definition of $G(\mathbf{r}; \mathbf{r}')$. Cross-section average of its solution $\tilde{G}(z; z') \equiv W^{-2}(z) \int \int G(y, z; y', z') dy dy'$ gives the normalized depth profile of PTE $\phi(z) = \tilde{G}(z; z)/\max[\tilde{G}(z; z)]$. For a rectangular waveguide in the limit of $W \ll L$ with $\alpha \equiv 0$, Eq. (1) reduces to the return probability model of Ref. [9].

The *ad-hoc* self-action term in Eq. (1) will be justified in numerical simulations below, it is meant to account for the effect of interference of waves that return after multiple scattering. It reflects the fact that upon the return, the coherent sum of the fields leads to the cross terms in the total intensity, similar to the weak localization correction [26]. With the proper choice of α (to be determined below), this equation can be solved inside the disordered waveguide ($0 \le z \le L$, $|y| \le W(z)/2$) with the open boundary conditions at the two ends ($z = 0, L$), $[z_0 \partial G(\mathbf{r};\mathbf{r}')/\partial z \mp G(\mathbf{r};\mathbf{r}')]_{z=0,L} = 0$, where $z_0 = (\pi/4)\ell$ is the 2D extrapolation length [1]. The solution can be readily obtained numerically.

To obtain the analytical solution, we employ a projection technique that was developed in the study of diffusion of electrolytes in nano-pores [21]. This technique reduces the process of solving $2D$ diffusion equation in a complex geometry to a solution of the one-dimensional diffusion equation (along z-axis) with an effective diffusion coefficient that varies with z:

$$\mathcal{D}(z) = W(z)/\left[1 + (W'(z)/2)^2\right]^{1/3}, \tag{2}$$

where the nominator accounts for the geometrical effect of reduction of flux in a constriction, and the denominator is introduced to expand the applicability to systems with larger width variation of upto $W'(z) \simeq 1$, see Ref. [21] for details. Eq. (1) is then transformed to yield $\tilde{G}(z;z')$ directly

$$-\frac{\partial}{\partial z}\mathcal{D}(z)\frac{\partial}{\partial z}\tilde{G}(z;z') = \left[1 + \alpha\tilde{G}(z,z')\right]\delta(z - z'), \tag{3}$$

while the boundary conditions at $z = 0, L$ remain the same. This method suits our problem because we are interested in the depth dependence of the cross-section-averaged intensity profile.

We stress that the z-dependent diffusivity $\mathcal{D}(z)$ arises from the varying width $W(z)$ in a purely diffusive waveguide where the localization corrections are negligible. In the regime where localization corrections are significant, the projection ansatz used to obtain Eq. (3)

from Eq. (1) is still applicable with the effective diffusion coefficient $\mathcal{D}(z)\times D(z)/D_0$, where $D(z)$ is the cross-section averaged value of the position-dependent diffusion coefficient [27–29] due to the localization-induced renormalization and D_0 is its unrenormalized value.

Solution of Eq. (3) can be obtained in the closed form

$$\phi(z) = \frac{(1-\tilde{\alpha})F(z)}{[1-\tilde{\alpha}F(z)]} \tag{4}$$

$$F(z) = \frac{4\left(\frac{z_0}{\mathcal{D}(0)} + \int_0^z \frac{dz'}{\mathcal{D}(z')}\right)\left(\frac{z_0}{\mathcal{D}(L)} + \int_z^L \frac{dz'}{\mathcal{D}(z')}\right)}{\left(\frac{z_0}{\mathcal{D}(0)} + \frac{z_0}{\mathcal{D}(L)} + \int_0^L \frac{dz'}{\mathcal{D}(z')}\right)^2}$$

$$\tilde{\alpha} = \frac{\alpha}{4}\left(\frac{z_0}{\mathcal{D}(0)} + \frac{z_0}{\mathcal{D}(L)} + \int_0^L \frac{dz'}{\mathcal{D}(z')}\right). \tag{5}$$

$\phi(z)$ has been normalized so that $\max[\phi(z)] = 1$ and $F(z)$ is an auxiliary function, which corresponds to the normalized solution of the same set of equations with $\alpha = 0$. The value of α (or $\tilde{\alpha}$) can be found from the waveguide with constant width.

3. VERIFICATION IN RECTANGULAR GEOMETRY

To test the analytical solution, we compare it to the numerical solution obtained by directly solving the wave equation with KWANT simulation package [30], see Appendix A for details. Figure 3a compares the profile of PTE computed numerically to the predictions of the two previously developed models [9, 18]. Although RP-model deviates from the numerical solution, both models agree well at $z = 0, L$. They give $\phi^{(RP)}(0) = (8/\pi)\times(\ell/L) \simeq 2.55 \times (\ell/L)$ and $\phi^{(FM)}(0) = (\pi^2/4) \times (\ell/L) \simeq 2.47 \times (\ell/L)$. The knowledge of $\phi(z)$ at one point is enough to recover the value of the coefficient $\tilde{\alpha}$. We find close values of $\tilde{\alpha} = 1 - 8/\pi^2 \simeq 0.19$ and $\tilde{\alpha} = 1 - \pi/4 \simeq 0.21$ from the two models. Below, to be specific, we use the former value. Importantly, we observe that $\tilde{\alpha}$ is a non-zero numerical constant independent of system parameters, such as the transport mean free path and the system dimension, underlining the universality of the self-action term on the right-hand-side of

Eqs. (1,3). The result of Eqs. (4) is shown as dashed line in Figure 3a, it agrees well with the result of numerical simulations. Quantitatively, for RP-, FM-models and our Eq. (4) are 5.6%, 0.4% and 0.4% respectively. Furthermore, in Figure 3b we verify that the same value of $\tilde{\alpha}$ applies to waveguides with varying cross-section. We stress that the agreement between numerical simulations and our model is achieved with no fitting parameters.

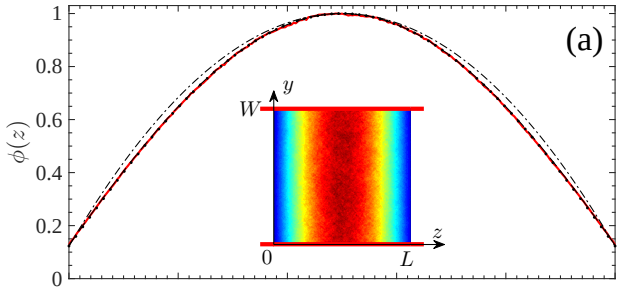

Figure 1. Comparison of previous models to ours in predicting the perfectly transmitting eigenchannels (PTEs) in the diffusive waveguides. (a) The cross-section integrated intensity $\phi(z)$ of the PTE in a constant width waveguide, computed numerically (bold solid line) and predicted by the RP-model (dash-dotted line), the FM-model (dotted line), and our model Eq. (4) (dashed line). The inset is 2D intensity distribution of the PTE, computed numerically, throughout this waveguide with $L/\ell = W/\ell \simeq 18.3$.

4. ARBITRARY GEOMETRY: INVERSE DESIGN

The closed-form analytical solution given in Eq. (4) establishes the relation between the shape of the diffusive waveguide and the depth profile of the PTE, thus enabling the inverse design. By introducing a normalized width function $w(z) = [W(z)/L] \times \int_0^L dz'/W(z')$, the dimensionless conductance $g = k\ell/\left[2\int_0^L dz'/W(z')\right]$ [31], and neglecting the extrapolation length z_0, we obtain an expression for waveguide boundary function $w_0(z)$ in terms of the depth profile $\phi_0(z)$

$$w_0(z)/\left[1+\left(\frac{g}{k\ell}w_0'(z)\right)^2\right]^{1/3} = \left[(1-\tilde{\alpha})(1-\tilde{\alpha}(1-\phi_0(z)))^3(1-\phi_0(z))/\phi_0'^2(z)\right]^{1/2}, \tag{6}$$

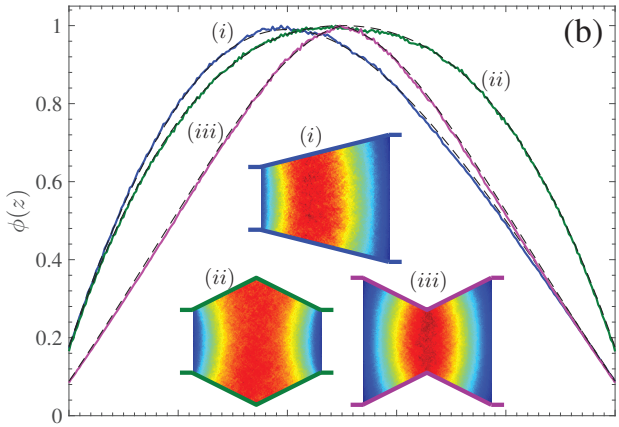

Figure 2. (b) $\phi(z)$ for the PTEs in three waveguides of varying cross-section. Blue color: expanding waveguide, green color: lantern waveguide, purple color: bow-tie waveguide. Solid lines: numerical simulation, dashed lines: our model Eq. (4). The inset are the numerically calculated 2D intensity distribution for the PTEs in the three waveguides. The waveguide length and width at the widest point are identical to those of the waveguide shown in Figure 3(a). The width at the narrowest point is equal to a half of that at the widest point.

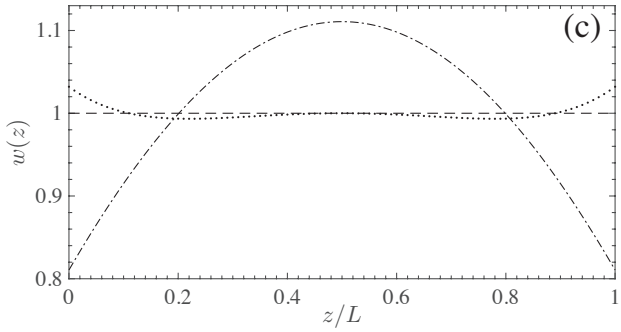

Figure 3. Figure (c) The waveguide width $w_0(z)$ obtained by inverting (via Eq. (13)) the depth profile $\phi_0(z)$ predicted in the rectangle geometry by the RP-model (dash-dotted line), the FM-model (dotted line), constant width (dashed line) is shown for reference. $z_0 \ll L$ is assumed for clarity. The FM model shows less deviation from a constant width than the RP-model, but only our model produces the consistent result of constant width.

where $k = 2\pi/\lambda$ is wave number and $\phi_0(z)$ satisfies the boundary condition $\phi_0(z = 0, L) = 0$. The extrapolation length at the boundary $z = 0, L$ can be accounted for by the following scaling

$$\phi_0(z) \quad \rightarrow \quad \phi(z) = \phi_0\left((z + z_0)/(L + 2z_0)\right) \tag{7}$$

$$w_0(z) \quad \rightarrow \quad w(z) = w_0\left((z + z_0)/(L + 2z_0)\right). \tag{8}$$

In Appendix B, we present a table of $\phi(z)$ for the waveguide geometries $w(z)$ shown in Figure 3b.

The relation between $w(z)$ and $\phi(z)$ allows us to infer the shape of the waveguide from the depth profile of the PTE. For the depth profile of PTE predicted by the RP- and FM-models for the rectangle waveguide, c.f. Figure 1c, we derive the corresponding waveguide shape, as shown in Figs. 3c. The shape predicted by the RP model corresponds to a waveguide with the width variation of up to 20%. In contrast, FM-model is more accurate. However, in other waveguide geometries, the PTE profiles predicted by the FM-model are inconsistent with the results of the numerical simulations.

To demonstrate the power of inverse design, we change the universal profile of PTE in constant-width waveguides to a highly unusual profile of a triangle. According to Eq. (13), to have $\phi_0(z)$ increase linearly with z, we find the waveguide width $w(z) \propto \sqrt{z}$ in the leading order of $\tilde{\alpha}$. This allows us to design waveguides that support PTE with a triangular profile, as shown in Figure 4. The waveguide boundary is described by $W(z) = W_c + \Delta W\sqrt{|z - z_c|/z_c}$, where z_c denotes the depth at which the width is the narrowest. It also closely corresponds to the maximum of the intensity profile of the PTE. The results in Figure 4, obtained for two different values of $z_c/L = 1/2$ and $2/3$, show that it is possible to obtain waveguide geometries that have maximum concentration of energy at the desired depth.

Finally, the inverse design introduced above provides an insight to controlling the depth profile of light intensity inside *a disordered slab* with local illumination. Such a geometry is common in optical experiments, and it is different from the waveguide geometry because the light will diffuse laterally as it penetrates deeper into the slab. A waveguide expanding linearly at 45° angle can be used as a proxy for studying the lateral diffusion in the slab geometry with local illumination [31]. In particular we consider a waveguide with

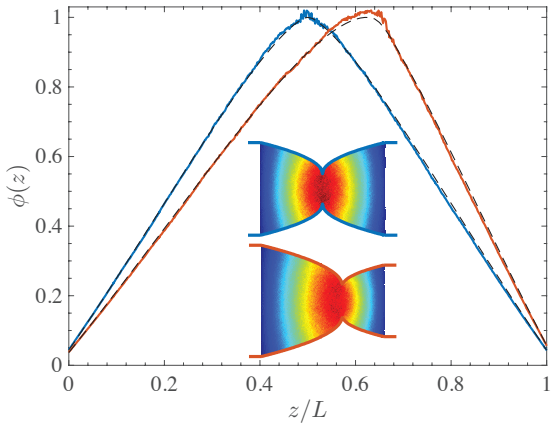

Figure 4. Design of waveguide shape to achieve the desired depth profile of PTE. The cross-section averaged intensity $\phi(z)$ showing an abnormal triangular dependence on the depth is obtained by the inverse design of the waveguide width $w(z)$ by Eq. (13). Bold solid lines are the result of numerical simulation, and dashed lines are the prediction by our model. The two waveguides, shown in the inset, have the PTE intensity maximum at the depth $z_c/L = 1/2$ (blue line) and $2/3$ (red line). The 2D intensity distribution of PTE are plotted in insets.

expanding width $W(z) = W_1 + (W_2 - W_1) \times (z/L)$, and the tapering angle of the waveguide boundary is $\theta = \arctan[(W_2 - W_1)/2L] = 45°$, to mimic the lateral diffusion in the slab. Substituting this expression into Eq. (4) leads to an important result – the profile of PTE depends on the aspect ratio of the waveguide W_1/L, see Figure 5. It implies that in the slab geometry, the ratio between the impinging beam size and the thickness of the slab can be used to control the energy penetration. An analytical expression of the depth profile is given in Appendix B, here, we only present the formula for the depth of the maximum of the intensity

$$z_{max} \simeq L/\left[1 + \sqrt{1 + 2L/W_1}\right]. \tag{9}$$

As expected, for $W_1 \gg L$ we recover known result $z_{max} \to L/2$. As W_1/L decreases, the maximum of the energy profile is displaced towards the front surface. This result has practical applications as it offers a mechanism to scan the intensity maximum of PTE in the longitudinal direction of a disordered slab by varying the incident beam size.

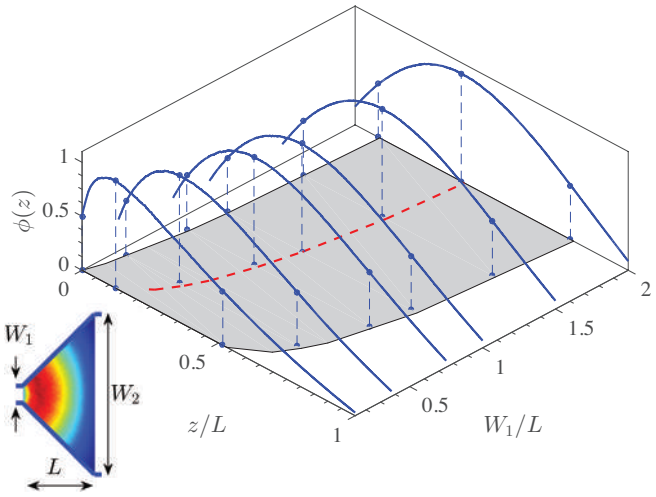

Figure 5. Prediction of PTE depth profile in an open slab with local illumination by approximating the lateral beam spreading with an expanding waveguide. The cross-section averaged intensity $\phi(z)$ for the linearly expanding waveguides $W(z) = W_1 + 2 \times z$ with different values of W_1 and fixed $L/\ell \simeq 18.3$. Gray area represents the region where $\phi(z)$ is greater than $1/2$ of its maximum value. The position of the maximum z_{max} depends on W_1/L, which is well described by Eq. (9), bold dashed line.

5. CONCLUSIONS

In conclusion, we proposed a model for the perfectly transmitting eigenchannel (PTE) in the two-dimensional (2D) random system with an arbitrary shape. A self-action term was incorporated into the 2D diffusion equation for the return probability, to account for the interference effect. We employed a projection technique to reduce the 2D problem to 1D, and obtained an analytical expression relating the depth profile of the PTE to the boundary shape of the waveguide. This relation enabled the inverse design, namely, finding the waveguide shape to achieve the desired depth profile of the PTE. As an example, we predicted and verified numerically a specific shape of the waveguide in which PTE has a triangular profile. Such a profile, distinct from the universal parabolic-like profile of the PTE in the rectangle-shaped waveguide [4, 7, 9, 18], yields a tighter energy distribution, that can enhance the local light-matter interaction inside the diffusive medium.

Approximating the lateral beam spreading with an expanding waveguide, we predict the depth profile for the PTE in an open slab with local illumination. The depth for the maximum intensity increases with the size of the impinging beam. Our model can be further extended to include the effect of mismatched boundary conditions [32](via an appropriate choice of z_0), and to describe three-dimensional geometries, see Appendix C. In the latter case, the projection to one-dimension Eq. (2) shall be modified as well [21]. The results presented here are applicable to electromagnetic, acoustic, electronic and other types of waves. In optics, in particular, controllable delivery of light to different depths may lead to non-invasive imaging, sensing and therapeutic applications such as e.g. 2-photon fluorescence, second harmonic generation microscopy.

ACKNOWLEDGMENTS

The authors acknowledge the support from the US National Science Foundation under Grant No. DMR-1205223, from the US Office of Naval Research under grant No. N00014-13-1-0649, and the US–Israel Binational Science Foundation (BSF) under grant No. 2015509.

APPENDICES

A. NUMERICAL SIMULATIONS

We numerically obtain the perfectly transmitting eigenchannel (PTE) by the direct solution of the wave equation using KWANT simulation package [11, 30]. It allows to conveniently compute the transmission matrix $\hat{t}$ relating the incoming and outgoing wave amplitudes. The simulated system is a two-dimensional disordered waveguide $0 \leq z \leq L$, $|y| \leq W(z)/2$. In KWANT it is defined as a collection of coupled lattice sites in the two-dimensional rectangular grid described by a tight-binding Hamiltonian. Lack of

bonds at the terminal sites at the sidewalls naturally introduces the reflecting boundary conditions. To model a passive random medium we introduce disorder by adding a random on-site potential δE_{ii} to the diagonal elements as $H_{ii} = E_0 + \delta E_{ii}$, while keeping the nearest neighbor couplings at constant value of 1. The scattering region $0 \leq z \leq L$ is connected to the leads at $z < 0$ and $z > L$ where $\delta E_{ii} = 0$. This model is well suited to describe wave scattering phenomena as long as $k\ell \gg 1$ [33] where k is the wave number and ℓ is transport mean free path.

The transmission matrix $\hat{t}$ relates the amplitudes of the propagating modes incident from the left lead ϕ_a to those of the outgoing modes in the right lead ϕ_b. Representing $t^\dagger t = \hat{V}\hat{\tau}\hat{V}^\dagger$ gives the diagonal matrix of eigenvalues τ_n and the corresponding eigenchannels V_{an}. After computing $\hat{t}$, we construct the input field vector $\phi_a = V_{an}$ to couple exclusively into a specific eigenchannel n. With τ_n arranged in the decreasing order, $n = 1$ corresponds to the maximum transmission eigenchannel [11]. The parameters of the waveguides are chosen to be in the regime of a well-developed diffusive propagation $L/\ell, W/\ell \gg 1$. In this regime, the universal bimodal distribution of the eigenvalues τ_n yields the maximum at $\tau \simeq 1$. In each disorder realization we select eigenchannel with $n = 1$ and retain it only if $1 - \epsilon < \tau_{n=1} < 1$ with $\epsilon = 0.03$. Then we compute its intensity $I_{PTE}(\mathbf{r})$ and average over the ensemble of 1000 random realizations of disorder to obtain $\langle I_{PTE}(\mathbf{r})\rangle$. $\phi(z)$ is obtained by averaging $\langle I_{PTE}(\mathbf{r})\rangle$ over the cross-section of the waveguide.

B. PTE PROFILES FOR SELECT GEOMETRIES

In Sec.3 we outlined the procedure to find the depth profile of PTE $\phi(z)$ for a given shape of disordered waveguide $w(z)$, Eqs. (2,4), or other way around, to find $w(z)$ from $\phi(z)$, Eq. (13). In this appendix we present the pairs $w(z)$, $\phi(z)$ for a select group of waveguide geometries studied in this work.

1. Rectangular waveguide:

$$\begin{aligned} w(z) &\equiv 1 \\ \phi(z) &= \frac{4(1-\tilde{\alpha})\zeta(1-\zeta)}{1-4\tilde{\alpha}\zeta(1-\zeta)} \\ \zeta &= (z+z_0)/(L+2z_0). \end{aligned}$$

2. Linearly expanding waveguide:

$$\begin{aligned} w(z) &= \left(\frac{W_1}{W_2-W_1}+\frac{z}{L}\right)\log\frac{W_2}{W_1} \\ \phi(z) &= \frac{4(1-\tilde{\alpha})\zeta(1-\zeta)}{1-4\tilde{\alpha}\zeta(1-\zeta)} \\ \zeta &= \frac{\dfrac{z_0}{W_1}+\dfrac{L}{W_2-W_1}\log\dfrac{w(z)}{w(0)}}{\dfrac{z_0}{W_1}+\dfrac{z_0}{W_2}+\dfrac{L}{W_2-W_1}\log\dfrac{w(L)}{w(0)}}. \end{aligned}$$

Here $W_{1,2}$ denote the widths at $z = 0, L$.

3. Bowtie/lantern waveguide:

$$\begin{aligned} w(z) &= \left(\frac{W_2}{W_1-W_2}+\left|2\frac{z}{L}-1\right|\right)\log\frac{W_1}{W_2} \\ \phi(z) &= \frac{4(1-\tilde{\alpha})\zeta(1-\zeta)}{1-4\tilde{\alpha}\zeta(1-\zeta)} \\ \zeta &= \frac{\dfrac{z_0}{W_1}+\dfrac{L/2}{W_2-W_1}\log\dfrac{w(z)}{w(0)}}{\dfrac{z_0}{W_1}+\dfrac{z_0}{W_2}+\dfrac{L}{W_2-W_1}\log\dfrac{w(L)}{w(0)}}. \end{aligned}$$

Here W_1 denote the widths at $z = 0, L$, and W_2 is the width at the mid-point $z = L/2$ of the waveguide.

C. GENERALIZATION TO 3D

In this Appendix we generalize our model Eqs. (1,2,3) to three-dimensional systems. We consider axially symmetric waveguide of diameter $W(z)$ where z is the axial coordinate. This corresponds to cross-section $A(z) = \pi W^2(z)/4$ which varies longitudinally. 3D version of Eq. (1) with a planar source at z' now reads

$$-\nabla^2_{\mathbf{r}} G(\mathbf{r};\mathbf{r}') = \left[1 + \alpha^{(3D)} G(\mathbf{r};\mathbf{r}')\right] \delta(z - z')/A(z), \tag{10}$$

where as in Eq. (1) the diffusion coefficient has been absorbed in the definition of $G(\mathbf{r};\mathbf{r}')$. Open boundary conditions are to be applied at the two ends ($z = 0, L$), $\left[z_0^{(3D)} \partial G(\mathbf{r};\mathbf{r}')/\partial z \mp G(\mathbf{r};\mathbf{r}')\right]_{z=0,L} = 0$, where $z_0^{(3D)} = (2/3)\ell$ is the 3D extrapolation length. Projection from the 3D waveguide geometry to 1D system with spatially-varying diffusion coefficient can be accomplished analogously [21] to 2D case (compare to Eq. (2)), with

$$\mathcal{D}^{(3D)}(z) = A(z)/\left[1 + (W'(z)/2)^2\right]^{1/2}, \tag{11}$$

Eq. (10) is then transformed to yield $\tilde{G}(z;z') \equiv A^{-2}(z) \int\int G(\mathbf{r};\mathbf{r}') dx dy dx' dy'$ directly

$$-\frac{\partial}{\partial z} \mathcal{D}^{(3D)}(z) \frac{\partial}{\partial z} \tilde{G}(z;z') = \left[1 + \alpha^{(3D)} \tilde{G}(z,z')\right] \delta(z - z'), \tag{12}$$

while the boundary conditions at $z = 0, L$ remain the same as for Eq. (10).

The normalized depth profile of PTE $\phi(z) = \tilde{G}(z;z)/\max[\tilde{G}(z;z)]$ can be found in the analytical form of Eqs. (4,5) with substitution of $\mathcal{D}(z) \to \mathcal{D}^{(3D)}(z)$ and $\tilde{\alpha} \to \tilde{\alpha}^{(3D)}$. The former is given by Eq. (11). The value of the constant $\tilde{\alpha}^{(3D)}$ can be established using the same procedure as in Sec. 2 – comparing the result to the waveguide with $W(z) = const \ll L$ in RP- or FM-model. We find $\tilde{\alpha}^{(3D)} = 1 - 3/\pi \simeq 0.045$ and $1 - 3\pi^2/32 \simeq 0.075$ respectively.

Inversion of the solution can be made similar to Eqs. (13,7,8). Introducing a normalized area function $a(z) = [A(z)/L] \times \int_0^L dz'/A(z')$, and neglecting the extrapolation length z_0, we obtain an expression for waveguide boundary function $a_0(z)$ in terms of the depth profile $\phi_0(z)$

$$a_0(z)/\left[1 + \left(W_0'(z)/2\right)^2\right]^{1/2} = \tag{13}$$
$$\left[(1-\tilde{\alpha})(1-\tilde{\alpha}(1-\phi_0(z)))^3(1-\phi_0(z))/\phi_0'^2(z)\right]^{1/2},$$

where subscript zero refers to $z_0 \to 0$ approximation, which is relaxed using scaling procedure in Eqs. (13,8).

REFERENCES

[1] E. Akkermans and G. Montambaux. *Mesoscopic Physics of Electrons and Photons*. Cambridge University Press, Cambridge, 2007.

[2] Ad Lagendijk, B. van Tiggelen, and D. S. Wiersma. Fifty years of anderson localization. *Physics Today*, 62(8):24–29, 2009.

[3] I. M. Vellekoop and A. P. Mosk. Universal optimal transmission of light through disordered materials. *Phys. Rev. Lett.*, 101:120601, 2008.

[4] W. Choi, A. P. Mosk, Q. Park, and W. Choi. Transmission eigenchannels in a disordered medium. *Phys. Rev. B*, 83:134207, 2011.

[5] M. Kim, Y. Choi, C. Yoon, W. Choi, J. Kim, Q. Park, and W. Choi. Maximal energy transport through disordered media with the implementation of transmission eigenchannels. *Nat Photon*, 6(9):581–585, 2012.

[6] S. M. Popoff, A. Goetschy, S. F. Liew, A. D. Stone, and H. Cao. Coherent control of total transmission of light through disordered media. *Phys. Rev. Lett.*, 112:133903, 2014.

[7] Benoît Gérardin, Jérôme Laurent, Arnaud Derode, Claire Prada, and Alexandre Aubry. Full transmission and reflection of waves propagating through a maze of disorder. *Phys. Rev. Lett.*, 113:173901, 2014.

[8] C.W. Hsu, A. Goetschy, Y. Bromberg, A. D. Stone, and H. Cao. Broadband coherent enhancement of transmission and absorption in disordered media. *Phys. Rev. Lett.*, 115:223901, 2015.

[9] M. Davy, Z. Shi, J. Park, C. Tian, and A. Z. Genack. Universal structure of transmission eigenchannels inside opaque media. *Nat Commun*, 6:1–6, 2015.

[10] O. S Ojambati, H. Yä lmaz, A. Lagendijk, A. P Mosk, and W. L. Vos. Coupling of energy into the fundamental diffusion mode of a complex nanophotonic medium. *New Journal of Physics*, 18(4):043032, 2016.

[11] R. Sarma, A. Yamilov, S. Petrenko, Y. Bromberg, and H. Cao. Control of energy density inside a disordered medium by coupling to open or closed channels. *Phys. Rev. Lett.*, 117:086803, 2016.

[12] Allard P. Mosk, Ad Lagendijk, Geoffroy Lerosey, and Mathias Fink. Controlling waves in space and time for imaging and focusing in complex media. *Nat Photon*, 6(5):283–292, 2012.

[13] S. M. Popoff, G. Lerosey, M. Fink, A. C. Boccara, and S. Gigan. Controlling light through optical disordered media: transmission matrix approach. *New Journal of Physics*, 13(12):123021–123032, 2011.

[14] I. M. Vellekoop. Feedback-based wavefront shaping. *Opt. Express*, 23(9):12189–12206, May 2015.

[15] J. Yoon, K. Lee, J. Park, and Y. Park. Measuring optical transmission matrices by wavefront shaping. *Opt. Express*, 23(8):10158–10167, 2015.

[16] H. Yu, J. Park, K. Lee, J. Yoon, K. Kim, S. Lee, and Y. Park. Recent advances in wavefront shaping techniques for biomedical applications. *Current Applied Physics*, 15(5):632 – 641, 2015.

[17] S. Rotter and S. Gigan. Light fields in complex media: Mesoscopic scattering meets wave control. *Rev. Mod. Phys.*, 89:015005, Mar 2017.

[18] O. S. Ojambati, A. P. Mosk, I. M. Vellekoop, A. Lagendijk, and W. L. Vos. Mapping the energy density of shaped waves in scattering media onto a complete set of diffusion modes. *Opt. Express*, 24(16):18525–18540, 2016.

[19] A. Peña, A. Girschik, F. Libisch, S. Rotter, and A. A. Chabanov. The single-channel regime of transport through random media. *Nat Commun*, 5:1–8, 2014.

[20] R. Sarma, A. Yamilov, S.F. Liew, M. Guy, and H. Cao. Control of mesoscopic transport by modifying transmission channels in opaque media. *Phys. Rev. B*, 92:214206, 2015.

[21] P. S. Burada, P. Hanggi, F. Marchesoni, G. Schmid, and P. Talkner. Diffusion in confined geometries. *ChemPhysChem*, 10(1):45–54, 2009.

[22] O.N. Dorokhov. Transmission coefficient and the localization length of an electron in n bound disordered chains. *JETP Lett.*, 36:318, 1982.

[23] Y. Imry. Active transmission channels and universal conductance fluctuations. *EPL (Europhysics Letters)*, 1(5):249, 1986.

[24] J. B. Pendry, A. MacKinnon, and P. J. Roberts. Universality classes and fluctuations in disordered systems. *Proceedings of the Royal Society of London A: Mathematical, Physical and Engineering Sciences*, 437(1899):67–83, 1992.

[25] Yu. V. Nazarov. Limits of universality in disordered conductors. *Phys. Rev. Lett.*, 73:134–137, 1994.

[26] M. P. van Albada M. B. van der Mark and Ad. Lagendijk. Light scattering in strongly scattering media: Multiple scattering and weak localization. *Phys. Rev. B*, 37:3575–3592, 1988.

[27] B. A. van Tiggelen, A. Lagendijk, and D. S. Wiersma. Reflection and transmission of waves near the localization threshold. *Phys. Rev. Lett.*, 84:4333–4336, 2000.

[28] B. Payne, A. Yamilov, and S.E. Skipetrov. Anderson localization as position-dependent diffusion in disordered waveguides. *Phys. Rev. B*, 82:024205, 2010.

[29] C. Tian. Hydrodynamic and field-theoretic approaches to light localization in open media. *Physica E: Low-dimensional Systems and Nanostructures*, 49:124– 153, 2013.

[30] C. W. Groth, M. Wimmer, A. R. Akhmerov, and X. Waintal. Kwant: a software package for quantum transport. *New Journal of Physics*, 16(6):063065, 2014.

[31] F. Scheffold, W. Hártl, G. Maret, and E. Matijević. Observation of long-range correlations in temporal intensity fluctuations of light. *Phys. Rev. B*, 56:10942–10952, 1997.

[32] X. Cheng, C. Tian, Z. Lowell, L. Zhao, and A. Z. Genack. Impact of surface reflection on transmission eigenvalue statistics and energy distributions inside random media. *The European Physical Journal Special Topics*, 226(7):1539–1548, 2017.

[33] A. Yamilov, S. Petrenko, R. Sarma, and H. Cao. Shape dependence of transmission, reflection, and absorption eigenvalue densities in disordered waveguides with dissipation. *Phys. Rev. B*, 93:100201, 2016.

IV. INVERSE DESIGN OF LONG-RANGE CORRELATION INTENSITY IN SCATTERING MEDIA

Milan Koirala[1] , Raktim Sarma[2], Hui Cao[2], and Alexey Yamilov[1]

[1]*Department of Physics, Missouri University of Science and Technology, Rolla, MO* 65409*, USA*

[2]*Department of Applied Physics, Yale University, New Haven, Connecticut 06520, USA*

ABSTRACT

We demonstrate a possibility to predictably control nonlocal correlation in mesoscopic transport of waves by tailoring the geometry of a disordered waveguide. In case of non-dissipative medium, we find an explicit relationship between correlation and the shape of the system. Inverting this relationship, we realize inverse design: we obtain specific waveguide shape that leads to a pre-determined non-local correlation. The proposed technique offers an approach to coherent control of wave propagation in random media that is complementary to wavefront shaping.

1. INTRODUCTION

Diffusion is a powerful and versatile description of the typical wave propagation [1–4] in scattering medium that disregards the phase and, thus, the possibility of interference. Persistent interferece phenomena such as universal conductance fluctuations, Anderson localization corrections, enhanced backscattering and nonlocal mesoscopic correlations [5–8] can be captured using the diagrammatic perturbation technique [3, 9–11]. The perturbation building block, which describes an interference of two propagation paths, is known as "quantum crossing", or Hikami box [12, 13]. The crossing, see Figure 1, is a local object

confined to a volume ℓ^d, where ℓ is the transport mean free path and d is the dimensionality of the system. This locality of the interference event means that it is independent of the exact shape of the considered geometry. In contrast, propagation between the source of waves to the interference site and on to the detector does depend on the geometry of the system, as seen from Figure 1. It is described in terms of ladder propagator, which is in essence a Green function $G(\mathbf{r}, \mathbf{r}')$ of the diffusion equation for the disorder-averaged intensity. Consequently, to describe the wave interference effects, the knowledge of $G(\mathbf{r}, \mathbf{r}')$ in the particular geometry is crucial.

In this work, we derive expressions for the Green function in the two- and three-dimensional disordered waveguides with an arbitrary shape in order to obtain the non-local long-range mesoscopic correlations [9, 14–21]. We adapt the projection technique, developed in physical chemistry for the particle diffusion in confined geometries [22, 23], to describe wave diffusion. We reduce the problem to one-dimension and obtain analytical solution. We further extend the projection technique to include the effects of absorption commonly encountered in experiments with the electromagnetic waves.

Spatial light modulator and related technologies have enabled manipulation of light propagation in scattering media via shaping the incident wavefront field to tailor it to the specific configuration of scatters in the sample [8, 24, 25]. This brought the renewed attention to the nonlocal correlations as they were found to be related to such transport parameters as focusing contrast inside the medium [26] and energy deposition [27**?** – 35]. The long-range correlation also affects total transmission via an optimized wave front with a limited degree of input control [21], it is also the key constraint determining the broadband transmission achievable in wavefront shaping [36]. Our derived analytical relation between the long-range correlation and the shape of the waveguide enables the inverse design: selecting the specific waveguide to obtain the desired correlation profile. Therefore, our work opens up additional avenues for coherent control of wave propagation in

diffusive scattering media. In recent works [35, 37, 37, 38], we fabricated two-dimensional disordered photonic waveguides with various geometries, which can be now be used to experimentally test the presented results.

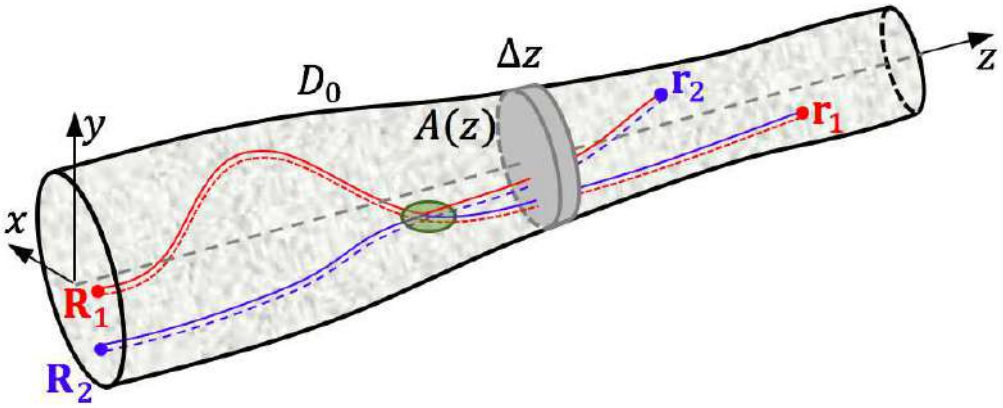

Figure 1. Schematic depiction of a disordered waveguide with varying diameter. In diagrammatic description of wave transport, the long-range correlation between intensities at $\mathbf{r}_1$ and $\mathbf{r}_2$ arises when two propagation paths, described by the Green function of diffusion equation, intersect allowing a swap of field amplitudes.

2. PROJECTION TECHNIQUE

In this section we outline the projection technique that allows one to reduce the two- or three-dimensional diffusion problem to one-dimension (1D). For completeness, in this section we will consider the non-stationary diffusion and will also include the effect of absorption.

Green function $G(\mathbf{r}, \mathbf{r}')$ of the diffusion equation is defined by the equation

$$\frac{\partial G(\mathbf{r}, \mathbf{r}', t)}{\partial t} - D_0 \nabla^2_{\mathbf{r}} G(\mathbf{r}, \mathbf{r}', t) + \frac{G(\mathbf{r}, \mathbf{r}', t)}{\tau_a} = S_0(t)\delta(\mathbf{r} - \mathbf{r}'), \tag{1}$$

where D_0 is the diffusion constant, τ_a is absorption time, and $S_0(t)$ is a point source at $\mathbf{r}'$. In context of light scattering, $G(\mathbf{r}, \mathbf{r}')$ represents an ensemble-averaged intensity in the medium with the corresponding source. The geometry of the 3D system is schematically depicted in Figure 1, with $0 \le z \le L$, $x^2 + y^2 \le [W(z)/2]^2$ in 3D or $-W(z)/2 \le y \le W(z)/2$ in

2D, where $W(z)$ is the diameter of the waveguide. The corresponding cross section area $A(z)$ is $\pi W^2(z)/4$ and $W(z)$ in 3D and 2D respectively. The boundary conditions consist of reflection (zero flux) condition $\partial G(\mathbf{r},\mathbf{r}',t)/\partial \mathbf{n} = 0$ at the walls of the waveguide and open boundary conditions at the two ends ($z = 0, L$), $[z_0 \partial G(\mathbf{r},\mathbf{r}',t)/\partial z \mp G(\mathbf{r},\mathbf{r}',t)]_{z=0,L} = 0$, where $z_0 = (\pi/4)\ell$ is extrapolation length [1].

In defining a projection to 1D, it is instructive to take a step back by writing Eq. 1 as a combination of the diffusive flux $\mathbf{J}(\mathbf{r},\mathbf{r}',t)$ and the continuity equations:

$$\begin{aligned} \mathbf{J}(\mathbf{r},\mathbf{r}',t) &= -D_0 \nabla_{\mathbf{r}} G(\mathbf{r},\mathbf{r}',t), && (2) \\ \frac{\partial G(\mathbf{r},\mathbf{r}',t)}{\partial t} &+ \nabla_{\mathbf{r}} \cdot \mathbf{J}(\mathbf{r},\mathbf{r}',t) + \frac{1}{\tau_a} G(\mathbf{r},\mathbf{r}',t) \\ &= S_0(t)\delta(\mathbf{r}-\mathbf{r}'). && (3) \end{aligned}$$

As the first step, we will perform an average over the position of the source $\mathbf{r}'$ in the cross-section plane at a fixed depth z' as $A^{-1}(z')\int_{A(z')} d\boldsymbol{\rho}' \times$, where $\boldsymbol{\rho}'$ is the transverse coordinate at z':

$$\begin{aligned} \mathbf{J}(\mathbf{r},z',t) &= -D_0 \nabla_{\mathbf{r}} G(\mathbf{r},z',t), && (4) \\ \frac{\partial G(\mathbf{r},z',t)}{\partial t} &+ \nabla_{\mathbf{r}} \cdot \mathbf{J}(\mathbf{r},z',t) + \frac{1}{\tau_a} G(\mathbf{r},z',t) \\ &= S_0(t)\delta(z-z')/A(z'). && (5) \end{aligned}$$

$G(\mathbf{r},z',t)$ represents the ensemble-averaged intensity at point $\mathbf{r}$ with a planar source $S_0(t)/A(z')$ at z'.

Presence of the divergence operator in Eq. 5 presents a challenge while performing averaging over the cross-section coordinate $\boldsymbol{\rho}$ in $\mathbf{r} \equiv (\boldsymbol{\rho}, z)$. Instead, we accomplish this task by performing integration over *volume* sandwiched between cross-sections at z and $z + \Delta z$,

see Figure 1. Using Gauss theorem, the volume integration is reduced to surface integration

$$\oint_V \nabla_{\mathbf{r}} \cdot \mathbf{J}(\mathbf{r}, z', t) d\mathbf{r} = \int_S \mathbf{J}(\mathbf{r}, z', t) \cdot \mathbf{n} d\sigma. \tag{6}$$

In the next step we separate the surface integral into three parts: a ring over the surface of the waveguide, and two cross-sections: one at z and $z+\Delta z$ each. The first contribution vanishes due to absence of the normal component of the flux at the boundary. The remaining two contributions to Eq. 6 are computed as follows

$$\begin{aligned} & - \int_{A(z)} J_z(\boldsymbol{\rho}, z, z', t) d\boldsymbol{\rho} + \int_{A(z+\Delta z)} J_z(\boldsymbol{\rho}, z+\Delta z, z', t) d\boldsymbol{\rho} \\ & \simeq \frac{1}{A(z)} \frac{\partial}{\partial z} \left[A(z) J_z(z, z', t) \right] \times A(z) \Delta z, \end{aligned} \tag{7}$$

where subscript z denotes the longitudinal component (of flux) and $J_z(z, z', t) \equiv A^{-1}(z) \int_{A(z)} J_z(\boldsymbol{\rho}, z, z', t) d\boldsymbol{\rho}$ the cross-section average. In Eq. 7 we accounted, in the leading order of Δz, for two possible sources of change in the value of the integral – one due to $\partial J_z(z, z', t)/\partial z$ and the other due to variability of the waveguide shape $dA(z)/dz$. Lastly, the volume integration of remaining terms in Eq. 5 does not pose problems, reducing them to the cross-sectional averages, e.g. $\oint_V G(\mathbf{r}, z', t) d\mathbf{r} \simeq \Delta z \times \int_{A(z)} G(\boldsymbol{\rho}, z, z', t) d\boldsymbol{\rho} \equiv G(z, z', t) \times [A(z) \Delta z]$.

Examining Eq. 7, we see that completion of our task of reducing the higher-dimensional problem to 1D requires expression for the longitudinal flux $J_z(z, z', t)$. Cross-sectional (surface) integration of the z-component of Eq. 4 yields $J_z(z, z', t) \simeq -D_0 \partial G(z, z', t)/\partial z$, which upon substitution in Eqs. (7,5) yields

$$\begin{aligned} \frac{\partial G(z, z', t)}{\partial t} & - \frac{1}{A(z)} \frac{\partial}{\partial z} \left[D_0 A(z) \frac{\partial G(z, z', t)}{\partial z} \right] \\ + \frac{1}{\tau_a} G(z, z', t) & = \frac{S_0(t)}{A(z)} \delta(z - z'), \end{aligned} \tag{8}$$

The above expression, together with similarly obtained boundary conditions $[z_0 \partial G(z,z',t)/\partial z \mp G(z,z',t)]_{z=0,L} = 0$, represents the final result of this section.

We would like to finish this discussion by putting it our result in context of the available literature. Particle diffusion in confined geometries is a common problem in physical chemistry, see for example Ref. [22] for a review. In this problem, it is convenient to define cross-section integrated (not averaged as above) quantity representing linear density $c(z,t)$ of e.g. a solute. The governing equation

$$\frac{\partial c(z,t)}{\partial t} - \frac{\partial}{\partial z}\left[D_0 A(z) \frac{\partial}{\partial z} \frac{c(z,t)}{A(z)}\right] = 0, \tag{9}$$

is known as Fick-Jacobs equation. It has been derived by Jacobs [39] heuristically based on the particle conservation argument, Zwanzig [40] via reducing higher dimensional Smoluchowski equation to 1D, and by others [41, 42]. We are not aware of reports of derivation such as the one presented above, in particular, in context of wave diffusion where there is no particle conservation constraint.

In context of particle diffusion, there was a considerable effort to evaluate the validity of the projection (reduction) to 1D via Eq. 9. It has been found [40–43] that even for rapidly varying channel profiles with $dW(z)/dz \sim 1$, a reliable solution can be obtained from a modified Fick-Jacobs equation with $D_0 \to D_0 \times (1 + W'^2(z))^{-\alpha}$, where $\alpha = 1/3, 1/2$ in 2D and 3D respectively. Hence, we surmise that similar substitution should extend the validity of Eq. 8 as well.

Having completed the derivation of Eq. (8), in the remainder of this work we will consider its static version (i.e. without the time-derivative term) to compute the long-range spatial correlation of intensity.

3. INTENSITY CORRELATION IN DISOREDERED WAVEGUIDES WITH VARYING CROSS SECTION

Intensity correlations originate due to interference in wave scattering and propagation, it was first considered for electronic waves in mesoscopic physics [9, 14, 44, 45]. The electromagnetic waves, such as visible light or microwaves, offer a convenient test bed for study of correlation with numerous practical applications [3, 11, 16, 17, 46, 47]. For incident plane wave, the spatial correlation is defined as

$$C(\mathbf{r}_1, \mathbf{r}_2) = \frac{\langle \delta I(\mathbf{r}_1) \delta I(\mathbf{r}_2) \rangle}{\langle I(\mathbf{r}_1) \rangle \langle I(\mathbf{r}_2) \rangle}, \tag{10}$$

where $\langle ... \rangle$ denotes the ensemble average and $\delta I(\mathbf{r}) = I(\mathbf{r}) - \langle I(\mathbf{r}) \rangle$ is the deviation intensity from its average at $\mathbf{r}$. This arrangement implies adding contributions from all trajectories originating from the front surface, i.e. at all possible $R_{1,2}$ in Figure 1.

Three universal, i.e. independent of the microscopical details of the disorder, contributions to $C(\mathbf{r}_1, \mathbf{r}_2)$ have been identified [3, 9, 48]: short-range C_1 decribing speckle pattern, long-range C_2 leading to e.g. fluctuations of transmission, and an infinite range C_3 underlying the universal conductance fluctuation [11, 49, 50]. Diagrammatically, interferences between waves scattered along independent paths give rise to C_1, one crossing of paths shown in Figure 1 generates C_2 , and two crossings cause C_3. The spatial correlation term $C_1(\mathbf{r}_1, \mathbf{r}_2)$ has unit magnitude but decays quickly when $|\mathbf{r}_1 - \mathbf{r}_2|$ exceeds the speckle size. $C_2(\mathbf{r}_1, \mathbf{r}_2) \propto 1/g$ but decays much more slowly, while $C_3(\mathbf{r}_1, \mathbf{r}_2) \propto 1/g^2$ has a constant contribution. g is the dimensionless conductance, which is large in diffusive systems considered here.

Serendipitously, averaging over cross-section of the waveguide such as that performed by the projection technique in the previous section, allows one to obtain the long-range correlation in the leading order of $1/g$ [19, 20]. Indeed, averaging over cross-section reduces the contribution of the short-range C_1 correlation by the factor $1/N$ (N is the number

of waveguide modes), whereas the contribution of $C_2 \propto 1/g$ remains unaffected because it is present at any value of the transverse coordinate. The ratio between their magnitudes is $g/N \propto \ell/L \ll 1$ for a strongly scattering system, here ℓ is transport mean free path and L is the length of the waveguide. Meanwhile, the contribution of the C_3 term remains smaller, at the level of $1/g^2$. Therefore, we conclude that

$$C_2(z_1, z_2) \simeq \frac{\langle \delta I(z_1) \delta I(z_2) \rangle}{\langle I(z_1) \rangle \langle I(z_2) \rangle}, \tag{11}$$

As seen above, the projection technique is perfectly suited for calculation of the long-range correlation, which we undertake next. We begin with an expression first obtained with the Langevin approach [15, 51]:

$$C_2(\mathbf{r}_1, \mathbf{r}_2) = a_d D_0^2 \frac{\int_V \langle I(\mathbf{r}) \rangle^2 \nabla_{\mathbf{r}} G(\mathbf{r}_1, \mathbf{r}) \cdot \nabla_{\mathbf{r}} G(\mathbf{r}_2, \mathbf{r}) d\mathbf{r}}{\langle I(\mathbf{r}_1) \rangle \langle I(\mathbf{r}_2) \rangle}. \tag{12}$$

Here, $G(\mathbf{r}, \mathbf{r}')$ is the Green function of the static version of the diffusion equation (1) with a constant source $S_0(t) \equiv 1$. $a_2 = 4/k\ell$ and $a_3 = 6\pi/k^2\ell$ is the dimensionality-dependent coefficient. Eq. (12) has a transparent diagrammatic interpretation. In this expression, $\langle I(\mathbf{r}) \rangle^2$ represents two diffusive paths connecting the input surface of the waveguide to a crossing point at $\mathbf{r}$; Green functions $G(\mathbf{r}_{1,2}, \mathbf{r})$ describe the diffuse propagation from $\mathbf{r}$ to the detectors at $\mathbf{r}_{1,2}$; and the gradient operators together with the constant prefactors originate from the interference (i.e. Hikami box) at $\mathbf{r}$. Finally, volume integration over $\mathbf{r}$ signifies averaging over all possible locations of interference.

Cross-sectional average of $\langle I(\mathbf{r}_{1,2}) \rangle$ terms in the denominator of Eq. (12) does not present challenges due to their weak dependence on the transverse coordinates, i.e. $\langle I(\mathbf{r}) \rangle \simeq \langle I(z) \rangle$. To proceed with the analytical calculation of Eq. (12), we average the nominator over the transverse components of $\mathbf{r}_1$ and $\mathbf{r}_2$. Although $\nabla_{\mathbf{r}} G(z_1, \mathbf{r}) \cdot \nabla_{\mathbf{r}} G(z_2, \mathbf{r})$ includes derivatives of the Green functions with respect to both longitudinal and transverse

coordinates, the former make the dominant contribution. Indeed, because the arguments of a Green function can be swapped, $\nabla_{\mathbf{r}} G(z_{1,2}, \mathbf{r})$ can be viewed as $\nabla_{\mathbf{r}} G(\mathbf{r}, z_{1,2})$. In this form, $G(\mathbf{r}, z)$ represents intensity at point $\mathbf{r}$ with a uniform planar source at the cross-section z. Such a source should not produce large transverse variation of intensity as long as the cross-section is not changing too rapidly, i.e. for a sufficiently small $dW(z)/dz$. Hence, we obtain

$$C_2(z_1, z_2) \simeq a_d D_0^2 \frac{\int_0^L \frac{\partial G(z_1, z)}{\partial z} \frac{\partial G(z_2, z)}{\partial z} \langle I(z) \rangle^2 A(z) dz}{\langle I(z_1) \rangle \langle I(z_2) \rangle}, \tag{13}$$

where $G(z, z')$ is the solution of the static version of the diffusion equation (with a constant source $S_0(t) \equiv 1$) we obtained previously using projection technique, c.f. Eq. (8). $\langle I(z) \rangle$ is the solution of the same equation with $S_0(t) \equiv 0$, and a constant value at $z = 0$, as will be discussed in the next section. Eq. (13) together with the static version of Eq. (8) have rather broad applicability, for example, they can incorporate the effects of absorption or gain on the correlations [20, 52].

4. LONG-RANGE CORRELATIONS IN LOSSLESS DISORDERED WAVEGUIDES

In this section we demonstrate that, without absorption, the long-range intensity correlation can be obtained in a closed form for an arbitrary slow-varying ($dW(z)/dz < 1$) waveguide geometry. To that end, we introduce a change of spatial variable

$$\zeta(z) = \frac{\frac{z_0}{A(0)} + \int_0^z \frac{d\tilde{z}}{A(\tilde{z})}}{\frac{z_0}{A(0)} + \int_0^L \frac{d\tilde{z}}{A(\tilde{z})} + \frac{z_0}{A(L)}}. \tag{14}$$

In terms of this variable, the defining equation for Green function takes a simple form

$$-\frac{\partial^2 G(\zeta, \zeta')}{\partial \zeta^2} = \delta(\zeta - \zeta') \tag{15}$$

with constant factors absorbed in the definition of the Green function to make it dimensionless. Furthermore, extending the region applicability of ζ from $\zeta_0 \le \zeta \le \zeta_L$ to $0 \le \zeta \le 1$ allows to also simplify boundary conditions to $G(\zeta, \zeta')|_{\zeta=0,1} = 0$. Here ζ_0 and ζ_L are defined by inserting $z = 0$ and L in Eq. 14 respectively. Eq. 13 for the long-range correlation takes form

$$C_2(\zeta_1, \zeta_2) \simeq \tilde{a}_d \frac{\int_{\zeta_0}^{\zeta_L} \frac{\partial G(\zeta_1, \zeta)}{\partial \zeta} \frac{\partial G(\zeta_2, \zeta)}{\partial \zeta} \langle I(\zeta) \rangle^2 d\zeta}{\langle I(\zeta_1) \rangle \langle I(\zeta_2) \rangle}, \tag{16}$$

where $\langle I(\zeta) \rangle$ satisfies homogeneous version of Eq. 15 with $\langle I(\zeta_0) \rangle = I_0$ and $\langle I(1) \rangle = 0$ boundary conditions; and $\tilde{a}_d = a_d \times [z_0/A(0) + \int_0^L A^{-1}(z)dz + z_0/A(L)]$.

The final expression for the long-range correlation can now be obtained substituting the solution of Eq. 15

$$G(\zeta, \zeta') = \begin{cases} \zeta(1 - \zeta'), & \zeta < \zeta' \\ \zeta'(1 - \zeta), & \zeta > \zeta' \end{cases} \tag{17}$$

and the corresponding intensity as $\langle I(\zeta) \rangle = I_0(1 - \zeta)/(1 - \zeta_0)$ into Eq. 16. We obtain

$$C_2(\zeta_1, \zeta_2) = \frac{2}{3g} \left[\zeta_1(2 - \zeta_1) + \frac{\zeta_1}{1 - \zeta_1}(1 - \zeta_2)^2 \right], \tag{18}$$

where $\zeta_{1,2} \equiv \zeta(z_{1,2})$ as defined by Eq. 14, and the dimensionless conductance is introduced via $g = 2/\tilde{a}_d$. When $\zeta_1 = \zeta_2$, Eq. 18 yields

$$C_2(\zeta, \zeta) = \frac{2\zeta}{g} \left(1 - \frac{2\zeta}{3} \right). \tag{19}$$

This quantity corresponds to the leading non-Rayleigh contribution to the fluctuation of intensity and originates in non-locality of wave transport. Both Eqs. (18,19) reduce to known expressions for waveguides with constant cross-section, in this case $\zeta(z) = (z+z_0)/(L+2z_0)$, which can be found from Eq. 14.

We would like to point out several general properties of Eqs. (18,19) that are common to all waveguides irrespective of their shape. For the sake of simplicity, we will assume that small corrections $z_0/L \sim \ell/L \ll 1$ can be neglected. We find that $g = (2/a_d)/[\int_0^L A^{-1}(z)dz]$; $C_2(L,L) = 2/(3g)$; the maximum value of the correlation $\max[C_2(\zeta_1,\zeta_2)] = C_2(\zeta_{max},\zeta_{max}) = (9/8) \times 2/(3g)$, where $\zeta_{max} = 3/4$. $C_2(\zeta,\zeta)$ is a monotonically increasing function of ζ between 0 and ζ_{max} and a monotonically decreasing between ζ_{max} and 1. Furthermore, $C_2(\zeta,\zeta) \leq 2/(3g)$ for $0 \leq \zeta \leq (1/2)$ and $2/(3g) \leq C_2(\zeta,\zeta) \leq 3/(4g)$ in the interval for $(1/2) \leq \zeta \leq 1$. Remarkably, $C_2(\zeta,\zeta)$ varies by less than 12% in the second interval. The long-range correlation between the output intensity at $\zeta_2 = 1$ and that in the interior of the sample is $C_2(\zeta,1) = 2/(3g)\zeta(2-\zeta)$. It decays monotonically with distance from the output surface, however, the rate of the decay is determined by the $\zeta(z)$, which is set by the shape of the waveguide. In a waveguide with constant cross-section, $C_2(z,L) \simeq 2/(3g)z/L[2 - z/L]$ in agreement with Ref. [51].

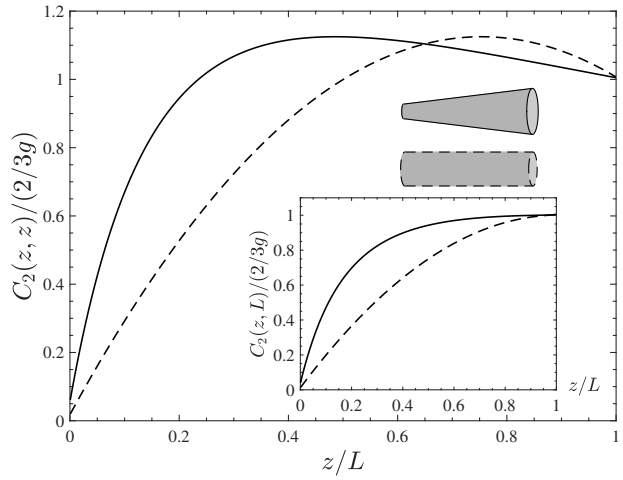

Figure 2. Solid line in the main plot depicts $C_2(z,z)$ in a three-dimensional expanding disordered waveguide shown in the inset, see text for system parameters. The dashed line depicts the same quantity for the waveguide of constant width. The inset plots the long-range correlation $C_2(z,L)$ for the two cases in the main plot.

Eq. 18 also predicts correlation between intensities at $z = 0, L$ surfaces. In this case, z_0 terms cannot be neglected as they make the leading contribution to ζ_0 and, therefore, have to be retained. Evaluation of $C_2(\zeta_0,\zeta_L)$ gives $2/(3N_0)$ in both two and three dimensions,

where N_0 is the number of waveguide modes at the input cross-section $z = 0$. Correlation between the transmitted and reflected intensities has been studied theoretically [53, 54] and experimentally [55]. It was found to be negatively correlated at the level of $-2/(3N_0)$. Because an increase of intensity at the front surface (positive correlation) corresponds to a reduction (negative correlation) of the reflected intensity, our results are in agreement with Ref. [54]. In addition, the maximum value of $C_2(z_{max}, z_{max}) = (9/8) \times 2/(3g)$, independent of the extrapolation length z_0. The leading term for $C_2(0,0) \simeq 1/N_0$ corresponds to addition of N_0 uncorrelated modes. In contrast, at output surface, the leading correction is $C_2(L, L) \simeq 2/(3g) + 1/(3N_L)$, where N_L is the number of modes at the output.

Figure 2 illustrates the dependence of the correlation on the shape of the waveguide by plotting $C_2(z, z)$ and $C_2(z, L)$ for an expanding disordered waveguide, in which the diameter $W(z)$ is a linear function of z. We used the following parameters $L = 100\ell$, $k\ell = 10$, $A(0) = 100\ell^2$, $A(L) = 1000\ell^2$, $z_0 = (2/3)\ell$, that correspond to $g \simeq 33$. For comparison, we also plot with dash line the same quantities for the waveguide of constant width equal to $A = 550\ell^2$, in this case $g = 58$. We can clearly see that the shape of the waveguide can have a significant effect on the correlation. Specifically, the reduced width at the front end led to a steeper increase of both $C_2(z, z)$ and $C_2(z, L)$ for small z. This dependence can be deduced e.g from Eq. 19 as $dC_2(z, z)/dz \propto \zeta'(z) \propto A^{-1}(z)$ for $\zeta \ll 1$. Therefore, narrower opening of the linearly expanding waveguide leads to a steeper increase of correlation in the first half of the sample in Figure 2. Since the maximum value correlations is bounded from above by the value $3/4g$, a rapid increase at the beginning of the waveguide, inadvertently leads to to a weaker dependence towards $z = L$. In case of $C_2(z, z)$, as was discussed above, once the maximum value of $3/4g$ is reached at z_{max}, in the remainder of the system the function varies in only a narrow range $2/3g \leq C_2(z, z) \leq 3/4g$, see Figure 2.

To conclude this section, we note that since $\zeta(z)$ is determined by $A(z)$ via Eq. 14, one can exploit the freedom of choice the shape of the waveguide in order to predictably manipulate the correlation, within the constraints imposed by the general properties above. We tackle this task below.

5. INVERSE DESIGN OF THE LONG-RANGE CORRELATION

The compact-form analytical expression given in Eq. 18 establishes a relation between shape of the diffusive waveguide and correlation $C_2(z_1, z_2)$ of the cross-section averaged intensity, thus enabling the predictive (inverse) design. Two comments are in order. First, $C_2(z_1, z_2)$ is the function of two variable whereas $A(z)$ is of one, so the task is not well defined. To circumvent this problem, we going to consider two possible mappings: one from the diagonal (fluctuation) $C_2(z, z)$, and the other from the off-diagonal (correlation) $C_2(z, L)$ functions. The second comment concerns the constrains imposed on possible $C_2(z, z)$ and $C_2(z, L)$. Indeed, as discussed in previous sections, see also Figure 2, neither of the two mappings allow an arbitrary input functions. For example, neglecting z_0, $C_2(z, z)$ has to be monotonically increasing from 0 to a maximum and then monotonically decreasing to $8/9$ of the maximum value at the output. Likewise, $C_2(z, L)$ has to be a monotonically increasing function of z. Below, we obtain such constrained mappings.

Solving Eq. 19 for ζ and then inverting $\zeta(z)$ with the help of Eq. 14 we obtain

$$A(z) = a_d \frac{\sqrt{1 - \frac{4g}{3} C_2(z, z)}}{\left| \frac{dC_2(z, z)}{dz} \right|}. \tag{20}$$

The structure of this relationship is intimately related to the constraints we imposed on $C_2(z, z)$. Indeed, the $4g/3$ factor ensures that the expression under the square root remains positive or zero. The latter case corresponds to the maximum of the function at z_{max}, where

both the nominator and denominator of Eq. 20 turn to zero simultaneously. To prevent $A(z)$ from turning to zero or having a singularity, we need to ensure that $C_2(z,z)$ has a parabolic behavior in the vicinity of its maximum.

Following steps similar to those used to arrive at Eq. 20, we find

$$A(z) = \frac{2a_d}{3} \frac{\sqrt{1 - \dfrac{C_2(z,L)}{C_2(L,L)}}}{\left|\dfrac{dC_2(z,L)}{dz}\right|}. \tag{21}$$

Unlike Eq. 20, where the maximum value of the input function was related to conductance using a simple relationship, the maximum value of $C_2(z,L)$ at $z = L$ is only approximately equal to $2/(3g)$ with additional (smaller) corrections due to the finite extrapolation length z_0. Hence, normalization by $C_2(L,L)$ guarantees that the expression under the square root does not fall below zero. Similar to Eq. 20, the vanishing of $dC_2(z,L)/dz$ in Eq. 21 at $z = L$ coincides with a zero of the nominator, preventing a singularity.

Equations (20,21) open a possibility of inverse design. As an example, we design a waveguide where the diagonal term $C_2(z,z)$ is a (nearly) piece-wise linear function. As discussed in previous sections, a choice of model correlations is constrained by their properties. Therefore, we set out to find a functional form of $A(z)$, such that

$$C_2(z,z) = \begin{cases} \dfrac{z}{z_c} \times \dfrac{3}{4g}, & z < z_c \\ \dfrac{L-z}{L-z_c} \times \dfrac{1}{12g} + \dfrac{2}{3g}, & z > z_c \end{cases} \tag{22}$$

where we neglected by the small corrections at $z = 0, L$ due to the extrapolation effect. This function has chosen to satisfy the following constraints: (i) it monotonically increases in $0 < z < z_c$; (ii) it monotonically decreases in $z_c < z < L$; (iii) it maximum value is $3/4g$ at z_c; and (iv) its value is $2/3g$ at $z = L$. However, the model function does not have a vanishing derivative at its maximum at z_c. This should result in an artifact to be corrected

at a later step. Substitution of Eq. 22 into Eq. 20 gives

$$A(z) = \frac{4ga_d}{3} \begin{cases} \sqrt{(z_c - z)z_c}, & z < z_c \\ 3\sqrt{(z - z_c)(L - z_c)}, & z > z_c \end{cases} \tag{23}$$

We observe that Eq. 23 predicts a zero cross-section at z_c. To avoid this artifact, related to a cusp in the input function in Eq. 22, we add a condition that $A(z)$ does not fall below a certain minimum value of A_{min}.

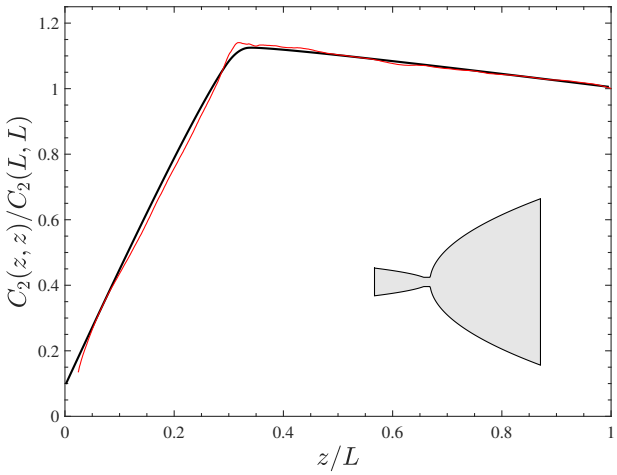

Figure 3. Thick solid line in the main plot depicts $C_2(z, z)$ in a two-dimensional expanding disordered waveguide defined by Eq. 23. Thin line is the result of numerical simulation. The inset plots the shape of the considered waveguide.

To test the above prediction we substitute Eq. 23 into Eqs. (14,18) to compute the long-range correlation in a two-dimensional disordered waveguide with parameters quoted below. Thick solid line in Figure 3 shows that the $C_2(z, z)$ is indeed close to a piece-wise linear function. The deviations from the input Eq. 22 can be seen at $z \sim 0$ and $\sim z_c$. The former is due to the fact that the model equation did not explicitly account for the extrapolation length z_0. Replacement of a cusp-behavior at z_c with a smooth parabolic maximum is related to the structure of Eq. 20 as well as our our insistence on $A(z)$ to be always greater than A_{min}. One can see from Figure 3, however, that this did not cause significant deviation from linearity away from the maximum.

To further verify the predictions of our inverse-design procedure, we performed numerical simulations. We consider a two-dimensional waveguide where $A(z) = W(z)$, and use the following parameters: $N_0 = 125$, $L/\ell \simeq 30$, $W(0)/\ell \simeq 5$, $W_{min}/W(0) = 1/3$, $z_c = L/3$ and $g \simeq 7$. The simulation are performed using method described in detail in our previous works [23, 32, 56]. Cross-section averaged intensity was obtained numerically by solving wave equation and then was used to compute $C(z_1, z_2)$ using Eq. 11. The angular brackets represent average over 1000 disorder realizations. The transport mean free path was obtained by computing the dimensionless conductance for a rectangular waveguide and then using relationship $g = (\pi/2)N\ell/(L + 2z_0)$, where N is the number of waveguide modes. This allowed us to express all length scales in terms of ℓ, with the numerical values quoted above.

Equation (11) holds only approximately, because averaging over cross-section of the waveguide does not fully remove other contributions. In order to compare the numerical simulation with our theoretical prediction, which only accounts for C_2 contribution, we removed the following two residuals. The first is related to C_1 contribution and can be evaluated by noticing that cross-sectional averaging of intensities in $W^{-2}(z) \iint \langle \delta I(z_1, y)\delta I(z_2, y + \Delta y)\rangle dy d\Delta y$ has a small but z-dependent contribution, which can be computed as

$$C_1(z, z) \simeq \frac{1}{W(z)} \int_0^{W(z)} C_1(\Delta y) d\Delta y. \tag{24}$$

Away from boundaries $z \sim 0, L$, the short-range correlation [18, 44] $C_1(\Delta y)$ can be evaluated in two dimensions in terms of Bessel function [57] as $J_0^2(k\Delta y)$. The second residual related to another type of correlation, C_0 [58], which is non-universal. This contribution has been related to the variance of the local density of states [59], [60], which we compute directly in our numerical simulations. The smallness of the two contributions is determined by $1/(kW)$ and $1/(k\ell)$ parameters respectively. Therefore, in larger systems and, particularly in three-dimensional systems, these residuals are expected to be negligible.

Thin line in Figure 3 shows the results of the numerically computed $C_2(z,z)$ after subtracting the two residual contributions described above. As predicted by Eq. 22, $C_2(z,z)$ exhibits nearly linear dependence in both $0 < z < z_c$ and $z_c < z < L$ intervals. We attribute deviation in the $z \sim 0$ region to the remaining ballistic intensity of the incident waves.

6. CONCLUSIONS

In this work, we first present a method to compute the Green function of the diffusion equation in two- and three-dimensional disordered waveguides with varying shape. This is accomplished by reducing the dimensionality of the problem to 1D. Because geometry dependence of the long-range intensity correlations arises from that in Green functions, the complexity of the problem of determining the correlations is greatly reduced. Furthermore, in case of lossless media, we are able to obtain close-form analytical expression for both Green function and the long-range correlation in arbitrary geometry. This relationship allows us to design specific waveguide shapes with unusual pre-determined non-local correlations, which we confirm with the direct numerical simulations. We refer to this approach as an inverse design. It is worth noting that the possibility of inversion of the *non-local long-range* correlations via rather simple Eqs. (20,21) is rather surprising.

Experimental measurement of the long-range correlation in our previous work [20] in photonic disordered waveguides already showed shape dependence. The results agreed with theoretical predictions based on Eq. 12. In waveguides other than rectangular, we had to resort to numerical calculation of the full two-dimensional Green function. Although samples in Ref. [20] exhibited absorption and our analytical results for passive systems in the last section do not apply, Eq. 13 does. Therefore, results of this work offer a much simpler approach based on the projection technique.

Our technique of studying geometry dependence of intensity correlations can be extended to studying other interference phenomena such as localization-induced position-dependent diffusion, transmission eigenchannels etc, see e.g. Refs. [8, 23, 61]. Our results are applicable to electronic, acoustic, electromagnetic and other types of waves and can incorporate the effect of absorption or optical gain.

ACKNOWLEDGMENTS

The authors acknowledge support from the U.S. National Science Foundation under Grant No. DMR-1205223, DMR-1205307.

REFERENCES

[1] P. M. Morse and H. Feshbach. *Methods of theoretical physics*, volume 22. AAPT, 1954.

[2] A. Ishimaru. *Wave Propagation and Scattering in Random Media*. Academic Press, 1978.

[3] M. C. W. van Rossum and Th. M. Nieuwenhuizen. Multiple scattering of classical waves: microscopy, mesoscopy, and diffusion. *Rev. Mod. Phys.*, 71:313–371, 1999.

[4] L. V. Wang and H. Wu. *Biomedical optics: principles and imaging*. John Wiley & Sons, 2007.

[5] BL Altshuler, PA Lee, and RA Webb. *Mesoscopic phenomena in solids*. Elsevier, 1991.

[6] C. W. J. Beenakker. Random-matrix theory of quantum transport. *Rev. Mod. Phys.*, 69:731–808, 1997.

[7] Ad Lagendijk, B. van Tiggelen, and D. S. Wiersma. Fifty years of anderson localization. *Physics Today*, 62(8):24–29, 2009.

[8] S. Rotter and S. Gigan. Light fields in complex media: Mesoscopic scattering meets wave control. *Rev. Mod. Phys.*, 89:015005, Mar 2017.

[9] R. Berkovits and S. Feng. Correlations in coherent multiple scattering. *Physics Reports*, 238(3):135–172, 1994.

[10] P. Sheng. *Introduction to wave scattering, localization and mesoscopic phenomena*, volume 88. Springer Science & Business Media, 2006.

[11] E. Akkermans and G. Montambaux. *Mesoscopic Physics of Electrons and Photons*. Cambridge University Press, Cambridge, 2007.

[12] LP Gorḱov, AI Larkin, and DE Khmelńitskiĭ. Particle conductivity in a two-dimensional random potential. *JETP Lett*, 30(4), 1979.

[13] S. Hikami. Anderson localization in a nonlinear-σ-model representation. *Phys. Rev. B*, 24:2671–2679, 1981.

[14] M.J. Stephen and G. Cwilich. Intensity correlation functions and fluctuations in light scattered from a random medium. *Phys. Rev. Lett.*, 59:285–287, 1987.

[15] R. Pnini and B. Shapiro. Fluctuations in transmission of waves through disordered slabs. *Phys. Rev. B*, 39:6986–6994, 1989.

[16] A. Z. Genack, N. Garcia, and W. Polkosnik. Long-range intensity correlation in random media. *Phys. Rev. Lett.*, 65:2129–2132, 1990.

[17] A.A Lisyansky and D. Livdan. Influence of internal reflection on correlation of intensity fluctuation in random media. *Phys. Rev. B*, 47:14157–14164, 1993.

[18] P. Sebbah, R. Pnini, and A. Z. Genack. Field and intensity correlation in random media. *Phys. Rev. E*, 62:7348–7352, 2000.

[19] R. Sarma, A. Yamilov, P. Neupane, B. Shapiro, and H. Cao. Probing long-range intensity correlations inside disordered photonic nanostructures. *Phys. Rev. B*, 90:014203–014207, 2014.

[20] R. Sarma, A. Yamilov, P. Neupane, and H. Cao. Using geometry to manipulate long-range correlation of light inside disordered media. *Phys. Rev. B*, 92:180203, 2015.

[21] C.H Hsu, S.F. Liew, A. Goetschy, H. Cao, and A.D. Stone. Correlation-enhanced control of wave focusing in disordered media. *Nature Physics*, 13:497–501, 2017.

[22] P. S. Burada, P. Hanggi, F. Marchesoni, G. Schmid, and P. Talkner. Diffusion in confined geometries. *ChemPhysChem*, 10(1):45–54, 2009.

[23] M. Koirala, R. Sarma, H. Cao, and A. Yamilov. Inverse design of perfectly transmitting eigenchannels in scattering media. *Phys. Rev. B*, 96:0542091–0542096, 2017.

[24] Allard P. Mosk, Ad Lagendijk, Geoffroy Lerosey, and Mathias Fink. Controlling waves in space and time for imaging and focusing in complex media. *Nat Photon*, 6(5):283–292, 2012.

[25] H. Yu, J. Park, K. Lee, J. Yoon, K. Kim, S. Lee, and Y. Park. Recent advances in wavefront shaping techniques for biomedical applications. *Current Applied Physics*, 15(5):632 – 641, 2015.

[26] X. Cheng and A. Z. Genack. Focusing and energy deposition inside random media. *Opt. Lett.*, 39(21):6324–6327, 2014.

[27] W. Choi, A. P. Mosk, Q. Park, and W. Choi. Transmission eigenchannels in a disordered medium. *Phys. Rev. B*, 83:134207, 2011.

[28] Benoît Gérardin, Jérôme Laurent, Arnaud Derode, Claire Prada, and Alexandre Aubry. Full transmission and reflection of waves propagating through a maze of disorder. *Phys. Rev. Lett.*, 113:173901, 2014.

[29] M. Davy, Z. Shi, J. Wang, X. C. Tian, and A. Z. Genack. Transmission eigenchannels and the densities of states of random media. *Phys. Rev. Lett.*, 114:033901, 2015.

[30] M. Davy, Z. Shi, J. Park, C. Tian, and A. Z. Genack. Universal structure of transmission eigenchannels inside opaque media. *Nat Commun*, 6:1–6, 2015.

[31] L. Zhao, C. Tian, Y. P. Bliokh, and V. Freilikher. Controlling transmission eigenchannels in random media by edge reflection. *Phys. Rev. B*, 92:094203–094219, 2015.

[32] R. Sarma, A. Yamilov, S. Petrenko, Y. Bromberg, and H. Cao. Control of energy density inside a disordered medium by coupling to open or closed channels. *Phys. Rev. Lett.*, 117:086803, 2016.

[33] O. S Ojambati, H. Yä lmaz, A. Lagendijk, A. P Mosk, and W. L. Vos. Coupling of energy into the fundamental diffusion mode of a complex nanophotonic medium. *New Journal of Physics*, 18(4):043032, 2016.

[34] O. S. Ojambati, A. P. Mosk, I. M. Vellekoop, A. Lagendijk, and W. L. Vos. Mapping the energy density of shaped waves in scattering media onto a complete set of diffusion modes. *Opt. Express*, 24(16):18525–18540, 2016.

[35] R. Sarma, A. Yamilov, and H. Cao. Enhancing light transmission through a disordered waveguide with inhomogeneous scattering and loss. *Applied Physics Letters*, 110(2):0211031–0211034, 2017.

[36] C.W. Hsu, A. Goetschy, Y. Bromberg, A. D. Stone, and H. Cao. Broadband coherent enhancement of transmission and absorption in disordered media. *Phys. Rev. Lett.*, 115:223901, 2015.

[37] R. Sarma, A. Yamilov, S.F. Liew, M. Guy, and H. Cao. Control of mesoscopic transport by modifying transmission channels in opaque media. *Phys. Rev. B*, 92:214206, 2015.

[38] R. Sarma, T. Golubev, A. Yamilov, and H. Cao. Control of light diffusion in a disordered photonic waveguide. *Applied Physics Letters*, 105(4):0411041–0411045, 2014.

[39] M. H. Jacobs. *Diffusion Processes*. Springer Berlin Heidelberg, Berlin, Heidelberg, 1967.

[40] R. Zwanzig. Diffusion past an entropy barrier. *The Journal of Physical Chemistry*, 96(10):3926–3930, 1992.

[41] D. Reguera and J. M. Rubí. Kinetic equations for diffusion in the presence of entropic barriers. *Phys. Rev. E*, 64:061106–061113, 2001.

[42] P. Kalinay and J. K. Percus. Corrections to the fick-jacobs equation. *Phys. Rev. E*, 74:041203–041206, 2006.

[43] P.S. Burada, G. Schmid, D. Reguera, J. M. Rubí, and P. Hänggi. Biased diffusion in confined media: Test of the fick-jacobs approximation and validity criteria. *Phys. Rev. E*, 75:051111–051118, 2007.

[44] B. Shapiro. Large intensity fluctuations for wave propagation in random media. *Phys. Rev. Lett.*, 57:2168–2171, 1986.

[45] S. Feng, C. Kane, P. A. Lee, and A. D. Stone. Correlations and fluctuations of coherent wave transmission through disordered media. *Phys. Rev. Lett.*, 61:834–837, 1988.

[46] J. F. de Boer, M. P. van Albada, and Ad. Lagendijk. Transmission and intensity correlations in wave propagation through random media. *Phys. Rev. B*, 45:658–666, 1992.

[47] F. Scheffold, W. Hártl, G. Maret, and E. Matijević. Observation of long-range correlations in temporal intensity fluctuations of light. *Phys. Rev. B*, 56:10942–10952, 1997.

[48] P. Sebbah, B. Hu, A. Z. Genack, R. Pnini, and B. Shapiro. Spatial-field correlation: The building block of mesoscopic fluctuations. *Phys. Rev. Lett.*, 88:123901, 2002.

[49] P. A. Lee and D. A. Stone. Universal conductance fluctuations in metals. *Phys. Rev. Lett.*, 55:1622–1625, 1985.

[50] F. Scheffold and G. Maret. Universal conductance fluctuations of light. *Phys. Rev. Lett.*, 81:5800–5803, 1998.

[51] R. Pnini and B. Shapiro. Intensity correlation in absorbing random media. *Physics Letters A*, 157(4):265–269, 1991.

[52] A. Yamilov, S.H. Chang, A. Burin, A. Taflove, and H. Cao. Field and intensity correlations in amplifying random media. *Phys. Rev. B*, 71:092201, 2005.

[53] N. Fayard, A. Cazé, R. Pierrat, and R. Carminati. Intensity correlations between reflected and transmitted speckle patterns. *Phys. Rev. A*, 92:0338271–0338278, 2015.

[54] N. Fayard, A. Goetschy, R. Pierrat, and R. Carminati. Mutual information between reflected and transmitted speckle images. *Phys. Rev. Lett.*, 120:073901–073905, 2018.

[55] I. Starshynov, A. M. Paniagua-Diaz, N. Fayard, A. Goetschy, R. Pierrat, R. Carminati, and J. Bertolotti. Non-gaussian correlations between reflected and transmitted intensity patterns emerging from opaque disordered media. *Phys. Rev. X*, 8:021041–021055, 2018.

[56] A. Yamilov, S. Petrenko, R. Sarma, and H. Cao. Shape dependence of transmission, reflection, and absorption eigenvalue densities in disordered waveguides with dissipation. *Phys. Rev. B*, 93:100201, 2016.

[57] A. Yamilov. Relation between channel and spatial mesoscopic correlations in volume-disordered waveguides. *Phys. Rev. B*, 78:045104–045110, 2008.

[58] B. Shapiro. New type of intensity correlation in random media. *Phys. Rev. Lett.*, 83:4733–4735, 1999.

[59] B. A. van Tiggelen and S. E. Skipetrov. Fluctuations of local density of states and C_0 speckle correlations are equal. *Phys. Rev. E*, 73:045601–045604, 2006.

[60] M. D. Birowosuto, S. E. Skipetrov, W. L. Vos, and A. P. Mosk. Observation of spatial fluctuations of the local density of states in random photonic media. *Phys. Rev. Lett.*, 105:013904–013907, 2010.

[61] A. Yamilov, Raktim R. Sarma, B. Redding, B. Payne, H. Noh, and H. Cao. Position-dependent diffusion of light in disordered waveguides. *Phys. Rev. Lett.*, 112:023904, Jan 2014.

V. CRITICAL STATES EMBEDDED IN THE CONTINUUM

Milan Koirala[1] , Alexey Yamilov[1], Ali Basiri[2], Yaroon Bromberg[3], Hui Cao[2], and Tsampikos Kottos[2]

[1]*Department of Physics, Missouri University of Science and Technology, Rolla, MO* 65409*, USA*

[2]*Department of Physics, Wesleyan University, Middletown, CT-06459, USA*

[3]*Department of Applied Physics, Yale University, New Haven, Connecticut 06520, USA*

ABSTRACT

We introduce a class of critical states which are embedded in the continuum (CSC) of one-dimensional optical waveguide array with one non-Hermitian defect. These states are at the verge of being fractal and have real propagation constant. They emerge at a phase transition which is driven by the imaginary refractive index of the defect waveguide and it is accompanied by a mode segregation which reveals analogies with the Dicke super-radiance. Below this point the states are extended while above they evolve to exponentially localized modes. An addition of a background gain or loss can turn these localized states to bound states in the continuum.

1. INTRODUCTION

A widespread preconception in quantum mechanics is that a finite potential well can support stationary solutions that generally fall into one of the following two categories: (a) Bound states that are square integrable and correspond to discrete eigenvalues that are below a well-defined continuum threshold; and (b) Extended states that are not normalizable

and they are associated with energies that are distributed continuously above the continuum threshold [1]. This generic picture has further implications. For example it was used by Mott [2] in order to establish the existence of sharp mobility edges between localized and extended wavefunctions in disordered systems. Specifically it was argued that a degeneracy between a localized and an extended state would be fragile to any small perturbation which can convert the former into the latter. Nevertheless, von Neumann and Wigner succeeded to produce a counterintuitive example of a stationary solution which is square integrable and its energy lies above the continuum threshold [3]. These, so-called, Bound States in the Continuum (BIC) can provide a pathway to confine various forms of waves like light [4–7], acoustic, water waves [8, 9], and quantum [10] waves as much as to manipulate nonlinear phenomena in photonic devices for applications to biosensing and impurity detection [11]. Interestingly, these ideas have also migrated to the non-linear domain [12, 13].

Although most of the studies on the formation of BIC states have been limited to Hermitian systems there are, nevertheless, some investigations that address the same question in the framework of non-Hermitian wave mechanics [14]. Along the same lines the investigation of defect modes in the framework of $\mathcal{PT}$-symmetric optics [15–18] has recently attracted some attention. In many occasions, however, the resulting BIC states are associated with very complex potentials which are experimentally challenging.

In this paper we introduce a previously unnoticed class of critical states which are embedded in the continuum (CSC). We demonstrate their existence using a simple set-up consisting of N coupled optical waveguides with one non-Hermitian (with loss or gain) defective waveguide in the middle. Similarly to BIC they have real propagation constant; albeit their envelop resembles a fractal structure. Namely their inverse participation number $\mathcal{I}_2$ scales anomalously with the size of the system N as

$$\mathcal{I}_2 \equiv \frac{\sum_n |\phi_n|^4}{(\sum_n |\phi_n|^2)^2} \sim \frac{\log(N+1)}{(N+1)} \tag{1}$$

Above ϕ_n is the wavefunction amplitude at the $n-$th waveguide. The CSC emerges in the middle of the band spectrum when the imaginary index of refraction of the defective waveguide $\epsilon_0^{(I)}$ becomes $|\epsilon_0^{(I)}| = 2V$ where V is the coupling constant between nearby waveguides. Below this value all modes are extended while in the opposite limit the CSC becomes exponentially localized with an inverse localization length $\xi^{-1} = \ln[2V/(|\epsilon_0^{(I)}| - \sqrt{(\epsilon_0^{(I)})^2 - 4V^2})]$. The localization-delocalization transition is accompanied with a mode re-organization in the complex frequency plane which reveals many similarities with the Dicke super/sub radiance transition [19]. We can turn these exponentially localized modes to BIC modes by adding a uniform loss (for gain defect) or gain (for lossy defect) in the array, thus realizing BIC states in a simple non-Hermitian set-up.

2. MODEL

We consider a one-dimensional array of $N = 2M + 1$ weakly coupled single-mode optical waveguides. The light propagation along the z-axis is described by the standard coupled mode equations [20]

$$i\lambda \frac{\partial \bar{\psi_n}(z)}{\partial z} + V\left(\psi_{n+1}(z) + \psi_{n-1}(z)\right) + \epsilon_n \psi_n(z) = 0 \tag{2}$$

where $n = -M, \cdots, M$ is the waveguide number, $\psi_n(z)$ is the amplitude of the optical field envelope at distance z in the n-th waveguide, V is the coupling constant between nearby waveguides and $\lambda\ bar \equiv \lambda/2\pi$ where λ is the optical wavelength in vacuum. The refractive index ϵ_n satisfies the relation $\epsilon_n = \epsilon_0^{(R)} + i\epsilon_n^{(I)}\delta_{n,0}$ where we have assumed that a defect in the imaginary part of the dielectric constant is placed in the middle of the array at waveguide $n = 0$. Below, without loss of generality, we will set $\epsilon_0^{(R)} = 0$ for all waveguides. Our results apply for both gain $\epsilon_0^{(I)} < 0$ and lossy $\epsilon_0^{(I)} > 0$ defects.

Substitution in Eq. (2) of the form $\psi_n(z) = \phi_n^{(k)} \exp(-i\beta^{(k)} z/\lambda)$, where the propagation constant $\beta^{(k)}$ can be complex, leads to the Floquet-Bloch (FB) [21] eigenvalue problem

$$\beta^{(k)}\phi_n^{(k)} = -V(\phi_{n+1}^{(k)} + \phi_{n-1}^{(k)}) - \epsilon_n \phi_n^{(k)}; \quad k = 1, \cdots, N \tag{3}$$

We want to investigate the changes in the structure of the FB modes and the parametric evolution of $\beta^{(k)}$ as the imaginary part of the optical potential $\epsilon_0^{(I)}$ increases.

Before we begin the analysis of the model, we would like to comment on the possibility of realizing such system in an experiment. First, due to the Kramers-Kronig relations the real and imaginary part of the dielectric constant are not independent of each other; nevertheless it is possible to have the same $\epsilon_0^{(R)}$ for the defect waveguide as well by compensating for the changes in the $\epsilon_0^{(R)}$ at $n = 0$ by adjusting, for example, the width of this waveguide. Secondly, optical losses can be incorporated experimentally by depositing a thin film of absorbing material on top of the waveguide [22], or by introducing scattering loss in the waveguides [23]. Optical amplification can be introduced by stimulated emission in gain material or parametric conversion in nonlinear material [24].

3. THRESHOLD BEHAVIOR

We begin by analyzing the parametric evolution of $\beta^{(k)}$'s as a function of the non-Hermiticity parameter $\epsilon_0^{(I)}$. We decompose the Hamiltonian H_{nm} of Eq. (3) into a Hermitian part $(H_0)_{nm} = -V\delta_{n,m+1} - V\delta_{n,m-1}$ and a non-Hermitian part $\Gamma_{nm} = -i\epsilon_n^{(I)}\delta_{n,0}\delta_{n,m}$ i.e. $H = H_0 + \Gamma$. For $\epsilon_0^{(I)} = 0$ the eigenvalues and eigenvectors of $H = H_0$ are $\beta^{(k)} = -2V\cos(k\pi/(N+1))$ and $\phi_n^{(k)} = \sqrt{2/(N+1)}\sin[k\,(n\pi/(N+1) + \pi/2)]$. In the limit $N \to \infty$ the spectrum is continuous creating a band $\beta \in [-2V, 2V]$ that supports radiating states.

As $\epsilon_0^{(I)}$ increases from zero the propagation constants move into the complex plane. Using, for small values of $\epsilon_0^{(I)}$, first order perturbation theory we get that $\beta^{(k)} \approx \beta_0^{(k)} + \Gamma_{k,k}$ where $\Gamma_{k,k} \approx -i\epsilon_0^{(I)}/(N+1)$. When the matrix elements of the non-Hermitian part of

H become comparable with the mean level spacing $\Delta = 2V/N$ of the eigenvalues of the Hermitian part H_0, the perturbation theory breaks down. This happens when $|\epsilon_{cr}^{(I)}|/(N+1) \sim \Delta$ which leads to the estimation $|\epsilon_{cr}^{(I)}| \sim 2V$. In the opposite limit of large $|\epsilon_0^{(I)}|$, H_0 can be treated as a perturbation to Γ. Due to its specific form, the non-Hermitian matrix Γ has only one nonzero eigenvalue and thus, in the large $|\epsilon_0^{(I)}|$ limit, there is only one complex propagation constant corresponding to $\mathcal{R}e\left[\beta_0^{(k=(N+1)/2)}\right] = 0$, while all other modes will have zero imaginary component (to first order). The above considerations allow us to conclude that for $|\epsilon_0^{(I)}| \gg 2V$ a segregation of propagation constants in the complex plane occurs: Below this point all β's get an imaginary part which increases in magnitude as $\sim -\epsilon_0^{(I)}/N$ while after that only one of them accumulates almost the whole imaginary part $\sim -\epsilon_0^{(I)}$ (independent of N) and the remaining $N-1$ approaches back to the real axis as $\sim -(2V)^2/(N\epsilon_0^{(I)})$. This segregation of propagating constants is the analogue of quantum optics Dicke super-radiance transition [25] which was observed also in other frameworks [14, 26–30]. These predictions are confirmed by our numerical data (see Figure 1).

4. THERMODYNAMIC LIMIT

In this section we investigate the structure of the FB modes of the system Eq. (3) in the thermodynamic limit (N$\rightarrow\infty$) as $\epsilon_0^{(I)}$ crosses the threshold $\epsilon_{cr}^{(I)}$. In the case of real defect, an infinitesimal value of it will lead to the creation of a localized mode (with a real-valued β_{def} outside of the interval $[-2V, 2V]$) [31]. We want to find out if the same scenario is applicable in the case of imaginary defect. To this end we introduce the ansatz:

$$\phi_n = \begin{cases} A^{(+)} \exp(-n\Lambda) & \text{for} \quad n \geq 0 \\ A^{(-)} \exp(n\Lambda) & \text{for} \quad n \leq 0 \end{cases} \tag{4}$$

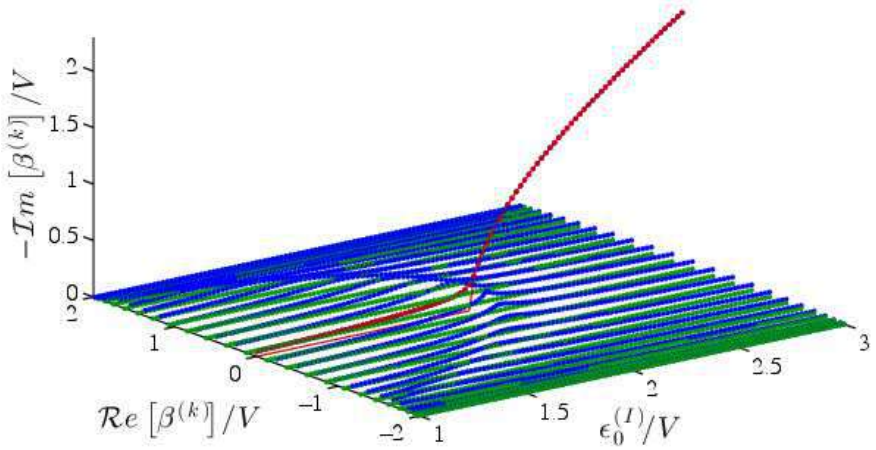

Figure 1. Parametric evolution of the propagation constants $\beta^{(k)}$ of an array of $N = 49$ coupled waveguides with one dissipative ($\epsilon_0^{(I)} > 0$) defect in the middle, as a function of $\epsilon_0^{(I)}$. The phase transition occurs at $\epsilon_0^{(I)} = \epsilon_{cr}^{(I)} \equiv +2V$ where the defect mode profile (shown as red dots) switches from non-exponential to exponential decay. Solid red line shows the asymptotic analytical result Eq. (5). Similar behavior (not shown here) but with the β's in the upper complex plane can be observed for gain $\epsilon_0^{(I)} < 0$ where $\epsilon_{cr}^{(I)} = -2V$. The green lines indicate modes with real propagation constants which are solutions of the first Eq. (11). In the case of even number N they also acquire an imaginary part in the propagation constant, similar to the modes shown in blue.

Continuity requirement of the FB mode at $n = 0$ leads to $A^{(+)} = A^{(-)}$. Furthermore, substituting the above ansatz in Eq. (3) for $n = 0$ and $n = 1$ and after some straightforward algebra we get that

$$\beta_{\text{def}} = -s\sqrt{4V^2 - (\epsilon_0^{(I)})^2}; \quad \Lambda = -\ln\left(\frac{-\beta_{\text{def}} - i\epsilon_0^{(I)}}{2V}\right), \tag{5}$$

where $s \equiv \epsilon_0^{(I)}/|\epsilon_0^{(I)}|$ denotes the sign of the defect. From Eq. (5) we find that for $|\epsilon_0^{(I)}| < |\epsilon_{cr}^{(I)}| \equiv 2V$ the corresponding propagation constant is real while the decay rate is $\Lambda = -i \arctan\left(\epsilon_0^{(I)}/\beta_{\text{def}}\right)$ i.e. a simple phase. In other words the FB modes are extended. In the opposite limit of $|\epsilon_0^{(I)}| > |\epsilon_{cr}^{(I)}|$ the propagation constant becomes complex and the

corresponding Λ takes the form

$$\Lambda = \ln\left(\frac{2V}{\left|\epsilon_0^{(I)}\right| - \sqrt{(\epsilon_0^{(I)})^2 - 4V^2}}\right) + i\, s\, \frac{\pi}{2} \tag{6}$$

The corresponding inverse localization length is then defined as $\xi^{-1} \equiv \mathcal{R}e(\Lambda)$ indicating the existence of exponential localization. Therefore we find that a non-Hermitian defect - in contrast to a Hermitian one (see for example [31])- induces a localization-delocalization transition at the phase transition points $\epsilon_{cr}^{(I)} = s \times 2V$. We emphasize again that this phase transition and the creation of a localized mode occur for both signs of the non-Hermitian defect and can be induced for both lossy ($\epsilon_0^{(I)} > 0$) and gain ($\epsilon_0^{(I)} < 0$) defect.

In Figure 2 we report the FB defect mode of our system Eq. (3) for three cases (a) $0 < \epsilon_0 < 2V$, (b) $\epsilon_0 = 2V$ and (c) $\epsilon_0 > 2V$, and different system sizes. Note that although in the latter case the mode is localized in space, it is not qualified as a BIC since the corresponding propagation constant β_{def} (see Eq. (5)) is imaginary and therefore the mode is non-stationary. Adding, however, a uniform gain (for lossy defect) β_{def} or loss (for gain defect) $-\beta_{\text{def}}$ to the array can turn this state to a BIC with zero imaginary propagation constant. The latter case is experimentally more tractable since adding a global loss will lead to a decay of all other modes while the localized defect mode would be stable having a constant amplitude.

5. PROPERTIES OF THE CRITICAL STATE

The existence of the delocalization-localization phase transition posses intriguing questions, one of which is the nature of the FB mode at the transition point associated with $\epsilon_{cr}^{(I)}$. In particular, it is known from the Anderson localization theory, that the eigenfunctions at the metal-to-insulator phase transition are multifractals i.e. display strong fluctuations on all length scales [32–41]. Their structure is quantified by analyzing the dependence of

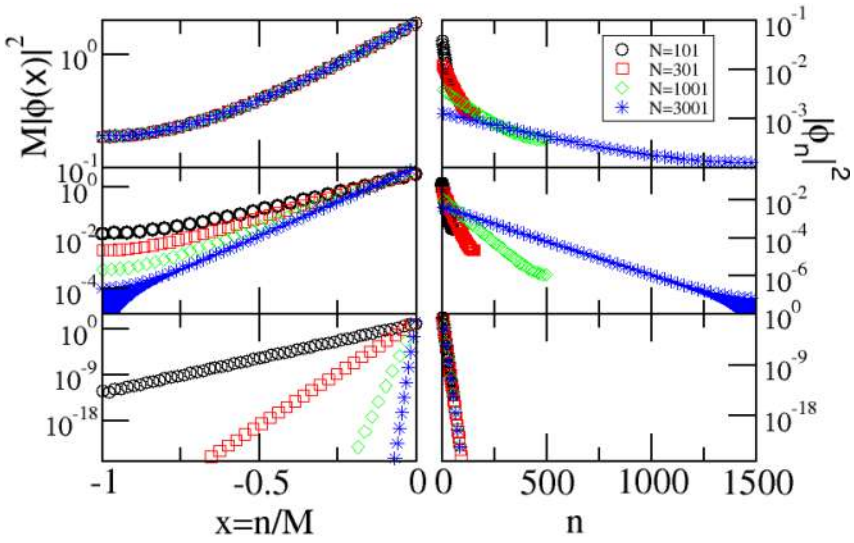

Figure 2. FB defect mode for various system sizes $N = 2M + 1$. Left panels report the left part ($n < 0$) of these modes (the right part $n > 0$ is the same) by employing the scaling $M\phi(x = n/M)$ while the right panels report the right part $n > 0$ of these modes without any scaling. In the former representation an extended state is invariant under increase of the size of the system while in the latter, the scale invariance is demonstrated for localized modes. Three defect values of $\epsilon_0^{(I)}$ has been used: (upper) $0 < \epsilon_0^{(I)} = 1.9V < 2V$ where the mode is delocalized; (middle) $\epsilon_0^{(I)} = 2V$ where the mode is critical; (lower) $\epsilon_0^{(I)} = 2.1V > 2V$ where the mode is exponentially localized.

their moments $\mathcal{I}_p$ with the system size N:

$$\mathcal{I}_p = \frac{\sum_n |\psi_n|^{2p}}{(\sum_n |\psi_n|^2)^2} \propto N^{-(p-1)D_p}. \tag{7}$$

Above the multifractal dimensions $D_p \neq 0$ are different from the dimensionality of the embedded space d. Among all moments, the so-called inverse participation number (IPN) $\mathcal{I}_2$ plays the most prominent role. It can be shown that it is roughly equal to the inverse number of non-zero eigenfunction components, and therefore it is a widely accepted measure to characterize the extension of a state. We will concentrate our analysis on $\mathcal{I}_2$ of the FB mode at the phase transition point $\epsilon_{cr}^{(I)}$.

We assume that the eigenmodes of Eq. (3) take the form:

$$\phi_n^{(k)} = A^{(\mp)} e^{iq^{(k)}n} + B^{(\mp)} e^{-iq^{(k)}n} (n < 0/n > 0) \tag{8}$$

where $q^{(k)} = q_r^{(k)} + iq_i^{(k)}$, while the associated propagation constants are written in the form $\beta^{(k)} \equiv -2V\cos(q^{(k)}) = \beta_r^{(k)} + i\beta_i^{(k)}$. Imposing hard wall boundary conditions $\phi_{M+1} = \phi_{-M-1} = 0$ to the solutions Eq. (8) leads to:

$$B^{(\mp)} = -A^{(\mp)} e^{\mp 2iq(M+1)} \tag{9}$$

The requirement for continuity of the wavefunction at $n = 0$ lead us to the relation

$$A^{(+)} + B^{(+)} = A^{(-)} + B^{(-)} \tag{10}$$

Substitution of Eqs. (9,10) back into Eq. (3) for $n = 0$, lead to the transcendental equations for q:

$$\sin[(M+1)q] = 0; \text{ or } \cot[(M+1)q]\sin(q) = i\frac{\epsilon_0^{(I)}}{2V} \tag{11}$$

We are interested in the structure of the FB mode in the middle of the band corresponding to $\mathcal{R}e(\beta) = 0$. For simplicity of the calculations we assume below that $M+1$ is odd and also remind that the total size of the system is $N = 2M+1$. Imposing the condition $\mathcal{R}e(\beta) = 0$ in the second term of the Eq. (11) we get that $q_r = -s\pi/2$ while the imaginary part q_i satisfies the equation

$$s\tanh\left[(M+1)q_i\right]\cosh(q_i) = \frac{\epsilon_0^{(I)}}{2V} \tag{12}$$

We will look for a stationary solution at the phase transition point $\epsilon_0^{(I)} = s\,2V$ with $\beta_i \to 0$ (or equivalently $q_i \to 0$) in $N \to \infty$ limit that also satisfies $q_i \times (M+1) \sim q_i N \to \infty$ condition. In Eq. (12) we now perform small q_i expansion in $\cosh(q_i) \approx 1 + q_i^2/2$ and large $(M+1)q_i$ expansion in $\tanh[(M+1)q_i] = \frac{\exp((M+1)q_i) - \exp(-(M+1)q_i)}{\exp((M+1)q_i) + \exp(-(M+1)q_i)} \approx 1 - 2\exp(-(N+1)q_i) \approx 1 - q_i^2/2$.

In the large M-limit the solution of the last transcendental equation is

$$q_i \sim 2\frac{\ln(N+1)}{N+1} \tag{13}$$

Substituting back to the expression for the propagation constant we get $\beta = -2V\cos(-s\pi/2 + iq_i) \approx -s\,2V\,iq_i$ which in the large $N(M)$-limit results in $\beta = 0$. Finally, substituting Eqs. (9,13) back to Eq. (8) we get that

$$\phi_n \propto \exp\left[i(-s\pi/2 + iq_i)|n|\right] = \frac{(-s\,i)^{|n|}}{(N+1)^{2|n|/(N+1)}} \tag{14}$$

The FB state described by Eq. (14) is not exponentially localized neither it is extended. It rather falls to an exotic family of critical states and it can quantify better via the IPN $\mathcal{I}_2$. Using Eq. (7) for $p = 2$ it is easy to show that the IPN of the FB mode of Eq. (14) is given by Eq. (1). Furthermore, this scaling relation is not consistent with the standard power law Eq. (7) characterizing self-similar (fractal) states. Rather we have an unusual situation of *a critical state that it is at the verge of being fractal*. To our knowledge such anomalous scaling has been discussed only in completely different context of Hermitian random matrix models [42] or modulated (graded)systems [43, 44] and were never found to be present in any physical system. Thus our simple set-up constitutes the first paradigmatic system where these CSC can be observed. In Figure 3 we report the scaling of $\mathcal{I}_2$ versus the system size at the phase transition point $\epsilon_{cr}^{(I)} = 2V$ as found by solving Eq. (3) numerically. We see that the data follow nicely the prediction of Eq. (1). We conclude this section by noting that for odd N considered above, some of the FB modes can have (due to symmetry) a nodal point at the center of the array where the non-Hermitian defect is placed, see green symbols in Figure 1. Therefore they do not overlap with the defect and thus have real propagation constants. The latter are solutions of the first Eq. (11). In the case of even N, all modes of the system are calculated by an equation similar to the second Eq. (11) and thus they all have imaginary propagation constant. This is due to the fact that they have an appreciable

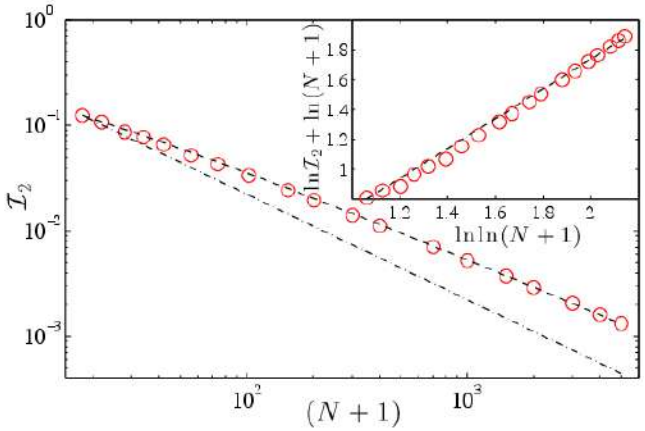

Figure 3. Scaling analysis of $\mathcal{I}_2$ (shown as symbols) of a CSC state versus the system size N. Dot-dashed line corresponds to N^{-1} dependence. Dashed line is prediction of Eq. (1) which contains a logarithmic correction. In the inset we plot the same data in a different fashion i.e. $\ln \mathcal{I}_2 + \ln(N+1)$ versus $\ln\ln(N+1)$. Straight line with a unit slope confirms the existence of the logarithmic dependence as indicated by Eq. (1).

component at the middle of the array where the non-Hermitian defect is placed. The rest of the analysis associated with the CSC remains qualitatively the same. We also repeated our calculation for the periodic boundary conditions to confirm that the scaling properties the critical state remain unchanged in the $N \to \infty$ limit.

6. PERIODIC PERTURBATION

In this section we demonstrate that the critical nature of the defect state is not a consequence of the degenerate band-edge [45] being present in the case of the tight-binding system of Eq. (3). This can be achieved by introducing an on-site potential $\epsilon_n^{(R)} = \epsilon_0^{(R)}(-1)^n$ which removes the degeneracy at $\beta = 0$. Therefore, the new tight-binding equation is:

$$\beta^{(k)}\phi_n^{(k)} = -V(\phi_{n+1}^{(k)} + \phi_{n-1}^{(k)}) - (\epsilon_0^{(R)}(-1)^n + i\epsilon_n^{(I)}\delta_{n0})\phi_n^{(k)} \tag{15}$$

We propose the following ansatz for odd/even (denoted by superscript o/e) waveguide numbers:

$$\phi_n^{(k)(o/e)} = A^{(-)(o/e)} e^{iq^{(k)}n} + B^{(-)(o/e)} e^{-iq^{(k)}n} (n < 0)$$
$$\phi_n^{(k)(o/e)} = A^{(+)(o/e)} e^{iq^{(k)}n} + B^{(+)(o/e)} e^{-iq^{(k)}n} (n > 0) \quad (16)$$

In the absence of imaginary defects we get the following dispersion relation:

$$\beta^{(k)} = (-1)^b \sqrt{(\epsilon_0^{(R)})^2 + 4V^2 \cos^2 q^{(k)}}, \quad (17)$$

where b is the band index. $b = 1$ for $\mathcal{R}e[\beta] < 0$ and $b = 2$ for $\mathcal{R}e[\beta] > 0$. Therefore, the degenerate energy at zero is shifted into the positive or negative branch.

In the presence of defect, and after taking into account the hard wall boundary conditions ($\phi_{M+1}^{(k)(o)} = \phi_{-M-1}^{(k)(o)} = 0$) and continuity at n=0, we get two discrete equations for the complex propagation constant q:

$$\sin[(M+1)q] = 0; \text{ or}$$
$$\cot[(M+1)q] \sin(q) = \frac{i\epsilon_0^{(I)}}{2V} . \frac{\epsilon_0^{(R)} + (-1)^b \sqrt{(\epsilon_0^{(R)})^2 + 4V^2 \cos^2 q}}{2V \cos q} \quad (18)$$

The above equations are consistent with the results presented in the previous section at the limit $\epsilon_0^{(R)} \to 0$. In the localized regime ($|\epsilon_0^{(I)}| > |\epsilon_{cr}^{(I)}|$), we get $\cot[(M+1)q] \approx i$. By replacing this expression into the second term of Eq. (18), we derive the following cubic relation for $x \equiv \tan q$:

$$2\epsilon_0^{(R)} \epsilon_0^{(I)} x^3 + \left((\epsilon_0^{(I)})^2 - 4V^2\right) x^2 + 2\epsilon_0^{(R)} \epsilon_0^{(I)} x + (\epsilon_0^{(I)})^2 = 0 \quad (19)$$

The above algebraic equation has three roots. Depending on the value of $\epsilon_0^{(I)}$ these roots can be either real or complex. In the former case (i.e. x, and therefore q, being real) the associated mode is extended, while in the latter one (i.e. x, and therefore q, being complex) the associated mode is localized. The transition between these types of modes occurs at $\epsilon_{cr}^{(I)}$

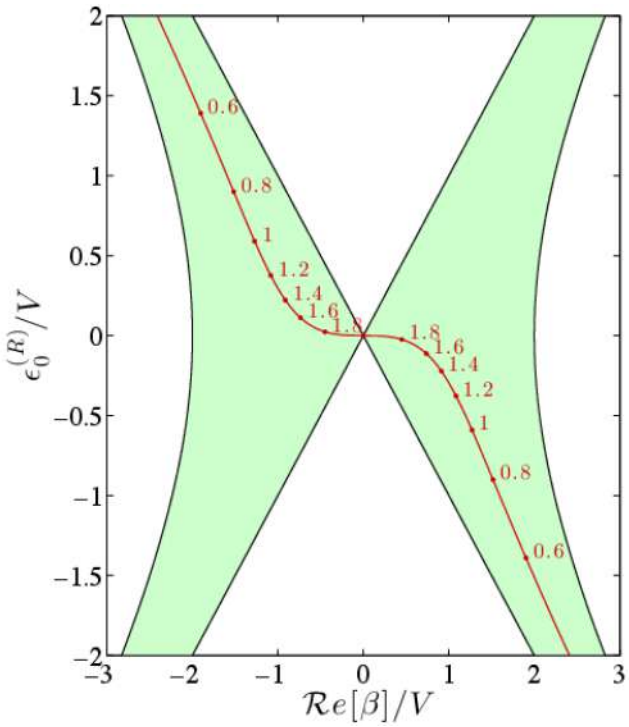

Figure 4. Band structure (green shadowed array) of the model Eq. (15) vs. $\epsilon_0^{(R)}$. The red line indicates the trajectory of the defect eigenmode as $\epsilon_0^{(R)}$ increases. The red dots and the associated numbers are indicative values of the critical $|\epsilon_0^{(I)}|$ (for the specific $\epsilon_0^{(R)}$) above which a defect mode is created.

and is given as a solution of the following equation:

$$\left((4V^2 - \epsilon_{cr}^{(I)})^2\right)^3 = 8(\epsilon_0^{(R)})^2\Big(- 2V^4 + 10V^2(\epsilon_{cr}^{(I)})^2 + (\epsilon_{cr}^{(I)})^4 + 2(\epsilon_{cr}^{(I)})^2(\epsilon_0^{(R)})^2\Big) \tag{20}$$

Furthermore, it can readily be confirmed that, as expected, for $\epsilon_0^{(R)} \to 0$, $\epsilon_{cr}^{(I)}$ approaches to 2.

The associated energy β_{cr} of the defect (localized) mode is found after substituting the expression for $\epsilon_{cr}^{(I)}$ from Eq. (20), into Eq. (18). This allows us to evaluate $q^{(cr)}$ which can then be substituted in Eq. (17) in order to get an expression for β_{cr}. The obtained

dependence of $\mathcal{R}e[\beta_{cr}]$ on $\epsilon_0^{(R)}$ is shown in Figure 4 with red line. The values of $\mathcal{I}m[\beta_{cr}]$ are denoted with dots and numbers. We note that the real part of the propagation constant $\mathcal{R}e[\beta_{cr}]$ is insensitive to the sign of $\epsilon_0^{(I)}$.

Next, we investigate the scaling behavior of the defect mode at the transition point $\epsilon_{cr}^{(I)}$. Following the same argumentation as used in the previous section, we write $q^{(cr)}$ as $q_r^{(cr)} + iq_i$, where we assume that $(M+1)q_i \to \infty$ and q_i is a small quantity. Substituting back to the transcendental equality of Eq. (18) and expanding each term up to first order in q_i we eventually get:

$$q_i \sim \frac{\ln(N+1)}{N+1}. \tag{21}$$

Considering the fact that $\mathcal{I}_2 \sim q_i$, it can be deduced that the second moment of the defect mode for the modified model scales anomalously as indicated in Eq. (1) of the main text. Hence, we conclude that the logarithmic scaling of IPR is not a consequence of degenerate band-edge in Anderson model at $\beta = 0$.

7. CONCLUSIONS

In conclusion we have investigated the structure of non-Hermitian defect states as a function of the defect strength. We have found that these states experienced a phase transition from delocalization to localization as the imaginary part of the refractive index in the defect waveguide approaches a critical value. At the transition point the inverse participation number of this mode scales as $\ln(N)/N$ indicating a weak criticality. This phase transition is accompanied by a mode re-organization which reveals analogies with the Dicke super-radiance. The transition survives periodic perturbations in the refractive index in the waveguide array and the anomalous logarithmic behavior of the inverse participation ratio at the critical point is preserved. It will be interesting to investigate whether this behavior survives in higher dimensions and other type of configurations including disordered [46–48] and continuous [49, 50] models.

ACKNOWLEDGMENTS

We thank A. Ossipov and Y. Fyodorov for useful discussions. This work was sponsored partly by grants NSF ECCS-1128571, DMR-1205223, ECCS-1128542 and DMR-1205307 and by an AFOSR MURI grant FA9550-14-1-0037.

REFERENCES

[1] A. Peres. *Quantum Theory: Concepts and Methods*. Fundamental Theories of Physics. Springer Netherlands, 1995.

[2] N.F. Mott. Electrons in disordered structures. *Advances in Physics*, 16(61):49–144, 1967.

[3] J. Von Neumann and 465 (1929) E. Wigner, Phys. Z. 30. About strange discrete eigenvalues. *Phys. Z.*, 30:465, 1929.

[4] Y. Plotnik, F. Dreisow, M. Heinrich, S. Nolte, A. Szameit, and M. Segev. Experimental observation of optical bound states in the continuum. *Phys. Rev. Lett.*, 107:183901–183904, 2011.

[5] S. Weimann, Y. Xu, R. Keil, A.E. Miroshnichenko, A. Tünnermann, S. Nolte, A. A. Sukhorukov, A. Szameit, and Y. S. Kivshar. Compact surface fano states embedded in the continuum of waveguide arrays. *Phys. Rev. Lett.*, 111:240403–240407, 2013.

[6] G. Corrielli, G. Della Valle, A. Crespi, R. Osellame, and S. Longhi. Observation of surface states with algebraic localization. *Phys. Rev. Lett.*, 111:220403–220407, 2013.

[7] C.W. Hsu, B. Zhen, J. Lee, S.L. Chua, S. G. Johnson, J.D. Joannopoulos, and M. Soljacic. Observation of trapped light within the radiation continuum. *Nature*, 499:188–191, 2013.

[8] R. Porter and D.V. Evans. Embedded rayleigh-bloch surface waves along periodic rectangular arrays. *Wave Motion*, 43(1):29–50, 2005.

[9] C.M. Linton and P. McIver. Embedded trapped modes in water waves and acoustics. *Wave Motion*, 45(1):16–29, 2007.

[10] F. Capasso, C. Sirtori, J. Faist, D.L. Sivco, S.N.G. Chu, and A. Y. Cho. Observation of an electronic bound state above a potential well. *Nature*, 358:565–567, 1992.

[11] D. C. Marinica, A. G. Borisov, and S. V. Shabanov. Bound states in the continuum in photonics. *Phys. Rev. Lett.*, 100:183902, May 2008.

[12] K. Yagasaki, A. R. Champneys, and B. A. Malomed. Discrete embedded solitons. *Nonlinearity*, 18(6):2591, 2005.

[13] S. GonzÃąlez-PÃĺrez-Sandi, J. Fujioka, and B.A. Malomed. Embedded solitons in dynamical lattices. *Physica D: Nonlinear Phenomena*, 197(1):86 – 100, 2004.

[14] J. OkoÅĆowicz, M. PÅĆoszajczak, and I. Rotter. Dynamics of quantum systems embedded in a continuum. *Physics Reports*, 374(4):271 – 383, 2003.

[15] K. Zhou, Z. Guo, J. Wang, and S. Liu. Defect modes in defective parity-time symmetric periodic complex potentials. *Opt. Lett.*, 35(17):2928–2930, 2010.

[16] A. Regensburger, M. A. Miri, C. Bersch, J. Näger, G. Onishchukov, D. N. Christodoulides, and U. Peschel. Observation of defect states in $\mathcal{PT}$-symmetric optical lattices. *Phys. Rev. Lett.*, 110:223902, 2013.

[17] S. Longhi. Bound states in the continuum in pt-symmetric optical lattices. *Opt. Lett.*, 39(6):1697–1700, 2014.

[18] M. I. Molina and Y. S. Kivshar. Embedded States in the Continuum for -Symmetric Systems. *Studies in Applied Mathematics*, 133(3):337–350, 2014.

[19] G. Luca Celardo, Giulio G. Giusteri, and Fausto Borgonovi. Cooperative robustness to static disorder: Superradiance and localization in a nanoscale ring to model light-harvesting systems found in nature. *Phys. Rev. B*, 90:075113–075122, 2014.

[20] D. N. Christodoulides, F. Lederer, and Y. Silberberg. Discretizing light behaviour in linear and nonlinear waveguide lattices. *Nature*, 424:817–823, 2003.

[21] P. St. J. Russell. Optics of floquet-bloch waves in dielectric gratings. *Applied Physics B*, 39(4):231–246, 1986.

[22] A. Guo, G. J. Salamo, D. Duchesne, R. Morandotti, M. Volatier-Ravat, V. Aimez, G. A. Siviloglou, and D. N. Christodoulides. Observation of $\mathcal{PT}$-symmetry breaking in complex optical potentials. *Phys. Rev. Lett.*, 103:093902–093905, 2009.

[23] T. Eichelkraut, R. Heilmann, S. Weimann, S. Stützer, F. Dreisow, D. N. Christodoulides, S. Nolte, and A. Szameit. Mobility transition from ballistic to diffusive transport in non-hermitian lattices. *Nature Communications*, 4:25331–25337, 2013.

[24] C. E. Rüter, K. G. Makris, R. El-Ganainy, D. N. Christodoulides, M. Segev, and D. Kip. Observation of parity-time symmetry in optics. *Nature Physics*, 6:192–195, 2010.

[25] R. H. Dicke. Coherence in spontaneous radiation processes. *Phys. Rev.*, 93:99–110, 1954.

[26] V. V. Sokolov and V. G. Zelevinsky. Dynamics and statistics of unstable quantum states. *Nuclear Physics A*, 504(3):562 – 588, 1989.

[27] G. L. Celardo, F. Borgonovi, M. Merkli, V. I. Tsifrinovich, and G. P. Berman. Superradiance transition in photosynthetic light-harvesting complexes. *The Journal of Physical Chemistry C*, 116(42):22105–22111, 2012.

[28] R. Monshouwer, M. Abrahamsson, F. van Mourik, and R. van Grondelle. Superradiance and exciton delocalization in bacterial photosynthetic light-harvesting systems. *The Journal of Physical Chemistry B*, 101(37):7241–7248, 1997.

[29] J. Keaveney, A. Sargsyan, U. Krohn, I. G. Hughes, D. Sarkisyan, and C. S. Adams. Cooperative lamb shift in an atomic vapor layer of nanometer thickness. *Phys. Rev. Lett.*, 108:173601–173605, 2012.

[30] M. O. Scully and A. A. Svidzinsky. The lamb shift-yesterday, today, and tomorrow. *Science*, 328(5983):1239–1241, 2010.

[31] E.N. Economou. *Green's Functions in Quantum Physics*. Springer Series in Solid-State Sciences. Springer, 2006.

[32] A. D. Mirlin. Statistics of energy levels and eigenfunctions in disordered systems. *Physics Reports*, 326(5):259 – 382, 2000.

[33] Y. V. Fyodorov and A. D. Mirlin. Statistical properties of eigenfunctions of random quasi 1d one-particle hamiltonians. *International Journal of Modern Physics B*, 8(27):3795–3842, 1994.

[34] Y.V. Fyodorov and A. D. Mirlin. Mesoscopic fluctuations of eigenfunctions and level-velocity distribution in disordered metals. *Phys. Rev. B*, 51:13403–13409, 1995.

[35] V. I. Fal'ko and K. B. Efetov. Multifractality: Generic property of eigenstates of 2d disordered metals. *EPL (Europhysics Letters)*, 32(8):627, 1995.

[36] V. I. Fal'ko and K. B. Efetov. Statistics of prelocalized states in disordered conductors. *Phys. Rev. B*, 52:17413–17429, Dec 1995.

[37] F. Wegner. Inverse participation ratio in 2+ ε dimensions. *Zeitschrift für Physik B Condensed Matter*, 36(3):209–214, 1980.

[38] H. Aoki. Critical behaviour of extended states in disordered systems. *Journal of Physics C: Solid State Physics*, 16(6):L205–L208, 1983.

[39] M. Schreiber and H. Grussbach. Multifractal wave functions at the anderson transition. *Phys. Rev. Lett.*, 67:607–610, 1991.

[40] D. A. Parshin and H. R. Schober. Distribution of fractal dimensions at the anderson transition. *Phys. Rev. Lett.*, 83:4590–4593, 1999.

[41] A. Mildenberger, F. Evers, and A. D. Mirlin. Dimensionality dependence of the wave-function statistics at the anderson transition. *Phys. Rev. B*, 66:033109–033112, Jul 2002.

[42] A. Ossipov, I. Rushkin, and E. Cuevas. Criticality without self-similarity: a 2d system with random long-range hopping. *Journal of Physics: Condensed Matter*, 23(41):415601, 2011.

[43] M. Zheng, M. Goda, K. Yakubo, and K. W. Yu. Anomalous size dependence of inverse participation ratio of eigenfunctions in graded elastic lattices. *Journal of the Physical Society of Japan*, 77(9):094601, 2008.

[44] K. Yakubo, J. J. Xiao, and K. W. Yu. Localized vibrations in graded lattices: Gradons. *Journal of Physics: Conference Series*, 92(1):012008, 2007.

[45] L. I. Deych, M. V. Erementchouk, A. A. Lisyansky, and B. L. Altshuler. Scaling and the center-of-band anomaly in a one-dimensional anderson model with diagonal disorder. *Phys. Rev. Lett.*, 91:096601–096604, 2003.

[46] P. E. Parris. One-dimensional trapping kinetics at zero temperature. *Phys. Rev. Lett.*, 62:1392–1395, 1989.

[47] A. Ziletti, F. Borgonovi, G. L. Celardo, F. M. Izrailev, L. Kaplan, and V. G. Zelevinsky. Coherent transport in multibranch quantum circuits. *Phys. Rev. B*, 85:052201–052205, 2012.

[48] A. Basiri, Y. Bromberg, A. Yamilov, H. Cao, and T. Kottos. Light localization induced by a random imaginary refractive index. *Phys. Rev. A*, 90:043815–043821, 2014.

[49] J. D. Joannopoulos, S. G. Johnson, J. N. Winn, and R. D. Meade. *Photonic crystals: molding the flow of light*. Princeton university press, 2011.

[50] A. Figotin and V. Gorentsveig. Localized electromagnetic waves in a layered periodic dielectric medium with a defect. *Phys. Rev. B*, 58:180–188, 1998.

SECTION

2. SUMMARY AND CONCLUSIONS

2.1. ANALYSIS OF CORRELATION FUNCTION AND TRANSMISSION EIGENCHANNELS INSIDE RANDOM MEDIA

The first portion of the dissertation described the interference effects in wave propagation in random media. Wave-based models were studied in $1D$, $2D$, Quasi-$1d$, and $3D$ geometries to explore such effects.

The diffusion model is an extremely useful model used to describe typical wave propagation [1, 5, 61, 62]. Interference effects such as universal conductance fluctuations, Anderson localization corrections, enhanced backscattering, and nonlocal mesoscopic correlations [7, 63–65] can't be explained by the diffusion model. These phenomena are general and occur not only for electromagnetic waves, but also for acoustic, electronic, and other kinds of waves [6, 7]. Two very interesting phenomena that originate in interference effects are intensity-intensity correlation function and transmission channels. In this thesis, we proposed analytical models to predict the behavior of these two quantities in random media of different geometries.

We also proposed a way to detect a diffusive cloak [66] using the long-range correlation function. When waves undergo multiple scattering events inside random media, wave path crossing may occur due to the complicated propagation via a random walk-like process. This wave crossing inside gives rise to the correlation. The correlation function can be decomposed into its components depending on number of path crossings. The long-range intensity correlation (C_2) is very sensitive to location of path crossing, allowing one to detect the size and position, including the depth, of the diffusive cloak. We proposed

a novel theoretical idea to detect diffusive cloak embedded inside random media. Our work also offers a possibility to manipulate correlations and fluctuations. We also show that diffusive-light invisibility cloaks can work well under stationary conditions in the limits of very small and very large coherence lengths of light. But they can be uncloaked for the intermediate case of illumination with partially coherent light and inspection of the resulting speckle contrast (C_1).

Another important phenomenon that stems from the interference effect is the existence of eigenchanels, first predicted by Dorokhov [29] in 1984. Indeed, there exist system-specific incident wavefronts, which couple light into perfectly transmitted eigenchannels (PTE). Such an excitation allows light propagation through scattering media with near unity transmittance [40, 49, 53, 67–69]. In this thesis, we develop a theoretical model to predict the spatial structure of the perfectly transmitting eigenchannels in the regime of diffusive transport. We employ a projection technique [33] to obtain an analytical relation between the depth profile of the perfectly transmitting eigenchannel and the geometry of the waveguide. We further propose inverse design to manipulate the shape of the waveguide to achieve the desired energy distribution for the perfectly transmitting eigenchannel.

2.2. ANALYSIS OF BOUND STATE IN CONTINUUM

Lastly, we introduce a previously unnoticed class of critical states, which are embedded in the continuum. We demonstrate their existence using a simple setup consisting of N coupled optical waveguides with one non- Hermitian (with loss or gain) defective waveguide in the middle. Similarly to the well-known bound in the continuum (BIC) states, they have real propagation constants, however, their envelope resembles a fractal structure. These states experienced a phase transition from delocalization to localization as the imaginary part of the refractive index in the defect waveguide approaches a critical value. At the transition point, the inverse participation number of this mode scales as $\ln(N)/N$ indicating a weak criticality. We show that this phenomenon is a robust one, as

the transition is accompanied by a mode re-organization, which reveals analogies with the Dicke super-radiance. The transition survives periodic perturbations in the refractive index in the waveguide array, and the anomalous logarithmic behavior of the inverse participation ratio at the critical point is preserved.

REFERENCES

[1] A. Ishimaru. *Wave Propagation and Scattering in Random Media*. Academic Press, 1978.

[2] S. Chandrasekhar. *Radiative Transfer*. Dover publications, 1960.

[3] A. Einstein. *Investigations on the Theory of the Brownian Movement*. Courier Corporation, 1956.

[4] P. M. Morse and H. Feshbach. *Methods of theoretical physics*. Technology Press, 1946.

[5] M. C. W. van Rossum and Th. M. Nieuwenhuizen. Multiple scattering of classical waves: microscopy, mesoscopy, and diffusion. *Rev. Mod. Phys.*, 71:313–371, 1999.

[6] E. Akkermans and G. Montambaux. *Mesoscopic Physics of Electrons and Photons*. Cambridge University Press, Cambridge, 2007.

[7] Ad Lagendijk, B. van Tiggelen, and D. S. Wiersma. Fifty years of anderson localization. *Physics Today*, 62(8):24–29, 2009.

[8] Y. Imry. Active transmission channels and universal conductance fluctuations. *EPL (Europhysics Letters)*, 1(5):249, 1986.

[9] G. Maret and P. E. Wolf. Multiple light scattering from disordered media. the effect of brownian motion of scatterers. *Zeitschrift für Physik B Condensed Matter*, 65(4):409–413, 1987.

[10] A. Ishimaru. Wave propagation and scattering in random media and rough surfaces. *Proceedings of the IEEE*, 79(10):1359–1366, 1991.

[11] J. W. Goodman. *Speckle phenomena in optics: theory and applications*. s and Company Publishers, 2007.

[12] R. Berkovits and S. Feng. Correlations in coherent multiple scattering. *Physics Reports*, 238(3):135–172, 1994.

[13] B. Shapiro. Large intensity fluctuations for wave propagation in random media. *Phys. Rev. Lett.*, 57:2168–2171, 1986.

[14] S. Feng, C. Kane, P. A. Lee, and A. D. Stone. Correlations and fluctuations of coherent wave transmission through disordered media. *Phys. Rev. Lett.*, 61:834–837, 1988.

[15] M. P. van Albada, J. F. de Boer, and A. Lagendijk. Observation of long-range intensity correlation in the transport of coherent light through a random medium. *Phys. Rev. Lett.*, 64:2787–2790, 1990.

[16] I. Freund. Looking through walls and around corners. *Physica A: Statistical Mechanics and its Applications*, 168(1):49 – 65, 1990.

[17] Th.M Nieuwenhuizen and M.C.W van Rossum. RÃťle of a single scatterer in a multiple scattering medium. *Physics Letters A*, 177(1):102 – 106, 1993.

[18] M.J. Stephen and G. Cwilich. Intensity correlation functions and fluctuations in light scattered from a random medium. *Phys. Rev. Lett.*, 59:285–287, 1987.

[19] B.Z. Spivak and A.Yu. Zyuzin. Fluctuations of coherent light transmission through disordered media. *Solid State Communications*, 65(5):311 – 313, 1988.

[20] R. Pnini and B. Shapiro. Fluctuations in transmission of waves through disordered slabs. *Phys. Rev. B*, 39:6986–6994, 1989.

[21] J. F. de Boer, M. P. van Albada, and Ad. Lagendijk. Transmission and intensity correlations in wave propagation through random media. *Phys. Rev. B*, 45:658–666, 1992.

[22] M. Koirala, R. Sarma, H. Cao, and A. Yamilov. Inverse design of perfectly transmitting eigenchannels in scattering media. *Phys. Rev. B*, 96:0542091–0542096, 2017.

[23] A. Z. Genack, N. Garcia, and W. Polkosnik. Long-range intensity correlation in random media. *Phys. Rev. Lett.*, 65:2129–2132, 1990.

[24] N. Garcia, A.Z. Genack, R. Pnini, and B. Shapiro. Intensity correlation in waveguides. *Physics Letters A*, 176(6):458 – 461, 1993.

[25] C. P. Umbach, S. Washburn, R. B.Laibowitz, and R. A. Webb. Magnetoresistance of small, quasi-one-dimensional, normal-metal rings and lines. *Phys. Rev. B*, 30:4048–4051, 1984.

[26] P. A. Lee, D. A. Stone, and H. Fukuyama. Universal conductance fluctuations in metals: Effects of finite temperature, interactions, and magnetic field. *Phys. Rev. B*, 35:1039–1070, 1987.

[27] BL Altshuler. Fluctuations in the extrinsic conductivity of disordered conductors. *JETP lett*, 41(12):648–651, 1985.

[28] F. Scheffold and G. Maret. Universal conductance fluctuations of light. *Phys. Rev. Lett.*, 81:5800–5803, 1998.

[29] O.N. Dorokhov. On the coexistence of localized and extended electronic states in the metallic phase. *Solid State Communications*, 51(6):381 – 384, 1984.

[30] J.B. Pendry, A. MacKinnon, and A.B. Pretre. Maximal fluctuations âĂŤ a new phenomenon in disordered systems. *Physica A: Statistical Mechanics and its Applications*, 168(1):400–407, 1990.

[31] Yu. V. Nazarov. Limits of universality in disordered conductors. *Phys. Rev. Lett.*, 73:134–137, 1994.

[32] J. B. Pendry, A. MacKinnon, and P. J. Roberts. Universality classes and fluctuations in disordered systems. *Proceedings of the Royal Society of London A: Mathematical, Physical and Engineering Sciences*, 437(1899):67–83, 1992.

[33] P. S. Burada, P. Hanggi, F. Marchesoni, G. Schmid, and P. Talkner. Diffusion in confined geometries. *ChemPhysChem*, 10(1):45–54, 2009.

[34] M. Minsky. Microscopy apparatus us patent 3013467. *USP Office, Ed. US*, 1961.

[35] P. J. Keller, A. D. Schmidt, J. Wittbrodt, and E. H. K. Stelzer. Reconstruction of zebrafish early embryonic development by scanned light sheet microscopy. *Science*, 322(5904):1065–1069, 2008.

[36] J. Mertz. Optical sectioning microscopy with planar or structured illumination. *Nature Methods*, 8:811–819, 2011.

[37] D. Huang, E. A. Swanson, C. P. Lin, J. S. Schuman, W. G. Stinson, W. Chang, M.R. Hee, T. Flotte, K. Gregory, and C.A. Puliafito. Optical coherence tomography. *Science*, 254(5035):1178–1181, 1991.

[38] F. Helmchen and W. Denk. Deep tissue two-photon microscopy. *Nature Methods*, 2:932–940, 2005.

[39] I. M. Vellekoop and A. P. Mosk. Focusing coherent light through opaque strongly scattering media. *Opt. Lett.*, 32(16):2309–2311, 2007.

[40] I. M. Vellekoop, E. G. van Putten, A. Lagendijk, and A. P. Mosk. Demixing light paths inside disordered metamaterials. *Opt. Express*, 16(1):67–80, 2008.

[41] M. Davy, Z. Shi, and A. Z. Genack. Focusing through random media: Eigenchannel participation number and intensity correlation. *Phys. Rev. B*, 85:035105, 2012.

[42] X. Cheng and A. Z. Genack. Focusing and energy deposition inside random media. *Opt. Lett.*, 39(21):6324–6327, 2014.

[43] Z. Shi, M. Davy, J. Wang, and A. Z. Genack. Focusing through random media in space and time: a transmission matrix approach. *Opt. Lett.*, 38(15):2714–2716, 2013.

[44] P.A. Mello, E. Akkermans, and B. Shapiro. Macroscopic approach to correlations in the electronic transmission and reflection from disordered conductors. *Phys. Rev. Lett.*, 61:459–462, 1988.

[45] P. Sebbah, B. Hu, A. Z. Genack, R. Pnini, and B. Shapiro. Spatial-field correlation: The building block of mesoscopic fluctuations. *Phys. Rev. Lett.*, 88:123901, 2002.

[46] A. A. Chabanov, B. Hu, and A. Z. Genack. Dynamic correlation in wave propagation in random media. *Phys. Rev. Lett.*, 93:123901–123904, 2004.

[47] Y. Imry and R. Landauer. Conductance viewed as transmission. *Rev. Mod. Phys.*, 71:S306–S312, 1999.

[48] C.H Hsu, S.F. Liew, A. Goetschy, H. Cao, and A.D. Stone. Correlation-enhanced control of wave focusing in disordered media. *Nature Physics*, 13:497–501, 2017.

[49] C.W. Hsu, A. Goetschy, Y. Bromberg, A. D. Stone, and H. Cao. Broadband coherent enhancement of transmission and absorption in disordered media. *Phys. Rev. Lett.*, 115:223901, 2015.

[50] M. Davy, Z. Shi, J. Park, C. Tian, and A. Z. Genack. Universal structure of transmission eigenchannels inside opaque media. *Nat Commun*, 6:1–6, 2015.

[51] O. S. Ojambati, A. P. Mosk, I. M. Vellekoop, A. Lagendijk, and W. L. Vos. Mapping the energy density of shaped waves in scattering media onto a complete set of diffusion modes. *Opt. Express*, 24(16):18525–18540, 2016.

[52] O. S Ojambati, H. Yä lmaz, A. Lagendijk, A. P Mosk, and W. L. Vos. Coupling of energy into the fundamental diffusion mode of a complex nanophotonic medium. *New Journal of Physics*, 18(4):043032, 2016.

[53] Benoît Gérardin, Jérôme Laurent, Arnaud Derode, Claire Prada, and Alexandre Aubry. Full transmission and reflection of waves propagating through a maze of disorder. *Phys. Rev. Lett.*, 113:173901, 2014.

[54] Allard P. Mosk, Ad Lagendijk, Geoffroy Lerosey, and Mathias Fink. Controlling waves in space and time for imaging and focusing in complex media. *Nat Photon*, 6(5):283–292, 2012.

[55] A. Peña, A. Girschik, F. Libisch, S. Rotter, and A. A. Chabanov. The single-channel regime of transport through random media. *Nat Commun*, 5:1–8, 2014.

[56] R. Sarma, A. Yamilov, S.F. Liew, M. Guy, and H. Cao. Control of mesoscopic transport by modifying transmission channels in opaque media. *Phys. Rev. B*, 92:214206, 2015.

[57] A.A Lisyansky and D. Livdan. Influence of internal reflection on correlation of intensity fluctuation in random media. *Phys. Rev. B*, 47:14157–14164, 1993.

[58] P. Sebbah, R. Pnini, and A. Z. Genack. Field and intensity correlation in random media. *Phys. Rev. E*, 62:7348–7352, 2000.

[59] R. Sarma, A. Yamilov, P. Neupane, B. Shapiro, and H. Cao. Probing long-range intensity correlations inside disordered photonic nanostructures. *Phys. Rev. B*, 90:014203–014207, 2014.

[60] R. Sarma, A. Yamilov, P. Neupane, and H. Cao. Using geometry to manipulate long-range correlation of light inside disordered media. *Phys. Rev. B*, 92:180203, 2015.

[61] P. M. Morse and H. Feshbach. *Methods of theoretical physics*, volume 22. AAPT, 1954.

[62] L. V. Wang and H. Wu. *Biomedical optics: principles and imaging*. John Wiley & Sons, 2007.

[63] BL Altshuler, PA Lee, and RA Webb. *Mesoscopic phenomena in solids*. Elsevier, 1991.

[64] C. W. J. Beenakker. Random-matrix theory of quantum transport. *Rev. Mod. Phys.*, 69:731–808, 1997.

[65] S. Rotter and S. Gigan. Light fields in complex media: Mesoscopic scattering meets wave control. *Rev. Mod. Phys.*, 89:015005, Mar 2017.

[66] R. Schittny, M. Kadic, T. Bückmann, and M. Wegener. Invisibility cloaking in a diffusive light scattering medium. *Science*, 345(6195):427–429, 2014.

[67] W. Choi, A. P. Mosk, Q. Park, and W. Choi. Transmission eigenchannels in a disordered medium. *Phys. Rev. B*, 83:134207, 2011.

[68] M. Kim, Y. Choi, C. Yoon, W. Choi, J. Kim, Q. Park, and W. Choi. Maximal energy transport through disordered media with the implementation of transmission eigenchannels. *Nat Photon*, 6(9):581–585, 2012.

[69] S. M. Popoff, A. Goetschy, S. F. Liew, A. D. Stone, and H. Cao. Coherent control of total transmission of light through disordered media. *Phys. Rev. Lett.*, 112:133903, 2014.

VITA

Milan Koirala obtained his Bachelor of Science from Tribhuvan University in Nepal in 2007. He was a physics student with chemistry and mathematics as subsidiary subjects.

Milan obtained his Masters degree from Tribhuvan University in Nepal in 2012. During his time in Nepal Academy of Science and Technology (NAST), completing his masters in physics under the supervision of Dr. Buddha R. Shah and Mr. Prakash M. Shrestha, he worked to find natural background radiation in Kathmandu Valley and the Chure region of Nepal as his thesis project. His thesis project was presented as, "Assessment of natural background radiation around Kathmandu Valley and Chure region."

At Missouri University of Science and Technology, he earned his Doctor of Philosophy in physics on July 2019. He joined the group of Dr. Alexey Yamilov to work on his research project, which focused on coherence effects in wave propagation through complex media. While there, he greatly enjoyed his work as a research assistant to Dr. Alexey Yamilov. He served as a teaching assistant in the physics department. In addition to publishing the papers presented in this dissertation, Milan presented his research at scientific meetings and participated in conferences. Milan earned competition prize for presentations given at the Missouri S&T physics department. While in Rolla, he served as a graduate student representative from the physics department.